BLOCK IONOMER COMPLEX FORMULATIONS FOR IN VIVO PROTEIN DELIVERY

Yuhang Jiang

A dissertation submitted to the faculty at the University of North Carolina at Chapel Hill in partial fulfillment of the requirements for the degree of Doctor of Philosophy in the Eshelman School of Pharmacy (Molecular Pharmaceutics)

Chapel Hill
2016

Approved By:

Alexander Kabanov

Hong Yuan

Elena Batrakova

William Banks

Shawn Hingtgen

ABSTRACT

Yuhang Jiang: Block ionomer complex formulations for in vivo protein delivery
(Under the direction of Alexander Kabanov)

Complex coacervation between therapeutic proteins and hydrophilic ionic-neutral block-copolymers leads to the formation of core-shell structured nanoparticles gently packaging the proteins in its core (reviewed in CHAPTER 1). This kind of nanoparticle, termed block ionomer complex (BIC), has great potential as protein delivery vehicles because of its simple and non-denaturing manufacturing procedure. However, reports on in vivo application of protein BICs are not common, primarily because of their instability at physiological ionic strength. The focus of this thesis is to explore the usage of BIC as an in vivo protein delivery vehicle.

Our lab previously developed a protein BIC formulation, "SOD1 nanozyme", formed between the protein superoxide dismutase 1 (SOD1) and the block copolymer poly(ethylene glycol)-poly(L-lysine) (PEG-PLL) followed by crosslinking with 3,3'-dithiobis(sulfosuccinimidyl propionate) (DTSSP). CHAPTER 2 examines the mechanism for SOD1 nanozyme to be effective for stroke treatment. Active incorporation of SOD1 nanozymes into the growing thrombus turns out to retain them at the vicinity of the injured sites on blood vessels after stroke.

Although helpful in the retention of SOD1 nanozymes after stroke, polylysine can be toxic in vivo because of their cationic charge which easily disrupts cellular membranes. CHAPTER 3 describes a project that aims to replace the polylysine component with poly

(aspartate diethyltriamine) (PAsp(DET)). This polymer is less toxic than polylysine due to its unique two-step protonation behavior, and its BIC with SOD1 has a similar size as the PLL-based SOD1 nanozyme. The therapeutic efficacy of this new formulation is also close to that of the PLL-based formulation.

This dissertation also involves the characterization of a protein BIC formulation without crosslinking. We found that the BIC formed by brain derived neurotrophic factor (BDNF) and PEG-poly (L-glutamic acid) is stable at physiological salt concentrations. While protecting the cargo BDNF from interaction with a variety of mucosal proteins, the complex specifically releases active BDNF in the presence of its receptor, tropomyosin receptor kinase B (TrkB). Compare with native BDNF, The complex delivered significantly higher amounts of protein to different brain regions after intranasal delivery. This work is presented in CHAPTER 4.

In summary, BIC is a promising platform for in vivo delivery of therapeutic proteins with careful design of stabilization strategies.

I dedicate this work to my beloved grandmother, Jinghua Zhang (张景华).

ACKNOWLEDGMENTS

I would like to express my sincere gratitude to my advisor Prof. Alexander Kabanov for his continuous support of my Ph.D. study and related research, for his patience, motivation, and immense support in all research fields I tried to explore. His guidance helped me all the time during my grad school. I could not have imagined having a better advisor for my Ph.D. study.

Besides my advisor, I also would like to thank other professors in my thesis committee: Prof. Shawn Hingtgen, Prof. Hong Yuan, Prof. William Banks, and Prof. Elena Batrakova for support, advice, and encouragement. Their insightful questions asked in my committee meetings are always very inspiring to me. Indeed, many of the important experiments I described in my thesis can find their roots in these committee meeting questions.

I would also like to thank Prof. Devika S-Manickam and Dr. Xiang Yi for their continuous support and mentorship for me during my graduate study. Devika mentored me since the first day I joined the lab when she was doing her post-doctoral training in our laboratory. She taught me almost everything I needed to know to conduct experiments independently, and even now I am still trying to become an organized professional scholar just like her. Xiang mentored me on many important techniques involved in the pharmacokinetic analysis of proteins including iodine labelling, animal surgery and serum collection. These techniques are so frequently used that I couldn't have completed any single chapter of this thesis without having learned them from Xiang. My sincere thanks also goes to Prof. Louise McCullough, and Prof. Rajkumar Verma who provided me an opportunity to join their team as a visiting student in the summer of 2013, gave me access to their laboratory and research

facilities, and trained me how to do stroke surgery in mice. Without their precious support it would not have been possible for me to complete my two projects on formulation of SOD1 nanozyme. Indeed, my completion of graduate study would not have been possible without the help I received from my collaborators. In addition to Dr. McCullough and Dr. Verma, I also want to thank many of my collaborators in other institutions, especially Dr. William Banks and Kristin Bullock from University of Washington; Dr. Younsoo Bae and Steven Rheiner from University of Kentucky, as well as Dr. Carol Milligan and Phonepasong Arounleut from Wake Forest University.

I wouldn't have successfully completed my graduate research projects without collaboration and support from my fellow labmates. In specific, I want to thank Dr. Anya Brynskikh and Jimmy Fay, former and current graduate students in Kabanov lab. Anya was a senior graduate student in the lab when I joined, and my first project was actually a continuation of hers. She is very knowledgeable in neuroscience, and I learnt from her many useful techniques to conduct experiments in this field including stroke surgery in rats, immunohistochemistry, and confocal microscopy. Jimmy is a very talented graduate student in the Department of Biochemistry and Biophysics, and he rotated in our lab in 2015 before he decided to join us and work on the same project with me. Trained as a biophysicist, Jimmy offered me a lot of help by introducing a completely new set of research tools into my projects, not to mention the many in-depth discussions on complex characterization and molecular modelling experiments with him.

In addition to Anya and Jimmy, I want to thank many other lab members for their friendship and company during these years. Ms. Yuling Zhao, Dr. Zhijian He, Miss Xiaomeng Wan, Mr. Youngee Seo, Miss Poornima Suresh, Ms. Katie Mutilin, Dr. Jing Tong, Dr. Yi Zhao, Miss Dongfen Yuan, Mr. Duhyeong Hwang, Mr. Matt Haney, Dr. Dasha Filonova, Dr. Vivek Mahajan, Dr. Hemant Vishwasrao, Dr.Soo Kim, Dr. Jing Gao, Dr. Liz Wayne, Ms. Jubina

Bregu, Mr. Nazar Filonov, and Ms. Shu Li, along with all past and present members of Kabanov Lab. I also want to thank my friends from other labs and institutions for their kind help throughout my graduate study: Dr. Hui Wang, Dr. Jing Fu, Dr. Yuan Zhang, Dr. Yuanzeng Min, Dr. Kai Wang, Mr. Jay Kim, Dr. Lei Miao, Ms. Qiaoxi Li, Ms. Yingqiu Zhou, Dr. Tojan Rahhal, Dr. Dylan Glatt, Dr. Hao Cai, Dr. Lei Peng, Mr. Jay Kim, Ms. Junghyun Lee, Ms. Xiaokun Qian, Ms. Naihan Chen, Dr. Kevin Han, Ms. Erin Wilson, Mr. Bing Yang, and Ms. Angela Yang.

My thesis work involves interdisciplinary efforts which is not possible to be conducted by a single lab. I want to express my sincere thanks to all the professors and core facility managers who have kindly allowed me to use their instruments and trained me to use them with confidence. Dr. Ashutosh Tripathy for training me on ITC, SPR, and SEC-MALS experiments; Dr. Wallace Ambrose and Dr. Amar S. Kumbhar for helping me with TEM and AFM to characterize my nanoparticles; Dr. Michael Jay, Dr. Matthew Sadgrove, and Dr. Zibo Li for kindly letting me use their gamma counters for my pharmacokinetic analysis; Dr. Bob Bagnell for his help with my confocal microscopy experiments; Dr. Hong Yuan, Mr. Jonathan Frank, and Mr. Joseph Merrill for their help with my IVIS imaging, PET imaging and autoradiography attempts in my projects.

Last but not least, I want to thank my father Dayan Jiang, my mother Yun Wu, and all other members of my family for their understanding and support during my journey in the United States. I have not went back to China for the past five years during my grad school, yet I still feel their trust and love guiding me through the mist of my toughest times. I love them forever.

PREFACE

In this thesis I report my work during my graduate study in Sasha's lab. The focus of my research is to explore possibilities of protein formulation using BICs. CHAPTER 1 aims to provide an overview of the mechanism for proteins to bind to polyelectrolytes in the aqueous solution, and the application of this technology in the past 20-30 years. It is part of a more comprehensive review currently under preparation which will involve general discussions on the physiochemical properties of block ionomer complexes in a bigger framework.

My research was done in collaboration with many talented scientists. In CHAPTER 2, Dr. Anya Brynskikh established experimental protocols for stroke surgery in rats and immunohistochemistry used in this project. She also contributed to generate Figure 2.2, Figure 2.5, and Figure 2.6, and made significant contributions during the preparation of the manuscript for publication; Dr. Devika Manickam established the protocol for the synthesis and purification of SOD1 nanozymes, directly supervised this project, and contributed to writing. The paper was published previous to writing this thesis with the following citation:

Jiang Y, Brynskikh AM, S-Manickam D, Kabanov AV. J Control Release. 2015 Sep 10; 213:36-44. Doi: 10.1016/j.jconrel.2015.06.021.

In CHAPTER 3, Phonepasong Arounleut bred all the amyotrophic lateral sclerosis mice, performed all the experiments involving this animal model, and contributed to all the data presented in Figure 3.7; Dr. Carol Milligan provided experimental resources and supervision for Phonepasong's work, and contributed to manuscript writing; Steven Rheiner synthesized the PEG-PAsp(DET) polymer; Dr. Younsoo Bae supervised Steven's work and

contributed to the writing of manuscript; Dr. Devika S-Manickam originated the idea and supervised the whole project. The paper was published previous to writing this thesis with the following citation:

Jiang Y, Arounleut P, Rheiner S, Bae Y, Kabanov AV, Milligan C, Manickam DS. J Control Release. 2016 Jun 10; 231:38-49. Doi: 10.1016/j.jconrel.2016.02.038.

In CHAPTER 4, Jimmy Fay helped in several horizontal agarose gel electrophoresis experiments in this project, actively explored possible characterization experiments including Surface Plasmon Resonance, and Nanoparticle Tracking Analysis, generated Figure 4.8, and contributed to manuscript writing; Dr. Chi-Duen Poon designed and performed all the molecular dynamic modelling experiments; Yuling Zhao helped in animal handling in the PK experiments as presented in Figure 4.14, Figure 4.15, Figure 4.16, and Figure 4.18; Kristin Bullock performed the brain efflux experiments described in Figure 4.17; Dr. Devika S-Manickam contributed to early proof-of-concept experiments of Nano-BDNF formulation; Dr. Xiang Yi participated in most animal experiments, performed data analysis of all PK experiments, and actively supervised other experiments in this project for a year; Dr. William Banks provided invaluable support for iodine labelling, animal surgery, data analysis and interpretation of PK experiments.

In all the aforementioned Chapters, Dr. Alexander Kabanov provided the necessary resources for the researches to be complete, supervised and coordinated these research projects, and constantly contributed very insightful scientific advises and very challenging scientific questions which made sure the high scientific qualities of the outcomes from these projects.

My research was supported by the following funding agencies:

National Institutes of Health grant number **RO1NS051334**;

Institutional Development Award (IDeA) from the National Institute of General Medical Sciences of the National Institutes of Health under grant number **P20GM103480**;

North Carolina Institute of Translational and Clinical Sciences grant number **550KR51322**;

National Center for Advancing Translational Sciences award number **ULTR000083**;

National Institutes of Health grant number **R21NS08815202**;

HeART Award from the International Rett Syndrome Foundation for funding;

The *Carolina Partnership*, a strategic partnership between the UNC Eshelman School of Pharmacy and The University Cancer Research Fund through the Lineberger Comprehensive Cancer Center.

TABLE OF CONTENTS

LIST OF TABLES

LIST OF FIGURES

LIST OF ABBREVIATIONS AND SYMBOLS

A	light absorption
AFM	atomic force microscopy
AKT	serine/threonine-protein kinase-1
ALS	amyotrophic lateral sclerosis
ANOVA	analysis of variance
Asp	aspartic acid
AUC	area under the curve
B/S ratio	brain/serum ratio
BBB	blood brain barrier
BDNF	brain derived neurotrophic factor
BIC	block ionomer complexes
BSA	bovine serum albumin
C3M	complex core coacervate micelle
CB	cerebellum
cl-	cross-linked
CNS	central nervous system
CPM	counts per minute
D or Da	Dalton
DAB	3, 3-diaminobenzidine
DAPI	4', 6-diamidino-2-phenylindole
D_{eff}	effective diameter
DET	diethylenediamine
DLS	dynamic light scattering

DMEM	Dulbecco's modified eagle medium
dn/dc	refractive index increment
DNA	deoxyribonucleic acid
DSPE	1, 2-Distearoyl-sn-glycero-3-phosphoethanolamine
DTSSP	3, 3'-Dithiobis (sulfosuccinimidylpropionate)
DTT	dithiothreitol
e_c	elementary charge
EDC	1-ethyl-3-(3-dimethylaminopropyl) carbodiimide
EDTA	ethylenediaminetetraacetate
ERK	extracellular Signal-regulated Kinase
F	fluorescence
FC	frontal cortex
FPLC	fast protein liquid chromatography
G	Gibbs free energy
GSH	glutathione
H	enthalpy
H&E	hematoxylin and eosin
HAGE	horizontal agarose gel electrophoresis
HSA	human serum albumin
HB	HEPES buffer
HBS	HEPES buffered saline
HC	hippocampus
hCMEC/D3	human brain microvascular endothelial cell
HEPES	4-(2- hydroxyethyl)-1-piperazineethanesulfonic acid)
HT	hypothalamus

Huh-7	a hepatocyte derived cellular carcinoma cell line
I	ionic strength
I/R	ischemia/reperfusion
IACUC	institutional animal care and use committee
IC	intracarotid
ICA	internal carotid artery
ICP-MS	inductively coupled plasma mass spectrometry
ICV	intracerebral ventricular
ID	injected dose
IgG	immunoglobulin G
IHC	immunohistochemistry
INB	intranasal to brain
IP	intraperitoneal
IPEC	interpolyelectrolyte complex
ITC	isothermal titration calorimetry
IV	intravenous
K_b	Boltzmann constant
K_i	unidirectional influx rate
K_{obs}	apparent binding affinity
LCST	lower critical solution temperature
L_p	persistence length
LR	lactated Ringer's solution
MALS	multi-angle light scattering
MB	midbrain
MCA	middle cerebral artery

MCAO	middle cerebral artery occlusion
MD	molecular dynamics
MPS	mononuclear phagocyte system
M_w	molecular weight, or molar mass
N_A	Avogadro's number
$NaBH_4$	sodium borohydride
NaCl	sodium chloride
$NaCNBH_3$	sodium cyanoborohydride
NaN_3	sodium azide
NF-L	neurofilament
NGS	normal goat serum
NHS	N-hydroxysuccinimide
NIH	National Institute of Health
NMJ	neuromuscular junction
NP	nanoparticle
NSC-34	immortalized mouse motor neuron cell
NVU	neurovascular unit
OB	olfactory bulb
OC	occipital cortex
OCT	optimal cutting temperature compound
P	postnatal day
PAGE	polyacrylamide gel electrophoresis
PAsp(DET)	poly[N-[N'-(2-aminoethyl) - 2-aminoethyl] aspartamide]
PB	phosphate buffer
PBS	phosphate buffered saline

PC	parietal cortex
PD	Parkinson's disease
PDB	protein data bank
PDI	polydispersity index
PECAM-1	platelet endothelial cell adhesion molecule
PEG	poly(ethylene glycol)
PEI	poly(ethylenimine)
PG	pyrogallol
pI	isoelectric point
PIC	polyion complex
PiPrOx	poly(isopropyl oxazoline)
PLE	poly(L-glutamic acid)
PLGA	poly(lactic-co-glycolic acid)
PLL	poly(L-lysine)
PNIPAAM	poly(isopropylacrylamide)
PON	pons
PTS	protein thermal shift
PVS	perivascular space
RB	rest of the brain
RES	reticuloendothelial system
R_g	radius of gyration
R_h	hydrodynamic radius
rHsp70	recombinant heat shock protein 70
ROS	reactive oxygen species
RT	room temperature

rt-PA	recombinant tissue plasminogen activator
S	entropy
SD	standard deviation
SDS	sodium dodecyl sulfate
SEC	size exclusion chromatography
SEM	standard error of mean
sIgA	secretory immunoglobulin A
S-NHS	N-hydroxysulfosuccinimide
SOD	superoxide dismutase
SOD1	copper/zinc SOD
SPDP	succinimidyl 3-(2-pyridyldithio) propionate
ST	striatum
T	temperature
$t_{1/2}$	half-life
TA	tibialis anterior
TBS	Tris-buffered saline
TBST	Tris-buffered saline with 0.1% Tween 20
TCA	trichloroacetic acid
TEM	transmission electron microscopy
TF	tissue factor
TH	thalamus
T_m	melting temperature
TrkB	tropomyosin receptor kinase B
TrkB-Fc	Recombinant human TrkB Fc chimera protein
TTC	2, 3, 5-triphenyltetrazolium chloride

UNC	the University of North Carolina at Chapel Hill
UNMC	University of Nebraska Medical Center
VAChT	vesicular acetylcholine transporter
WB	whole brain
$Z_{-/+}$ or $Z_{+/-}$	charge ratio
α	degree of protonation
α-BTX	alpha-bungarotoxin
κ^{-1}	Debye length
ρ	structural density
Δ	a symbol indicating change

CHAPTER 1 INTRODUCTION[1]

During the past decade, therapeutic proteins (e.g. antibodies, hormones, enzymes, and vaccines) have rapidly emerged as mainstream drug candidates in the pharmaceutical industry. Many new protein drugs are under investigation, raising hope for curing a large number of diseases previously considered "incurable" such as cancer, stroke, diabetes, etc. Nonetheless, not all proteins are naturally good drug candidates. Indeed, many of the most potent therapeutic proteins cannot make it to the clinic due to *in vivo* enzymatic degradation, rapid clearance from the circulation, immunogenicity, and inability to cross cellular membranes. To address these problems, a carrier is necessary to protect the proteins, facilitate their transport through biological barriers, and deliver them to their target site(s) of action. Microparticles composed of poly(lactic-co-glycolic acid) (PLGA) are the most well established carrier for protein delivery. With the controlled degradation of the polymeric matrix, the proteins encapsulated in the PLGA particles can be slowly released over a period of time [1]. Considering PLGA particles can be engineered to remain in the circulation for a long time [2], this approach can generate a sustained release profile for the cargo proteins after a single injection. The disadvantage of this approach is the extensive use of organic solvents in the manufacturing process which usually leads to denaturation or inactivation of the proteins [3]. Moreover, a large faction of proteins are usually associated with the surface of the microparticles and are not completely encapsulated. Once injected, these proteins will quickly dissolve in the blood stream and result in a sudden peak serum exposure, a phenomenon also known as "burst

[1] Part of This chapter previously appeared as a manuscript soon to be submitted.

release" which can associate with serious adverse events for some protein therapeutics [4]. Therefore, new strategies are needed for protein delivery to overcome these limitations.

1.1 Block Ionomer Complex

Nearly 90 years ago, Bungenberg de Jong and Kruyt first reported the phenomenon of "complex coacervation"[5] where the mixing of two oppositely charged colloids in aqueous solution lead to phase separation [6]. This phenomenon was later suggested as a pre-cellular structure and therefore the "origin of life" by Oparin [7]. Complex coacervation between oppositely charged polyelectrolytes has extensive applications in the food and pharmaceutical industries for separation processes. However, it was not until the mid-1990s when researchers started to realize that the coacervation process can be thermodynamically confined within well dispersed compartments, simply by extending one or both the polyelectrolytes by an uncharged hydrophilic polymer block [6, 8, 9]. The introduction of this hydrophilic block transforms the phase separation process into micellization, making it a powerful tool for therapeutic delivery of small molecules [10], genetic materials [11], as well as proteins [12, 13]. Indeed, the microenvironment and phase behavior of the coacervates strikingly resemble the membrane-less protein bodies in the cytoplasm formed by RNA and proteins [14, 15]. Hence, they represent a natural protein packaging mechanism, and offer a very gentle immobilizing environment for proteins to stay in the coacervate core protected by the hydrophilic corona. The production of block ionomer complexes (BICs) eludes any exposure to organic solvents, a significant advantage over the commonly used PLGA-based microspheres/nanoparticles. This chapter aims to review the physical roots of BIC formation, unique properties of protein BICs, common methods to stabilize protein BICs, and their biomedical applications. There are currently four terms in use interchangeably to describe this system: interpolyelectrolyte complex (IPEC) [16], complex core coacervate micelle (C3M) [6], polyion complex (PIC) [9],

and BIC [8]. For the sake of clarity, the term “block ionomer complex” will be employed throughout this thesis.

1.1.1 Formation of BIC

Electrostatic interaction is widely accepted to be the driving force for BIC formation [8, 9]. It generally comprises two components: the coulombic attraction between opposite charges, and the release of small counter ions originally condensed by the polyelectrolytes. Other non-covalent forces, like hydrophobic interactions and hydrogen bonding, have also been reported to contribute to the formation of BICs depending on the chemical nature of polyelectrolytes as well as solution environments (e.g. pH, ionic strength, etc.) [17]. A recent report suggest that even strong cation-π interactions can drive the formation of BICs from two like-charged polyelectrolytes by overcoming longer-range electrostatic repulsion [18]. The contribution of these non-electrostatic interactions can be more prominent if BICs are formed in environments where the electrostatic interactions are inhibited (e.g. solutions of high ionic strength).

Thermodynamically, the spontaneous formation of BIC entails a negative change in total Gibbs free energy (ΔG) of the system, which is further determined by the balance between changes in system entropy ($-T\Delta S$) and enthalpy (ΔH). A considerable body of literature has been published over the past two decades [9, 19, 20] discussing how individual events contribute to entropic and enthalpic changes depending on the nature (strong vs. weak) and charge density of the polyelectrolytes, as well as pH, temperature, and ionic strength of the solution. In most systems, this process is primarily driven by favorable entropic gains related to the release of pre-condensed small counter-ions and water molecules upon complexation [19, 21-25], as evidenced by the endothermal signals observed in isothermal titration calorimetry experiments [19, 25]. This effect is counterbalanced by unfavorable entropic changes originating from immobilization of polyelectrolytes upon complexation and formation

of highly ordered water networks at the colloidal interface [26]. The formation and rupture of hydrogen bonds is the major contributor for the enthalpic change in the system, which is usually determined by the dehydration/rehydration at the complex interface as well as direct formation of hydrogen bonds between the polyelectrolytes [26].

1.1.2 Protein BICs

As natural polyelectrolytes, many proteins can spontaneously participate in the formation of BICs with oppositely charged block ionomers in the aqueous solution. This process is usually described as "self-assembly", and is arguably the simplest way to load proteins into a nanoparticle. The same driving forces and thermodynamic considerations discussed in the previous section also apply here. Nevertheless, interactions between proteins and linear polyelectrolytes are featured by some unique properties due to the structural rigidity and charge anisotropy of the proteins.

1.1.2.1 Structural rigidity

Most globular proteins have well-defined high order structures with limited conformational flexibility. As a result, their partner polyelectrolytes have to be flexible enough for the binding to be stable [27-29]. Hatorri *et al*. observed a reciprocal relationship between binding affinity (K_{obs}) and polymer persistence length (L_p) in the complexation between β-lactoglobulin and three different polyanionic polymers [30]. Furthermore, even with a highly flexible polymer, the precise compensation to the local charge distribution of a protein can result in a great loss in its configurational entropy which is unfavorable for BIC formation. Indeed, many protein BICs are formed at non-stoichiometric charge ratios, and there is usually no noticeable change in its major physical properties at charge stoichiometry [13, 31, 32]. This implies the existence of unsaturated charges on either or both species that cannot be accounted for by complementarity of each other. These unsaturated charges are presumably compensated

by small ions in the solution, which in fact renders the microenvironment of the BIC core highly hydrated [17] and more amenable for protein storage.

1.1.2.2 Charge anisotropy

Another unique feature setting proteins apart from other polyelectrolytes is their heterogeneous distribution of positive and negative charges on the surface. When the charges exist as localized clusters, they become the so-called "charge patches" [33]. This concept is initially introduced in the field of ion-exchange chromatography where proteins can bind to the stationary phases even when the mobile phase pH is on the "wrong side" of the protein isoelectric point (pI) [34]. Indeed, when the dimension of protein globules are comparable or longer than the Debye length (κ^{-1}) in the solution, their charge patches will be isolated from each other, and interact with polyelectrolytes individually [35]. In this scenario, the complexation between polyelectrolyte to a protein under conditions where both species have the same sign of net charge [30, 36, 37] can occur as a consequence of "patch"-mediated short-range electrostatic attractions overcoming long-range repulsion from other "patches"[38]. In light of the highly differential charge distribution pattern of proteins, this effect makes it possible for a polyelectrolyte to specifically recognize and isolate a particular protein from a mixture of same-charged proteins [39].

1.2 Environmental effects on protein BICs

1.2.1 Ionic strength (I)

As introduced in the previous section, electrostatic interaction is the predominant force driving the formation of BICs. The increase of ionic strength suppresses it by decreasing the Debye length in water, as demonstrated by the following equation [40].

$$\kappa^{-1} = \frac{0.304}{\sqrt{I}}$$

It is then tempting to extrapolate a monotonic dependence of BIC stability on ionic strength of the solution. Interestingly, both experimental observations [38, 41, 42] and

computer simulation results [43] suggest that the binding constant between protein and polyelectrolyte do not simply decrease with the increase of *I*, but instead usually displays a maximum in the range of 5mM < *I* < 30mM [38].

This phenomenon cannot be simply explained by hydrophobic interaction or hydrogen bonding because their effects on polyelectrolyte binding are usually overshadowed by electrostatic interaction at such low ionic strength. Actually, while high ionic strength leads to screening of electrostatic interaction between the protein and the polyelectrolyte, a low level of ionic strength is necessary to isolate the "charge patches" on the protein. As *I* value continues to decrease below 5mM, the Debye length will significantly increase. When it reaches a level comparable to the dimension of the protein globule, the repulsive effects between the polyelectrolyte and same-charged "patches" on the protein starts to take effect and destabilize the complex [38]. Similar consideration applies to the polyelectrolytes - a certain level of ionic strength is necessary to screen the repulsion between charges of adjacent repeating units on the polymer. When the ionic strength is low, these repeating unites will try to maximize their distances between each other, which subsequently increases the stiffness of the polymer [44]. As discussed in the previous section, this effect is unfavorable for its binding to proteins. Hence, the formation and stability of BIC requires a moderate level of ionic strength in the solution.

1.2.2 pH

Most proteins are weak polyelectrolytes with pI values ranging from 4 – 10 [45]. Therefore, solution pH closely modulates the density and distribution of protein surface charges, as well as the protonation status of the polyelectrolytes. Subsequently, gradual changes in solution pH have been shown to induce sequential changes in physical states of the coacervation core and ultimate disassembly of the complex in a number of protein-polyelectrolyte systems [46-49]. This feature makes protein BICs potentially advantageous as

delivery tools since variations in local pH is common in biological systems, especially under pathological conditions. For instance, endosomal pH drops from 6.8 – 4.9 during its maturation process [50]; tumor microenvironment usually features slightly acid pH ranging from 6.9 – 6.5 [51] and ischemic stroke also induces a quick drop of brain tissue pH from 7.0 to 6.2 [52].

1.2.3 Temperature

The effect of temperature on protein BICs is highly system-dependent and usually reflects the contribution of non-electrostatic interactions. In general, higher temperature upholds hydrophobic interaction, while lower temperature favors hydrogen bonding [53]. Nevertheless, temperature fluctuation in the physiologically relevant range (36^{o}C – 43^{o}C) usually do not make a big difference for most protein BICs. Exceptions are those formulated with a class of temperature-responsive polymers as the hydrophilic block, including poly-(isopropylacrylamide) (PNIPAAM) [54] and poly-(isopropyl oxazoline) (PiPrOx)[55]. This class of polymers have lower critical solution temperatures (LCST) that are above room temperature, and become insoluble at elevated temperatures. As a result, protein BICs formed using these polymers whose hydrophilic block can undergo temperature-induced phase transition can selectively release the cargo proteins at certain temperatures [56]. By chemically modifying these polymers, their LCST can be tuned close to body temperature (35^{o}C – 40^{o}C) [57, 58]. This is particularly useful for targeting inflamed or tumorous tissues where the tissue temperature is higher than normal. Another exciting application of this class of BICs is in combination with far infrared irradiation to create local hyperthermia and induce drug release at virtually any tissue of interest [59].

1.3 Stabilization of protein BICs

Although many protein BICs can maintain their physical characteristics for months in a low-salt buffer (5mM-30mM), colloidal stability is the primary challenge associated with BIC for its biomedical application *in vivo*. Physiological fluids typically have an ionic strength

of about 150mM to maintain homeostasis, which readily disassembles most protein BICs before they can reach their target sites of action. In many cases, additional engineering is necessary to stabilize protein BICs and effectively use them for *in vivo* protein delivery. These engineering approaches include chemical crosslinking, charge conversion, ternary complex formation, and introduction of hydrophobic interactions.

1.3.1 Chemical crosslinking

Chemical crosslinking is the most common way to stabilize BICs for in vivo protein delivery. With the introduction of small crosslinkers into the system, the electrostatic coupling between protein and polymer can be reinforced by covalent conjugation, thereby preventing the BIC from dissociation in the body fluids. Depending on the need for proteins to be released at the target site, the crosslinker can be designed to be environmentally sensitive.

Glutaraldehyde is one of the earliest crosslinkers for proteins. Despite the simplicity of its structure, it demonstrates very complicated chemical behaviors in solution depending on the pH, temperature and concentration [60]. Consequently, its crosslinking chemistry usually involves a combination of several different mechanisms such as Schiff base formation and Michael-type addition. Despite this complexity, glutaraldehyde crosslinks BICs primarily by reacting with amine groups on lysine and arginine residues on the protein or the polymer. The reaction can also be followed by the addition of reducing agents such as sodium borohydride ($NaBH_4$) or sodium cyanoborohydride ($NaCNBH_3$) in order to stabilize the double bonds in the Schiff base [61-64]. These BICs demonstrated superb stability and therapeutic efficacy in vivo. However, glutaraldehyde has long been criticized for being too heterogeneous and toxic for medical applications[65].

Alternative to glutaraldehyde for protein BIC stabilization are amine-reactive bi-functional crosslinkers, including N-hydroxysuccinimide (NHS) esters and imidoesters. Both of them contain highly reactive leaving groups that can be substituted upon nucleophilic attacks

from the primary amine groups on either the protein or the polymer, with slight differences in optimum pH of the reaction. Sometimes disulfide bonds are introduced in these crosslinkers (3, 3'-Dithiobis (sulfosuccinimidylpropionate), DTSSP or Dimethyl dithiobispropionimidate, DTBP) to facilitate red-ox mediated cargo release [13, 32, 63, 66].

In light of the proximity between negatively charged carboxylate groups and positively charged amine groups in many protein BIC systems, 1-ethyl-3-(3-dimethylaminopropyl)carbodiimide (EDC) can be used as a zero-length crosslinker. This reagent activates carboxyl groups for spontaneous reaction with primary amines and result in the formation of a peptide bond. Its crosslinking efficiency can be further increased if used in combination with NHS or sulfo-NHS [67].

Crosslinking can also be mediated by chemical modifications on the polymer. In this scenario, the crosslinking chemistry is usually designed to be sensitive to environmental changes. As an example, Hefferman et al. reported a strategy where the amine groups of poly(ethylene glycol)-poly(L-lysine) (PEG-PLL) are modified with crosslinkable dithiopyridine groups with Michael addition which preserves the positive charges on the PLL chain [68]. This modified polymer successfully encapsulated succinimidyl 3-(2-pyridyldithio) propionate (SPDP)-modified ovalbumin/catalase through disulfide bond formation.

One potential downside of crosslinking is the immobilization of proteins in the core of the BIC with limited to no freedom of movement. This could be a disadvantage for the delivery of growth factors or antibodies which requires complementary binding with receptors or antigens to exert their functions. Nevertheless, crosslinking are most suitable for the delivery of enzymes with small substrates that can freely diffuse into the core of BIC without the need of having the enzymes released [12, 13, 32, 61, 63, 69-71]. The crosslinking of autolytic enzymes like trypsin in the BIC also prevents them from digesting each other, which is beneficial for their storage [62]. Protein activity loss is one of major concerns with crosslinking.

It can usually be ameliorated by careful selection of chemistry and optimization of input ratio of crosslinkers to reactive chemical groups on the protein. Indeed, a number of reports suggested insignificant loss of protein activity after crosslinking compared with their non-crosslinked counterparts [61, 62, 71].

1.3.2 Charge conversion

The primary reason for the instability of protein BICs at the physiological ionic strength is its insufficient charge density compared to synthetic polymers or DNA molecules. Therefore, charge conversion or "supercharging"[72] of proteins has been explored to increase BIC stability. The idea is to increase the charge density on the protein by converting positively charged amine groups into negatively charged carboxylate groups or vice versa. This approach was first reported by Lee et al. using citraconic amide and *cis*-aconic amide to modify the lysine groups on equine heart cytochrome c (Mw = ~12kD) [73]. The modification effectively converted the pI value of the protein by about 6, and as a result, effectively formed stable BICs with PEG–poly[N-[N'-(2-aminoethyl)- 2-aminoethyl] aspartamide] (PEG-pAsp(DET)) in a solution of 150mM NaCl. These BICs were effectively internalized by HuH-7 cells in vitro, where the citraconic amide and cis-aconic amide were hydrolyzed in the acidic endosomal environment. The cytochrome c then reversed its charge again and dissociated with PEG-PAsp(DET), which further disrupted endosomal membrane and facilitated the endosomal escape of cytochrome c. Soon after this work, a much bigger protein, an antibody (Mw = ~150kD) against the nuclear pore complex, was delivered to the cytoplasma of living HuH-7 cells in the same manner, and successfully inhibited their growth [74]. Recently, this system was further optimized by Kim et al in terms of the number of charge conversion sites and the ratio of homopolymer/block copolymer in the BIC, in order to develop it into a platform technology for intracellular antibody delivery [75].

1.3.3 Ternary BICs

In addition to directly participating in the complex coacervation process, proteins have also been reported to partition into the coacervate core of complexes composed of a charged-neutral block copolymer and an oppositely charged homopolyelectrolyte. The resulting complex are more stable against disintegration upon increases in ionic strength [76-80]. To prepare these complexes, the proteins are usually pre-mixed with a like-charged homopolyelectrolyte and then transferred to a solution containing an oppositely charged block copolymer. This process leads to the formation of a ternary BIC system containing the protein, the homopoyelectrolyte, as well as the block copolymer. It is also named "tripartite polyion micelles" in some works [81, 82]. The amount of proteins loaded into the complex can be modulated by complex composition, NaCl concentration and the starting concentrations of the protein [80]. Furthermore, the protein can be gradually released from the complex upon increasing ionic strength in the solution without destruction of the BIC structure [77, 78]. It is observed that the most stable complex formation occurs at an excess of homopolyelectrolyte over the protein [76]. As a result, the major limitation of ternary BIC is loading capacity. For example, in a lysozyme/ poly(acrylic acid)-poly(acryl amide) /poly(N,N-dimethylaminoethyl methacrylate) ternary system, the optimal number of lysozyme molecules was estimated to be 5–15 per complex [76]; in a lipase/ PEG-poly(2-methyl vinyl pyridinium)/ poly(acrylic acid) system, this number is 0.4-4.6, depending on the ionic strength of the solution [77].

1.3.4 Introducing hydrophobic interactions

Although electrostatic interaction is the primary driving force of BIC formation, one cannot ignore the contribution from forces of other nature, such as hydrogen bonding and hydrophobic interactions in maintaining its structural stability. Indeed, one strategy to stabilize BIC is the introduction of hydrophobic interactions at the coacervate core. Yuan et al. observed increased stability in solutions containing up to 0.1M NaCl of a BIC complex made from

lysozyme and PEG – poly (aspartic acid) (PEG-PAsp) by adding a single hydrophobic group to the ω-end of the PAsp block. Pispas further introduced hydrophobic monomers into the backbone of a block copolymer, which forms stable complexes with lysozyme in a solution containing 0.15 M NaCl [83].

1.4 Application of protein BICs

1.4.1 Intracellular delivery

Unlike small molecule drugs, most proteins cannot diffuse through the cellular membrane. Therefore, a delivery system that can transfer protein pharmaceuticals into the cytoplasm is the key for successful protein therapies with intracellular targets. To this end, BIC offers a great opportunity given its proven success in intracellular delivery of DNA and RNA molecules [84, 85].

The major technical challenge for proteins to be delivered in this way involves striking the right balance between the stability of BIC and the ability to release active proteins in the cytoplasm. To this end, chemical crosslinking is generally not a good stabilization strategy unless the crosslinker can be designed to be environmentally responsive and degrade to release the encapsulated proteins. As an example, crosslinkers can be designed to degrade and release cargo proteins inside the cells, taking advantage of the biochemical gradients between the cytoplasm and the extracellular space [32]. For example, the reduced form of glutathione (GSH) predominantly exists in the cytoplasm, creating a reductive environment in sharp contrast to the oxidizing environment of the extracellular space [86]. Hence, BICs crosslinked with disulfide bonds can release vaccine antigens inside the endosomes of antigen presenting cells [68]. Besides, protein BICs stabilized by charge conversion [74, 87] and ternary complex formation have also been reported to be successfully utilized for intracellular protein delivery [81, 82].

Another challenge involves endosomal escape of the proteins. As BICs are internalized into a cell, they immediately become entrapped in endosomes and will be later degraded by lysosomal enzymes [88]. To avoid degradation and ensure cytosolic delivery of the proteins, their endosomal escape needs to be facilitated. Kataoka et al. reported the use of PEG-block-poly [N-[N′-(2-aminoethyl)-2-aminoethyl] aspartamide] (PEG−PAsp(DET)) copolymer, which destabilizes endosomal membranes in the low pH environment [89], and successfully delivered charge-converted antibodies to the cytosol [74, 75].

1.4.2 Enzyme delivery

BIC is particularly useful for the delivery of enzymes, which is attributed to its "caging" and "hyperactivation" effects. Crosslinking is the major strategy to stabilize BICs for enzyme delivery, because release is usually not necessary for them to work.

1.4.2.1 Caging

BICs are known to protect the cargo proteins from proteolysis and aggregation induced by shear stress and temperature [90]. This is attributed to the steric repulsion provided by its hydrophilic corona against proteolytic enzymes and other proteins. Nonetheless, the highly hydrated nature of the coacervate core [17] allows for entry of small substrates and exit of products, which makes it a semi-permeable "cage" that allows the enzyme to be functional without being released out of the complex. The "cage" can be further fortified by chemical crosslinking and used for in vivo enzyme delivery [12, 13, 32, 91].

Formation of "cages" can also extend the circulation time of enzymes in vivo. The size of many proteins are smaller than the cut-off value of glomerular filtration (~45kD) and are therefore easily excreted from the kidney [92]. Some cationic proteins are quickly captured and removed by the mononuclear phagocyte system (MPS) and accumulate in the liver, spleen and lung shortly after administration [93]. Incorporation into "cages" effectively increases the

hydrodynamic size and shields the cationic charge of these enzymes, resulting in longer retention in the circulation.

1.4.2.2 Hyperactivation

Although enzymes can lose their activity towards large substrates (e.g. cell walls of bacteria [94]) owing to the caging effect, small substrates can usually diffuse into the coacervate core and access the active sites on the enzymes even after crosslinking [12, 70, 71, 95, 96]. Interestingly, sometimes compartmentalization of enzymes into BICs can lead to increased activity over their native counterparts, which is typically referred to as "hyperactivation" [70, 71, 97-100]. The mechanism for hyperactivation differs case by case, but typically involves contributions from the block copolymer. For example, PEG-PAsp has been proposed to increase trypsin activity by direct stabilization of its histidine residues at the active site through electrostatic interactions[100]. In another study, the activity of lysozyme was doubled after encapsulation into PEG-PAsp, attributing to the condensation of substrates in the hydrophilic corona of the BIC [70]. More recently, Kurinomaru et al studied the enzymatic activity of α-chymotrypsin and reported its increase by approximately 1 order of magnitude after complexation with polyelectrolytes of opposite charge to its substrates, suggesting a substrate accumulation mechanism by electrostatic attraction [98]. A similar but milder increase in activity was observed in Copper/Zinc superoxide dismutase after complexation with PEG-poly (L-lysine) [32, 63].

1.5 Conclusion

With decades of research directed towards understanding the process of complex coacervation between proteins and polyelectrolytes, we can now take advantage of this phenomenon to develop protein BICs for their delivery. The electrostatic nature of the interaction offers a gentle environment for protein packaging, as well as great flexibilities for the design and control of the physical properties of the BICs. By modulating the chemical

composition of polymers, crosslinkers, or even the surface residues on the proteins, this delivery system exhibits outstanding responsiveness to subtle environmental changes that are relevant to pathological states. One possible next step could be the functionalization of the BICs for cell-targeted delivery of proteins.

On the other hand, our understanding on the fundamental principles of protein BIC formation is still limited. Currently it is difficult to predict whether a BIC can form between a particular set of protein and polymer, and how stable they can be in a given environment due to the complexity of the system. This is can be hopefully achieved by in situ simulations with the rapid advancement of computing power.

CHAPTER 2 SOD1 NANOZYME SALVAGES ISCHEMIC BRAIN BY LOCALLY PROTECTING CEREBRAL VASCULATURE[2]

2.1 Summary

Copper/zinc superoxide dismutase (CuZnSOD; SOD1) is widely considered as a potential therapeutic candidate for pathologies involving oxidative stress, but its application has been greatly hindered by delivery issues. In our previous study, nano-formulated SOD1 (*cl*-nanozyme) was shown to decrease infarct volume and improve sensorimotor functions after single intravenous (IV) injection in a rat middle cerebral artery occlusion (MCAO) model of ischemia/reperfusion (I/R) injury. However, it remained unclear how *cl*-nanozyme was able to deliver SOD1 to the brain and exert therapeutic efficacy. Present study aims to answer this question by exploring micro-distribution pattern of *cl*-nanozyme in the rat brain after stroke. Immunohistochemistry studies demonstrated *cl*-nanozyme co-localization with fibrin along damaged arteries and capillaries in the ischemic hemisphere. We further found that *cl*-nanozyme can be cross-linked into thrombi formed after I/R injury in the brain, and this effect is independent of animal species (rat/mouse) used for modeling I/R injury. This work is also the first report reinforcing therapeutic potential of *cl*-nanozyme in a well-characterized mouse MCAO model of I/R injury.

2.2 Introduction

Stroke affects 7 million people, and continues to kill over a hundred thousand people annually in the United States alone [101]. Main causes of brain tissue damage during transient

[2] Part of this chapter previously appeared as an article in the Journal of Controlled Release. The original citation is as follows: *Jiang, Yuhang et al., J Control Release. 2015 September 10; 213: 36–44. doi:10.1016/j.jconrel.2015.06.021.*

ischemic stroke are ischemic and reperfusion injuries. Ischemic injury results from lack of glucose and oxygen when blood flow to the brain is blocked [102]. Reperfusion injury results from the detrimental action of reactive oxygen species (ROS) on brain tissue after blood flow is restored [103].

Antioxidant enzymes are endogenous tools for cells to scavenge ROS. However, their expression is often inhibited during stroke [104, 105], rendering antioxidant activity far less than sufficient for complete removal of excess ROS. Therefore, supplementation of antioxidant enzymes to the brain is a potential therapeutic strategy for this disease [106]. Their action would be especially beneficial for rescuing the salvageable penumbra since oxidative stress is the main mechanism of tissue damage in this area [107]. A direct use of anti-oxidant enzymes as therapy for stroke is not plausible because of its short half-life in the blood and poor permeability across the blood-brain barrier (BBB) and cellular membranes [108]. Even though BBB can be partially compromised during and after stroke, it still remains the key impediment for CNS transport of enzymes [109, 110]. Multiple strategies have been explored for delivery of functional antioxidant enzymes to the brain, including cationic liposomes, fusion proteins with peptide transduction domains, poly(ethylene glycol)-protein conjugates (PEGylated protein) and encapsulation into poly(lactic-co-glycolic acid) (PLGA) nanoparticles [111-118]. However, each of these approaches has limitations that precluded their successful clinical use as discussed in our previous work [32]. Briefly, loading of enzymes into solid or hollow nanoparticles often resulted in loss of activity and/or unsatisfactory loading efficiency (32% in the case of SOD1 liposomes [119]), and PEGylation usually decreases enzyme permeability across BBB [113].

We have demonstrated a different approach for encapsulation and delivery of antioxidant enzymes to the brain [32, 63, 120]. This approach is based on incorporation of an antioxidant enzyme, such as SOD1, into nano-sized polyion complexes with cationic block

copolymers ("nanozymes"). Nanozymes are core-shell structured nanoparticles with the polyion complex core consisting of charge-neutralized polycation chains and protein globules, and the shell consisting of PEG chains. Primary amine groups in the core were cross-linked (*cl*) using low molecular mass chemical cross-linkers to form *cl*-nanozyme and further purified to improve sample homogeneity by removing non-*cl*-nanozymes [32]. This formulation is essentially a covalently cross-linked polyion complex formed by SOD1 and methoxy-poly(ethylene glycol)-b-poly(l-lysine) (PEG-pLL, **Figure 2.1**).

Some of the key advantages of this strategy include high (100%) loading efficiency (owing to the formation of stoichiometric complexes) and instantaneous enzyme availability for catalysis precluding the need for its release, since superoxide anions are small enough to freely diffuse into the enzymatic core of the particle. This is a distinct advantage in scavenging ROS in the acute phase of diseases caused by oxidative stress, because the time window for antioxidant enzymes to work in these scenarios are usually narrow, and "fast acting" formulations like *cl*-nanozyme are consequently favored over those requiring drug release mechanisms.

The initial *in vivo* proof of concept for nanozyme transport to CNS was obtained by us using *cl*-nanozymes carrying butyrylcholinesterase, SOD1, or catalase [61, 63]. Compared to PEGylated SOD1 which poorly enters cells, SOD1 nanozyme was transported into neuronal cells and was superior to PEGylated SOD in depleting intracellular ROS and inhibiting Angiotensin II signaling *in vitro* and *in vivo* [121, 122]. Catalase nanozymes demonstrated neuroprotective effects in an animal model of Parkinson's disease (PD) [123, 124]. Our most recent results demonstrated the therapeutic efficacy of purified SOD1 *cl*-nanozyme in a rat middle cerebral artery occlusion (MCAO) model of I/R injury [32] by decreasing infarct volume and improving sensorimotor functions after a single IV bolus. Similar to other reports using nano-formulated SOD1 for the treatment of stroke [115, 118], we did not specifically

investigate how this approach was able to exert the observed therapeutic effect [32]. However, understanding this mechanism can be essential for improving therapeutic potential of SOD1 nanozyme formulation and for discovery of more applications of the nanozyme delivery platform.

In the present work, we demonstrate that *cl*-nanozyme accumulated predominantly within the injured vasculature and co-localized with fibrin after stroke. This suggests one possible mechanism where *cl*-nanozyme passively target to damaged brain vasculature, and locally protect the neurovascular unit as an entire entity. To evaluate this finding from a translational perspective and investigate the validity of our findings in another animal model, we tested the same *cl*-nanozyme formulation in a well-characterized mouse model of stroke, and again observed significant reduction of infarct size. *In vitro* thrombus incorporation assay in the mouse plasma further supported our major hypothesis that *cl*-nanozyme can be actively incorporated into growing thrombus formed during or after stroke.

2.3 Materials and Methods

2.3.1 Materials.

3,3'-Diaminobenzidine (DAB), SOD1, and 2,3,5-triphenyltetrazolium chloride (TTC) were purchased from Sigma-Aldrich. PEG_{113}-pLL_{51} was purchased from Alamanda Polymers™; Bovine serum albumin (BSA), ethanol, ethylenediaminetetraacetic acid (EDTA), 3,3′-dithiobis(sulfosuccinimidylpropionate) (DTSSP), 10% neutral buffered formalin, trichloroacetic acid (TCA) were purchased from Thermo Fisher Scientific. AlexaFluor® secondary antibodies, and Hoechst 43580 were purchased from Life Technologies; C57BL/6 mouse plasma was purchased from Molecular Innovations. All reagents and chemicals were used as received.

2.3.2 Synthesis of *cl*-nanozyme.

Cl-nanozyme was synthesized at the polycation to SOD1 charge ratio $Z_{+/-}$=2 using DTSSP as a cross-linker as previously described [32]. After synthesis and desalting (to remove unreacted DTSSP), *cl*-nanozyme was purified to separate the cross-linked from the non-cross linked species. For the purification, *cl*-nanozyme in 10 mM HEPES buffer containing 0.3 M NaCl (pH=7.4) was loaded onto Macrosep centrifugal device (Pall Corporation, MI) and concentrated twice to about 10% of its initial volume by centrifugation at 4,500 rpm at 4 °C. The concentrate was collected and desalted using NAP™ columns to remove excess NaCl. The eluent was then collected in 10 mM HEPES buffer containing 0.15 M NaCl (pH=7.4). SOD1 enzyme activity was determined using a microplate version of PG assay [32], and normalized to protein content determined by Inductively Coupled Plasma Mass Spectrometry (ICP-MS) using copper and zinc as standards. Particle effective diameter (*z*-average hydrodynamic diameter) and polydispersity index (PDI) were measured using a Malvern Zetasizer Nano (Malvern Instruments Ltd., MA). The resulting *cl*-nanozyme had a particle diameter of 39.2 ± 0.8 nm (PDI < 0.1), and retained 58.6 ± 9.5% enzyme activity relative to native SOD1.

2.3.3 Animals.

Charles River Laboratories supplied 8-week-old male Sprague-Dawley rats (250-300 g), and 12-week-old male C57BL/6 mice (20-28 g). Animals were housed and humanely handled in accordance with the Principles of Animal Care outlined by National Institutes of Health. They were allowed free access to food and water and were maintained under temperature, humidity, and light-controlled conditions. Institutional Animal Care and Use Committees (IACUC) of University of Nebraska Medical Center (UNMC) and the University of North Carolina at Chapel Hill approved all experiments involving animal subjects.

2.3.4 MCAO model of transient ischemic stroke in rats.

Brain ischemia was modeled by transient MCAO method as described previously [125]. Rats were anesthetized with ketamine (80 mg/kg) and xylazine (5 mg/kg) cocktail and isoflurane (5% v/v for induction and 0.5% v/v during surgery). Rectal temperature was maintained at about 37 °C throughout the surgery using a homoeothermic monitor (Harvard Apparatus, UK). Animals were prepared for surgery according to IACUC recommendations. The right common carotid artery was exposed and occluded using a silicon rubber-coated monofilament for MCAO. Filament was inserted through the incision into internal carotid artery (ICA) and further until reaching the bifurcation of MCA. Tip occluded the entrance to MCA and blocked blood supply to part of the right brain hemisphere (referred to as the ischemic hemisphere). Filament was carefully withdrawn after 1 hour. Sham surgery was performed as described above without filament insertion. After the surgery, animals were returned to their cages and allowed free access to water and food. At the time of reperfusion, 10,000 U/ kg of native SOD1 or *cl*-nanozyme (n = 10 in each group) were IV injected under anesthesia. Rats were sacrificed 3 or 24 h post-reperfusion, and perfused with 4% paraformaldehyde solution for histology analysis.

2.3.5 Histology and Immunohistochemistry.

Tissue toxicity of *cl*-nanozyme was assessed by hematoxylin and eosin (H&E) staining of liver, spleen, kidney, and lung tissues. Tissue samples were dissected and fixed in 10% neutral buffered formalin before embedded in paraffin. Five μm thick tissue sections were processed and stained according to standard protocol used by Tissue Sciences core facility at UNMC. *Cl*-nanozymes were visualized in peripheral organs using DAB. Tissue samples were prepared as described above. For detection of *cl*-nanozyme in liver, spleen, kidney, and lung, respective tissue sections were incubated at 4 ^{o}C overnight with rabbit anti-PEG antibody (1:500, Abcam, MA), followed by incubation with secondary biotinylated goat anti-mouse

antibodies and VecStain Elite kit (Vector Laboratories, CA). DAB color generation system was used as described previously [126] for chromogenic visualization. Fluorescent immunohistochemistry study was performed on tissues perfused with PBS followed by 10% neutral buffered formalin. To visualize *cl*-nanozyme in the liver and brain, tissue sections were stained using rabbit anti-PEG antibody (Abcam, CA) diluted 1:200 and 1:100, respectively. Hepatocytes were detected with polyclonal chicken anti-albumin antibody (1:100, Sigma Aldrich, MO). $CD68^+$ cells in the brain (infiltrating monocytes), liver (Kupffer cells) and spleen (splenic macrophages) were visualized using monoclonal mouse anti-CD68 antibody (1:40 Abcam, MA). Brain microvessels were visualized using monoclonal mouse anti-CD31 antibody (1:30, AbD Serotec, NC); neurons were visualized using monoclonal mouse anti-neurofilament 70kDa (NF-L) antibody (1:200, Millipore, CA); fibrin deposits after stroke were visualized using mouse anti-fibrin antibody (1:50, Abcam, MA). Treatment with primary antibodies was followed by treatment with secondary antibodies: AlexaFluor 594 goat anti-chicken, AlexaFluor 594 goat anti-mouse, and AlexaFluor 488 goat anti-rabbit, and AlexaFluor 647 goat anti-mouse. Nuclei were visualized using 2.5μg/ml Hoechst 43580 solution. Immunofluorescence were detected using Zeiss 710 Confocal Laser Scanning Microscope and images were analyzed using Zeiss Zen software and ImageJ software (National Institute of Health, MD).

2.3.6 Preparation of 125I-labeled Proteins and *cl*-nanozyme.

Native SOD1, fibrinogen, BSA, or *cl*-nanozyme were radioactively labeled with ^{125}I using chloramine-T method as previously described [127]. Briefly, 5 μg of protein or equivalent amount of *cl*-nanozyme was mixed with 0.5 mCi $Na^{125}I$ (PerkinElmer, MA) in a final volume of 40 μL in sodium phosphate buffer (0.25 M, pH=7.5). Five μL freshly-made chloramine-T solution (2 μg/μL in sodium phosphate buffer) was added to the mixture. After 60 s incubation under constant mixing, the ^{125}I-labeled samples were purified using Illustra

NAP-5 desalting columns (GE Healthcare, NJ). Fractions were collected in Eppendorf tubes pretreated with 1% BSA in Lactated Ringer's solution (1% BSA-LR) to prevent non-specific adsorbance. Radioactivity was measured using a PerkinElmer γ-counter. TCA precipitation was conducted to determine the ^{125}I association of labeled samples. Briefly, 1 µL of collected fractions was added to 0.5 mL of 1% BSA-LR and then precipitated in 0.5 mL of 30% TCA followed by centrifugation at 5000 *x*g for 10 min at 4 °C. The resulting supernatant and pellet were measured in the γ-counter and the values were used to calculate the %radioactivity that precipitated with acid (% protein bound-^{125}I = [CPM_{pellet} /(CPM_{pellet} + $CPM_{supernatant}$)]*100%). Samples containing >100,000 cpm/µL of radioactivity and > 90% TCA precipitation were used for animal studies.

2.3.7 Biodistribution and Serum Clearance in Mice.

Twelve-week-old male C57BL/6 mice were anesthetized by intraperitoneal (IP) injection of 0.2 mL of urethane (4.0 g/kg). Approximately 500,000 CPM of radiolabeled samples were injected IV via the jugular vein with 0.2 mL of 1% BSA-LR. For the biodistribution study, the abdomen and rib cage were opened and venous blood was collected by cardiac puncture 1 hour post-injection. Then, 20 mL of PBS was perfused through the left ventricle of the heart. At the end of study, organs were dissected and wet-weighed. For the serum clearance study, blood from the pre-exposed carotid artery was collected at various time points after injection. Serum was separated from whole blood by centrifugation at 5400 *x*g for 10 min at 4 ^{o}C. Levels of radioactivity were measured in the γ-counter. To calculate serum clearance, the level of radioactivity was expressed relative to the amount injected (%Inj/mL) and these values were plotted against time (min) to construct the serum concentration vs. time curve.

2.3.8 MCAO Model of Transient Ischemic Stroke in Mice.

All mice were randomly assigned before surgery into one of the following groups: *cl*-nanozyme-treated group (n = 8), native SOD1-treated group (n = 8), or saline-treated group (n = 7). The mice were weighed and were subjected to 90 min of ischemia under isoflurane anesthesia (5% v/v for induction and 1.5% v/v during surgery) as previously described [128]. Briefly, rectal temperature was monitored maintained at approximately 37 °C during surgery using a homoeothermic heating system. A midline ventral neck incision was made, and unilateral MCAO was performed by inserting a silicone rubber coated monofilament into the right internal carotid artery 6 mm from the internal carotid/pterygopalatine artery bifurcation via an external carotid artery stump. At the time of reperfusion, 10,000 U/ kg of treatment solutions were IV injected under anesthesia.

2.3.9 TTC Staining and Brain Infarct Volume Quantification.

After 90 minutes of ischemia and 24 hours of reperfusion, the mice were euthanized and the brains were chilled at -80 °C for 4 minutes to slightly harden the tissue. Five 2-mm-thick coronal sections were cut from the olfactory bulb to the cerebellum and then stained with 1.5% TTC in PBS (pH=7.4). The sections in TTC solution were incubated in a water bath maintained at 37 °C for 30 minutes, then transferred to a 10% phosphate-buffered formalin solution and incubated overnight at 4 °C before pictures were taken for analysis. The infarct volumes were calculated blinded to the treatment given, and the infarct size in each of the five slices was quantified using the Image J software. In addition to total hemisphere, the infarct areas were determined separately for cortex and caudoputamen in each slice. Then the infarct areas on each slice were summed up and multiplied by thickness to calculate infarct volumes. The infarct volumes were calculated using Swanson's method [129] and processed as % contralateral hemisphere to avoid mis-measurements secondary to edema.

2.3.10 Thrombus Incorporation Assay in Mouse Plasma.

One hundred thousand CPM of ^{125}I-labeled fibrinogen, BSA, native SOD1, and *cl*-nanozyme were added into an Eppendorf tube containing 1 mL C57BL/6 mouse Lithium heparin-stabilized plasma (Innovative Research, MI). Half mg of protamine sulfate was then added to neutralize heparin and allow thrombus formation. The tube was incubated on a rotary-shaker for 24 h at 4 °C before centrifugation at 5000*x*g for 10 min. Serum was separated from the white thrombus at the bottom of the tube, and then subjected to TCA precipitation assay to correct for error caused by ^{125}I dissociation during incubation as described above. Percentage of samples sequestered in the thrombus compartment were calculated using the following formula: %Thrombus Incorporation = $[CPM_{thrombus} /(CPM_{thrombus} + CPM_{serum})]*100\%$.

2.3.11 Autoradiography

For autoradiography experiments, ^{125}I-labeled *cl*-nanozyme was IV injected in mice with either a MCAO surgery at the onset of reperfusion or a sham surgery. The mice were sacrificed and perfused with PBS 1 hour after injection. Their brains were then harvested, snap-frozen with dry ice, and cut into 50 μm-thick coronal sections before exposing it for 73 days before read on an autoradiography imager.

2.3.12 Statistical Analysis.

The randomization code was broken in the mice stroke therapeutic efficacy study after acquiring all the data. Statistical analysis was done using Prism 5.0 software (GraphPad, CA). Unpaired Student's t-test was used for two groups, and one-way ANOVA followed by Tukey's multiple comparison test for groups of three and above. A minimum p-value of 0.05 was estimated as the significance level. Results of all experiments are presented as mean ± standard error of the mean (SEM).

2.4 Results

2.4.1 *Cl*-nanozyme Tissue Distribution in the Rat MCAO Model of I/R Injury

In our previous paper [32] reporting synthesis and purification of *cl*-nanozyme, we have demonstrated decreased infarct volume and improved sensorimotor functions after a single IV injection in a rat MCAO model. To gain insight into the mechanism of *cl*-nanozyme's therapeutic efficacy, we studied its micro-distribution in the same model. Immunohistochemistry (IHC) analysis revealed accumulation of *cl*-nanozyme primarily in the ipsilateral hemisphere in the area of infarct at 3h post-reperfusion. (**Figure 2.2**).

Cl-nanozyme localized primarily within blood vessels, as shown by fluorescent double staining for *cl*-nanozyme and endothelial marker PECAM-1 in **Figure 2.3 A**. *Cl*-nanozyme staining outside the blood vessel in brain parenchyma was primarily seen in the infarct region of the ipsilateral hemisphere. *Cl*-nanozyme co-localized with neither neurons nor activated mononuclear phagocytes (**Figure 2.2**).

We further hypothesized that *cl*-nanozyme co-localize with damaged blood vessels, since its signal was most prominent in infarct regions. Evidence for this hypothesis is shown in **Figure 2.4**. During the MCAO procedure, occlusion is created by filament insertion into the lumen along the internal carotid artery. **Figure 2.4 A** is a confocal micrograph of a coronal brain section across a portion of internal carotid artery where the filament tip was positioned (**Figure 2.4 D**).

The filament tip had damaged the artery during filament insertion and/or occlusion, as suggested by discontinuous nuclear staining around the luminal side of the artery (**Figure 2.4 C**), and *cl*-nanozyme co-localized with these damaged portions of the artery (**Figure 2.4 B, C**). No *cl*-nanozyme signal was observed in the contralateral hemisphere where the internal carotid artery was not damaged, as shown in dotted box, **Figure 2.4 B**. In infarcted brain regions, *cl*-nanozyme co-localized with fibrin, a protein involved in blood clotting (**Figure 2.3 B, C**),

which further supports our hypothesis that *cl*-nanozyme localizes in damaged blood vessels. Interestingly, while most *cl*-nanozyme signal co-localized with fibrin, not all capillaries with fibrin deposition sites showed *cl*-nanozyme accumulation (**Figure 2.3 C**).

Peripheral organs were collected 24 hours after reperfusion, and histological examinations was performed to qualitatively study the disposition and any possible toxicity effects of *cl*-nanozyme. H&E-stained tissue sections did not reveal any sign of acute toxicity (**Figure 2.5**). Analysis of *cl*-nanozyme distribution in select peripheral organs confirmed its presence in the liver and spleen, but not in lungs or kidneys at this time point (**Figure 2.6 A**). Triple fluorescent immunostaining of the liver tissue revealed co-localization of *cl*-nanozyme with hepatocytes and Kupffer cells (**Figure 2.6 B**). We noticed intense *cl*-nanozyme staining in areas between two adjacent hepatocytes indicative of its deposition in the bile canaliculi, suggesting a potential clearance mechanism via bile excretion. In addition to their intracellular accumulation in hepatocytes, *cl*-nanozymes were also observed in liver sinusoids.

2.4.2 *Cl*-nanozyme Biodistribution and Serum Clearance in Mice

We studied biodistribution of native SOD1 and *cl*-nanozyme in healthy C57/B6 mice to determine the effects of formulating SOD1 on its biodistribution. One hour after injection, *cl*-nanozyme was found to accumulate in liver and spleen in significantly higher amounts than native SOD1, displaying 25- and 38-fold increases, respectively (**Figure 2.7 A**). Changes in SOD1 accumulation in most other peripheral organs including heart, lung, and spine were significant but less drastic (less than 4-fold increase) compared to liver and spleen. However, *cl*-nanozyme accumulation in kidney was reduced by more than half compared to native SOD1 (35.4% vs. 88.3%). Notably, the brain uptake of *cl*-nanozyme was 2-fold higher than native SOD1 (0.0809% vs. 0.0406%) in healthy mice.

First-order kinetics was observed in the early phase of clearance for both substances, demonstrated by the statistically significant relation between log(%Inj/mL) and time (**Figure**

2.7 B). Serum half-life ($t_{1/2}$) of native SOD1 and *cl*-nanozyme was 10.3 min and 33.8 min respectively, suggesting prolonged SOD1 circulation after formulation.

2.4.3 Therapeutic Effect of *cl*-nanozyme in Mouse MCAO Model of I/R Injury

Cl-nanozymes administered at the onset of reperfusion in a mouse MCAO model of I/R injury resulted in reduced infarct volumes compared to groups treated with saline or native SOD1. Significantly reduced infarct volume was observed in all three brain regions analyzed (cortex: 35.0±7.0%; caudoputamen: 13.0±4.7%; hemisphere: 28.1±5. 6%) compared to those injected with saline (cortex: 69.8±3.7%; caudoputamen: 73.7±6.0%; hemisphere: 61.5±6.8%) and native SOD1 (cortex: 59.3±7.7%; caudoputamen: 78.9±6.5%; hemisphere: 57.1±6.9%), as shown in **Figure 2.8**. The mean infarct volume was slightly lower in the native SOD1-treated group than in saline-treated group, albeit this difference was not statistically significant. Interestingly, the protective effect of *cl*-nanozyme appears to be stronger in the caudoputamen area than in the cortex or entire hemisphere.

2.4.4 Thrombus Incorporation Assay

To directly evaluate the ability of *cl*-nanozyme and native SOD1 to be incorporated into white thrombi, we performed an *in vitro* thrombus incorporation assay using mouse plasma. After 24 h incubation at 4 ^{o}C, incorporation of native SOD1 into the thrombi (4.4±0.4%) was not significantly different from that of the negative control, BSA. However, significantly more *cl*-nanozyme (8.2±0.2%) was sequestered in the thrombus compartment (**Figure 2.9**). Fibrinogen was used as a positive control and showed 52±4% accumulation in the thrombi.

2.5 Discussion

Cl-nanozyme for delivery of antioxidant enzymes has been successfully used by us previously for the treatment of multiple pathologies involving oxidative damage [32, 120-124, 130]. Specifically, its therapeutic effect in decreasing the infarct volume and improving sensorimotor functions upon single IV injection in a rat stroke model was demonstrated in our

laboratory [32]. The present study continues to explore the mechanism by which *cl*-nanozyme exerted therapeutic efficacy.

The structure of *cl*-nanozyme does not include a brain targeting moiety. Thus, we did not expect it to cross a healthy BBB. Initially we believed that *cl*-nanozymes could possibly enter the brain via the disrupted BBB, a well-characterized phenomenon after brain I/R injury [131-133]. To our surprise, despite the observed therapeutic efficacy in the stroke model, we did not observe substantial evidence of *cl*-nanozyme crossing the BBB. In the IHC experiments, we did observe a considerable amount of *cl*-nanozyme signal associated with the infarct region of the brain, where the BBB is supposed to be disrupted. However, the majority of the signal was not associated with neurons or activated macrophages, but trapped inside the lumen of blood vessels. Although by design, our study does not exclude the possibility of a small portion of *cl*-nanozyme crossing the BBB and exerting therapeutic effect, the hypothesis of thrombus accumulation is apparently more plausible based on our observations. It also serves better on explaining why *cl*-nanozyme shows much better therapeutic efficacy compared to native SOD1, which can be tricky to explain based solely on the BBB disruption theory.

Our thrombus incorporation hypothesis is derived from the chemical composition of *cl*-nanozyme, with its core structure being charge-neutralized pLL/SOD1 complex. The monomer of pLL, ϵ-lysine is capable of cross-linking into the thrombus by participating in biochemical reactions accompanying its formation [134]. Briefly, blood vessel damage activates platelets and initiates a cascade of tissue factor (TF) activation, which converts TFXIII to its active form, TFXIIIa. TFXIIIa is a transglutaminase which cross-links glutamine with the ε-amine group of lysine. Indeed, pLL has been proved to be a good substrate for transglutaminase and this reaction has been utilized to enzymatically produce pLL-protein conjugates [135]. Therefore it is not surprising to see this reaction occurring *in vivo*.

IHC data in the rat model strongly supported the thrombus incorporation hypothesis. *Cl*-nanozyme was detected primarily in the infarct region in association with endothelial cells of the damaged brain vasculature. Intense *cl*-nanozyme signal was observed only in areas surrounding the injured internal carotid artery, but not the healthy one in the contralateral hemisphere (**Figure 2.4 B**), confirming the selective nature of the association between *cl*-nanozyme and damaged blood vessels. Evidence of *cl*-nanozyme and thrombus crosslinking was further supported by the co-localization of *cl*-nanozyme with fibrin, a major component in blood clots, in the capillaries of the infarct region.

Beyond the brain, we have also examined *cl*-nanozyme distribution in select peripheral organs. H&E data suggested that *cl*-nanozyme is not noticeably toxic after *in vivo* administration. This is a promising observation that supports further development of such nanoparticles for stroke therapy. IHC experiments found massive distribution of *cl*-nanozyme into liver and spleen. This is generally in agreement with the known function of these organs in clearing particulate matter. Interestingly, a closer look at the liver slices revealed distribution of *cl*-nanozyme not only in Kupffer cells, but also in tube-shaped territories between two adjacent hepatocytes that resemble bile canaliculi. This particular staining pattern possibly indicates that *cl*-nanozyme is excreted through bile as part of its metabolic pathway. What we have detected in these structures is more likely to be metabolic products than intact *cl*-nanozymes, especially considering the time point of analysis (24 h after reperfusion) and the cleavable disulfide bond present in the cross-linker (DTSSP) used in this formulation. Notably, the rat liver has been reported to have rather high concentrations (10 mM) of reduced glutathione known to participate in disulfide reduction, which thereby may enhance degradation of the *cl*-nanozyme in the liver [32]. In addition to intra-hepatocyte accumulation, staining was also observed in the liver sinusoids. Considering the $t_{1/2}$ of *cl*-nanozyme (33.8 min in mouse), it is unlikely that level of *cl*-nanozyme in the blood is high at this time point, i.e. 24

h after administration. Presence of *cl*-nanozyme in liver sinusoids may result from pLL binding to liver tissue, possibly via the same mechanism by which they bind to damaged blood vessels in the brain, since most of the blood coagulation proteins are synthesized in the liver [136].

These results in the rat MCAO model indicate that the therapeutic effect of *cl*-nanozyme can be attributed to its specific accumulation into damaged blood vessels in the infarct region. In events where blood vessels were damaged, intrinsic mechanisms of thrombosis could take place and actively recruit *cl*-nanozyme into them, thereby effectively reducing oxidative stress generated at the vicinity of damaged sites. Such blood vessel damage could result either from mechanical force (filament damaging ICA) or I/R injury (endothelium damage), both occurring in the MCAO model of stroke and the latter can also take place after transient stroke suffered by human subjects [137]. Since this mechanism appears to be translatable to human patients, we moved forward and investigated utility of *cl*-nanozymes in a different species to determine if similar therapeutic outcomes can be achieved in the mouse model of I/R injury. Indeed, this work is the first report reinforcing therapeutic potential of *cl*-nanozyme in a well-characterized mouse MCAO model [138].

Before evaluating *cl*-nanozyme in the mice MCAO model, we first conducted a comprehensive study to determine *cl*-nanozyme biodistribution in the early phase (1h) after injection. Similar to the rat model, we observed significantly increased sequestration of *cl*-nanozyme in the liver and spleen compared to native SOD1. Reduced uptake of *cl*-nanozyme in the kidney compared to that of native SOD1 (32 kDa) is in general agreement with the known function of kidney (glomerular filtration) in clearing small molecules with a molecular mass cutoff of ~40 kDa. Tissue distribution of protein is generally increased after formulation in most other organs, including a significant 2-fold increase in the brain. This increase probably resulted from a combination of decreased kidney accumulation and increased serum half-life as shown in **Figure 2.7 B**.

Remarkably, *cl*-nanozyme administration resulted in significant reduction of infarct size in the mouse MCAO model compared to the native SOD1 group reinforcing its therapeutic potential in a second rodent model. Formation of micro-thrombi in capillaries after MCAO surgery is a well-documented phenomenon in rodent MCAO models [137, 139, 140]. Specifically, Zhang and colleagues [141] reported fibrin deposition primarily in the sub-cortex region after acute ischemic stroke, which may explain why therapeutic effect of *cl*-nanozyme is more pronounced in the caudoputamen compared to the cortex. Therefore, we speculate that the mechanism of action of *cl*-nanozyme involves local protection of cerebral vasculature. Since the damaged brain endothelium in I/R injury is a site of intense ROS production [142], retention of *cl*-nanozyme in the sites of vascular damage and thrombus formation can facilitate its ability to scavenge local ROS and to subsequently mitigate detrimental effects of ROS on vasculature. Autoradiography results suggest clear differences in the distribution pattern of *cl*-nanozyme injected before and after stroke (Figure 2.10 Autoradiography of brain slices after IV injection of ^{125I} labelled *cl-nanozyme***Figure 2.10**). The distribution of *cl*-nanozyme in the stroke brain spreads the entire stroke hemisphere, while in the healthy brain they appears to be restrained in the brain ventricles.

From a translational research perspective, clinically, different factors can contribute to local thrombus formation during the reperfusion phase of focal cerebral ischemia, as described by Virchow's triad: reduction in cerebral blood flow, damage to the vessel wall, and hypercoagulability. These events can contribute to the occurrence of focal "no-reflow" phenomenon [143] and even thromboembolic complications in the sub-acute phase of ischemic stroke [144]. In our thrombus incorporation study, we clearly demonstrated that *cl*-nanozyme can be actively incorporated into thrombus during their growth. This experimental set up is a simplified model where only white thrombi are formed. It can be postulated that in the scenario of clinical stroke where body temperature, blood cells, and platelets are all contributing to

thrombus formation, the rate and extent of *cl*-nanozyme incorporation into thrombus could be faster and greater. By exploiting the "no-reflow" phenomenon and by passively accumulating at the site of injured arteries and microvessels after reperfusion, it is not surprising that *cl*-nanozyme exerted better therapeutic outcomes than native SOD1. Furthermore, passive targeting to sites of thrombus formation may open avenues for the delivery of agents that protect the endothelium from negative side effects of thrombolytics such as recombinant tissue plasminogen activator (rt-PA).

Two key works reported the use of particulate carriers for the delivery of SOD1 to treat stroke. Reddy and Labhasetwar demonstrated a 65% decrease in infarct volume compared to saline-treated group when SOD1 encapsulated in PLGA nanoparticles (NPs) was delivered via intracarotid (IC) injection to a rat MCAO model of stroke [115]. Interestingly, they also showed increased accumulation of HRP-loaded NPs in the ischemic hemisphere compared to its non-ischemic counterpart similar to our observation on increased accumulation of *cl*-nanozyme in the ischemic hemisphere. The authors pointed out the need for further research to understand the mechanism of NP-mediated protection. Yun *et al*. also showed a 50-60% decrease in infarct volume when SOD1 was delivered (again via the IC route) using 3 different nanoparticle platforms (liposomal SOD1, Polybutylcyanoacrylate-SOD1 and PLGA-SOD1 particles) in a mouse MCAO model of stoke [118]. SOD1 was conjugated to the distal end ($mPEG_{2000}$-DSPE) of liposomes prepared using phosphatidylcholine, cholesterol, mPEG2000-DSPE, and MAL-PEG2000-DSPE (molar ratio of 55:39:4:2). These carriers were modified with anti-NMDA receptor antibodies for brain targeting, and was shown to protect the ischemic regions by suppressing caspase-3 activation.

Although the present study is not unique in exploring therapeutic effect of SOD1 nano-formulations, it draws attention to the delivery of therapeutics to the neurovascular unit as a whole and in particular to the damaged brain endothelium, rather than neurons alone. Often

researchers focus extensively on the delivery of therapeutics across the BBB to the brain parenchyma, a task that remains a formidable challenge in most cases. However, it can be not as formidable to target therapeutics to the BBB itself. Indeed, homeostatic interactions exist between endothelium and cerebral parenchyma, and the BBB has been considered to be neuro-protective on its own by excreting neurotrophic factors in response to injury [145]. Our observations document that *cl*-nanozyme accumulates into damaged brain vasculature regions and probably exerts its effect mainly on brain vasculature rather than the parenchyma. It provides evidence that targeting therapeutics to the BBB itself could also be a viable therapeutic strategy. Another advantage of our approach is the use of IV administration route, which can be more desirable than IC from a translational perspective. This is made possible collaboratively by increased serum half-life and additional local retention at the damaged sites of vasculature. Moreover, our approach of drug administration after ischemic episode, as opposed to pretreatment with SOD1 formulations, as reviewed by Margaill *et al*.[106], is advantageous from translational standpoint as well.

2.6 Conclusion

In conclusion, the present study demonstrates the ability of *cl*-nanozyme to accumulate in damaged blood vessels. This allowed therapeutic cargo to exert its effect at the interface of blood and brain especially vulnerable to oxidative stress in stroke. We believe that *cl*-nanozyme is a promising delivery strategy that can find application in the therapy of cerebrovascular conditions associated with oxidative stress and inflammation. Evaluation of *cl*-nanozyme safety and efficacy in alternate models of transient ischemic stroke, e.g. MCAO procedure conducted on aged animals and/or animals with co-morbidities, is essential for further validation of the translational potential of this work.

2.7 Future directions

In this work we use an ischemic-reperfusion model to demonstrate the ability of *cl*-nanozyme to locally protect the blood vessels in the brain against reperfusion injury. This model has intrinsic limitations in its translational potential. For example, this model utilizes a surgical filament to mimic the blockage of the blood vessel and the thrombolysis process during stroke, and the thrombolysis is complete since they are induced by removal of the filament. In clinical practice, however, thrombolysis is usually performed by infusion of recombinant tissue plasminogen activator (rtPA) [146]. Therefore, the scenario where a stroke patient receives complete blood reperfusion is not common. Many of them has only partial reperfusion after treatment, and some of the patients might not even be eligible for rtPA treatment if they were hospitalized too late. Consequently, it would be very attractive to test *cl*-nanozyme in other stroke models than the one we are currently using.

Such studies can also provide valuable information on indirect mechanisms for stroke pathology as well as on broadening the range of indications of *cl*-nanozyme in stroke treatment. In a permanent occlusion model where the blood vessel is blocked for the entire duration of study, the damage mechanism would be completely different [147] and IV infusion of *cl*-nanozyme could be explored as a strategy to inhibit systemic ROS signaling and subsequent immune responses. An embolus or laser-induced stroke model followed by rtPA infusion could mimic a more clinical-relevant scenario where more variables are introduced, such as the patient response to anti-thrombolytic therapy, the time between stroke and treatment, and the risk of rtPA-related hemorrhagic transformation. In these models, more therapeutic potentials of *cl*-nanozyme can be possibly explored, e.g. to extend the therapeutic window of rtPA, or as a pre-treatment before a stroke attack.

If *cl*-nanozyme proves to work in these models, it will likely involve other mechanisms than the one we demonstrated in this chapter. Indeed, as an anti-oxidant enzyme formulation,

it is probably for *cl*-nanozyme to work through multiple pathways. One possibility would be the blockage of immunological cascade after stroke since ROS have been demonstrated to activate extensive immune response which exacerbates stroke damage. Another possible pathway is by inhibiting iron-catalyzed ROS production, since red blood cells contain a large amount of iron, which can promote the production of ROS as a catalyst after lysis of the cell.

Another limitation of this work relates to the strategy of using SOD as the therapeutic agent, since SOD is known to cause toxicity at higher dose and therefore can generate a "bell-shaped" dose-response curve. Concerns with SOD overdose can be traced back to the year 1973 when Fridovich and Hodgson demonstrated that SOD-catalysed dismutation reaction of O_2^- was reversible according to thermodynamics [148] and reported inactivation of Cu,Zn-SOD by H_2O_2 [149] as well as the peroxidation mediated by SOD on a wide variety of compounds [150]. The mechanism they proposed involved the reduction of the SOD Cu^{2+} to Cu^+ by H_2O_2 followed by Cu^+ mediated Fenton's type reaction with extra H_2O_2 to form $OH^{\cdot}$, which further oxidatively attacks an adjacent histidine and thus inactive the enzyme. This hypothesis was proved acceptable by many investigators later [151-153]. After the year 2000, another important factor HCO_3^- was proved to play a vital role in Cu,Zn-SOD related peroxidation reactions [154, 155]. This made Dr. Fridovich write another paper[156] 30 years later to revisit his work published in 1973 [148].

However, the Cu-Zn SOD toxicity could not fully explain a series of bell-shaped dose-response curves in vivo [157-159], because Mn SOD, which is not supposed to have peroxidase function, also showed similar dose-responses curves [160]. Some researchers believed it was trace amount of iron in vivo, maybe released from apoptotic cells that mediated similar Fenton's type reactions [152]. Many researchers therefore highly recommended combination delivery of SOD and Catalase, and make sure they are close enough so H_2O_2 can be eliminated as soon as possible [152, 153].

Another explanation for SOD toxicity is related to termination of lipid peroxidation. Basically, lipid peroxidation is a radical chain reaction initiated in vivo mostly by superoxide radical anions during stroke. Ironically, the only way to eliminate a radical is by reacting it with another radical, and the presence of superoxide itself as a relatively unreactive radical could be a perfect terminator for the lipid peroxidation chain reaction [161].

With the above information in mind, it is necessary to consider this effect when high dose of *cl*-nanozyme is to be used for the treatment of any disease.

Last but not least, it is necessary to emphasize the known toxicity of poly-L-lysine for in vivo application. In the case of stroke, it is acceptable since this is an acute administration for a life-threatening condition. However, a replacement of this polymer is needed if we want to develop this formulation for the treatment of chronic diseases with repeated dosing regimens.

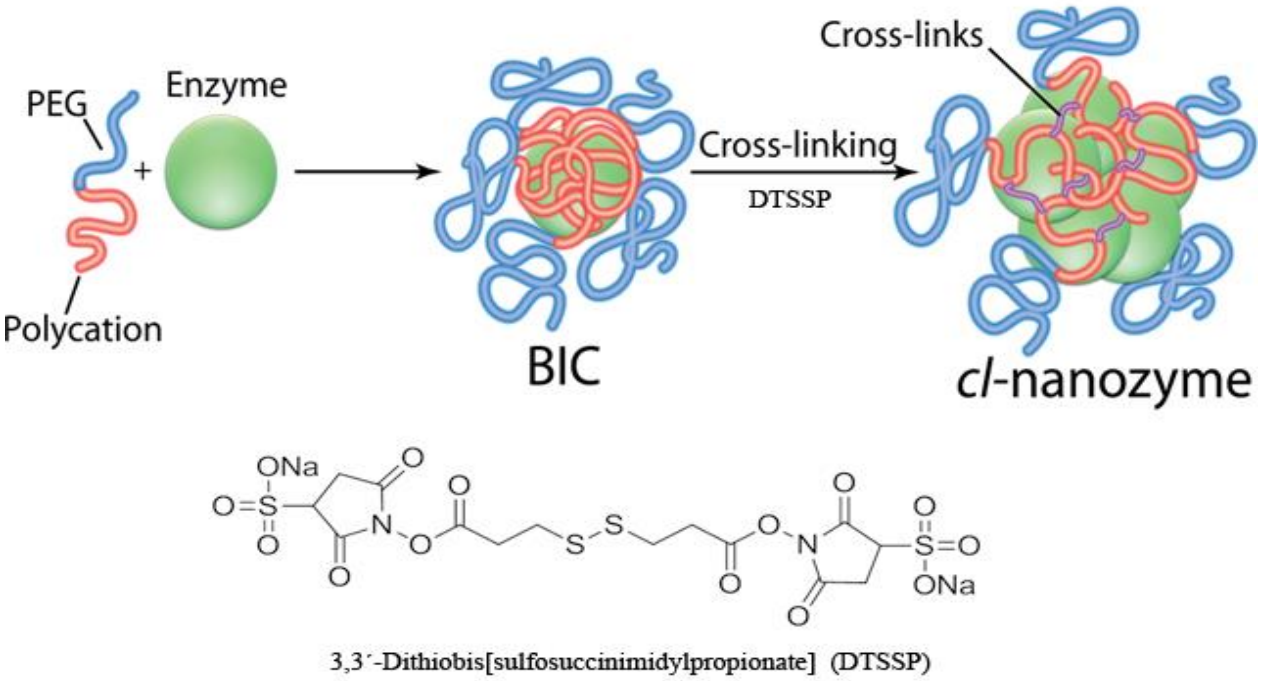

Figure 2.1 Schematic representation of *cl*-nanozyme

This is a schematic representation of *cl*-nanozyme synthesis. Block ionomer complexes (BIC) form due to spontaneous self-assembly resulting from electrostatic binding of negatively-charged enzyme (SOD1) with cationic block copolymer (PEG-pLL) to which DTSSP is added to covalently stabilize the BIC by cross-linking primary amine groups. This figure is reproduced from our previous publicatoin [32] to present a general idea of the *cl*-nanozyme's structure.

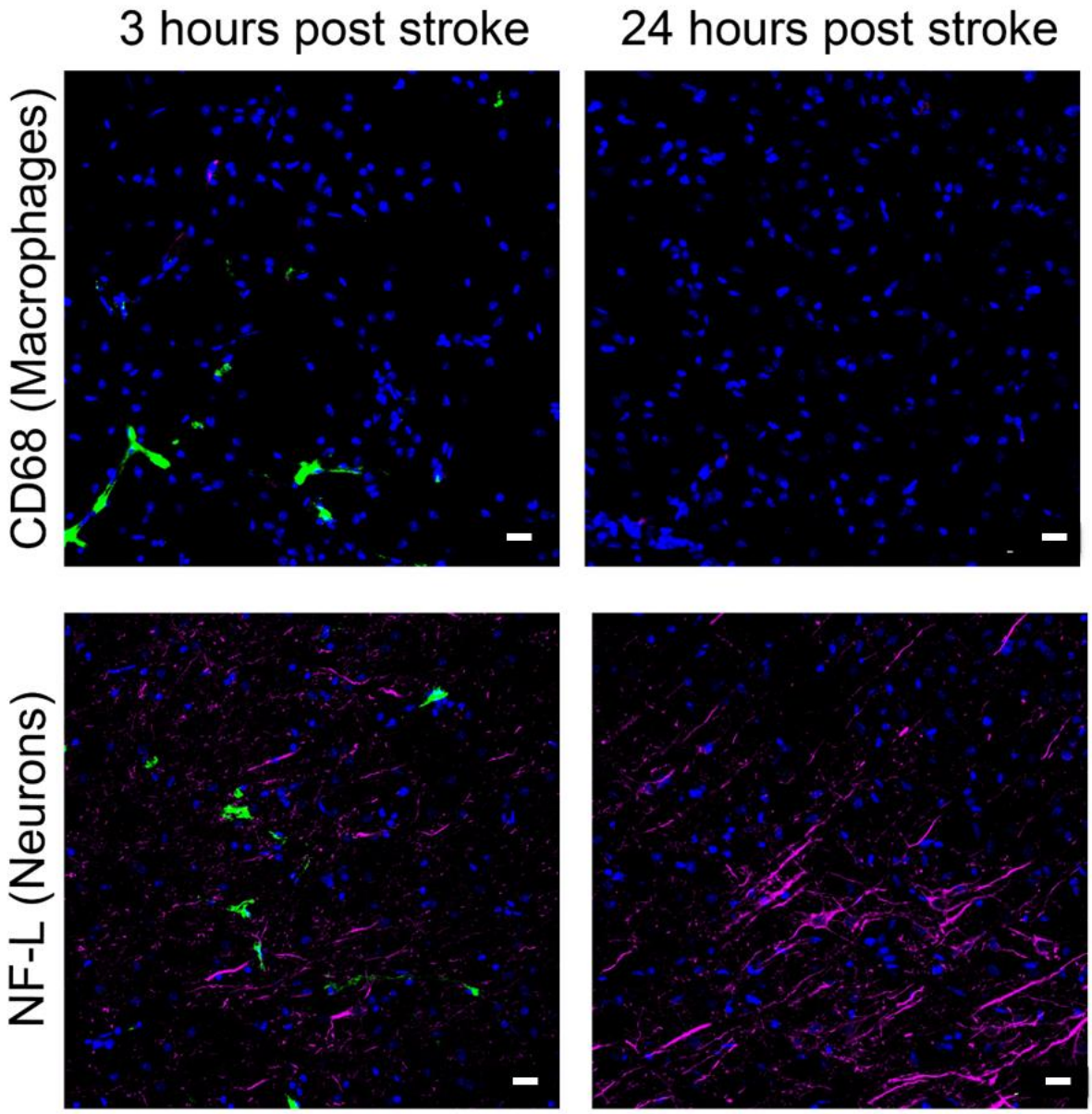

Figure 2.2 *Cl*-nanozyme in the brain does not co-localize with neuron or activated macrophages.

Immunofluorescent labelling reveals presence of *cl*-nanozyme 3h, but not 24h after reperfusion onset in the ischemic brain hemisphere. Distribution of *cl*-nanozyme in the brain is in branched clusters. The signal does not co-localize with mononuclear phagocyte marker CD68 or neuronal marker NF-L (both in pink) after stroke. Scale bar represents 20 μm.

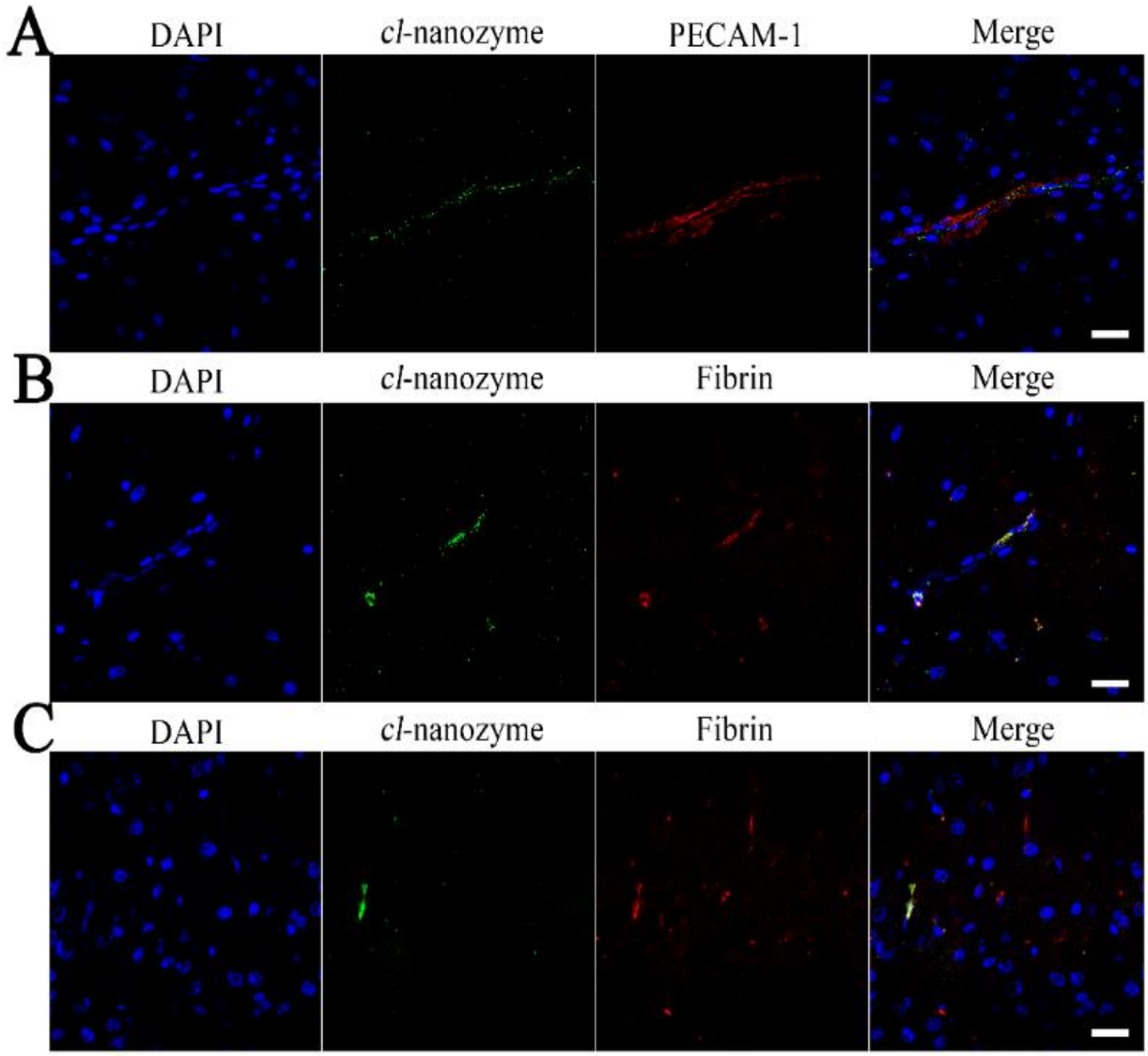

Figure 2.3 Distribution of *cl*-nanozyme in the Rat Brain.

Distribution of *cl*-nanozyme in the ipsilateral hemisphere of rat brains after I/R injury determined by immunofluorescence. **A.** *Cl*-nanozyme (PEG, green) was detected primarily in association with micro vessels (PECAM-1, red). **B.** Most *cl*-nanozyme signal co-localized with fibrin in rat brains after stroke, indicating possible interactions between *cl*-nanozyme and thrombus components. **C.** Not all fibrin signal in the brain were co-localized with *cl*-nanozyme. Nuclei are counterstained with DAPI, scale bars represent 20 μm.

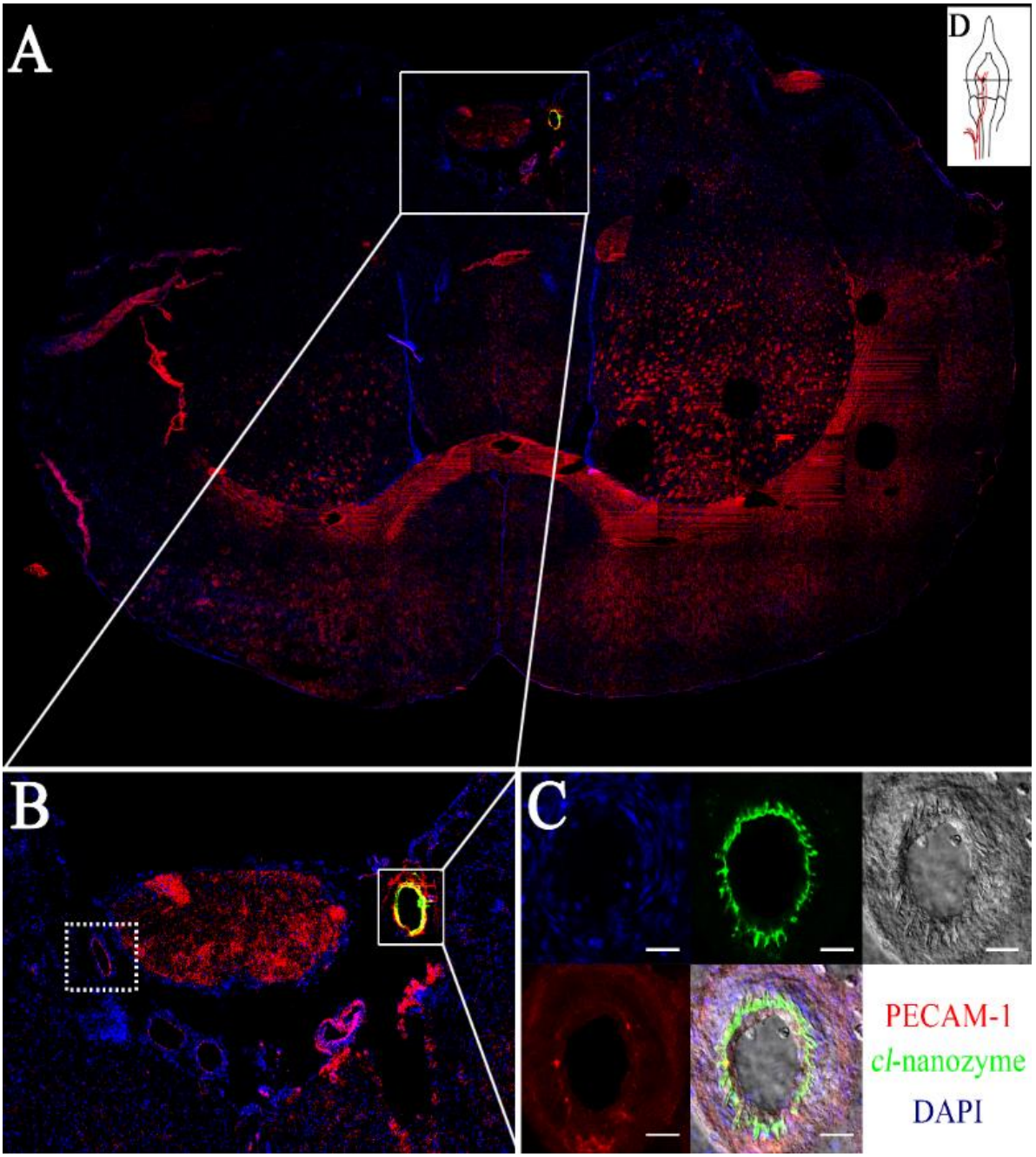

Figure 2.4 *Cl*-nanozyme Accumulation in the Damaged Internal Carotid Artery (ICA).

The ICA in the ipsilateral hemisphere in the rat brain showed intense staining for *cl*-nanozyme, which was not observed in the contralateral hemisphere. **A.** The ICA in the ipsilateral hemisphere was the only artery that showed very strong *cl*-nanozyme staining in the whole brain; **B.** 2.5X magnification of the squared area in **A**. Sub-arachnoid region shows that this staining was present only in the ipsilateral hemisphere, but not in the contralateral hemisphere; **C.** Confocal image of this artery shows *cl*-nanozyme co-localization with the injured endothelium cells lining the internal surface of this artery. Scale bars represent 20 μm. **D.** A graphic illustration of the position of the brain section shown in **A**.

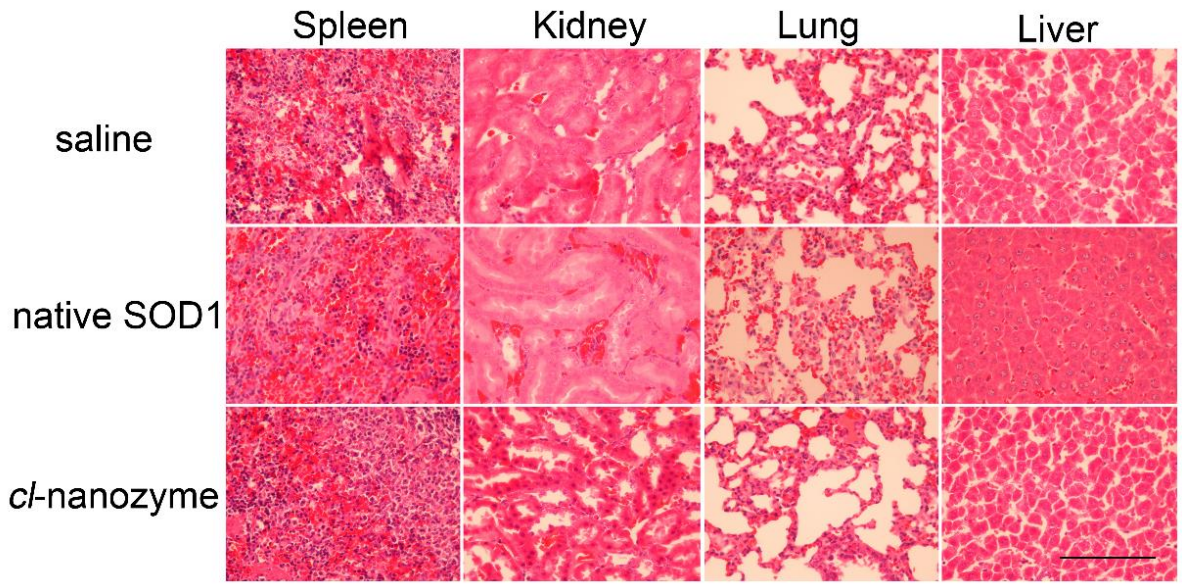

Figure 2.5 H&E staining of peripheral organs of MCAO rats.

Transient ischemic stroke was modeled in rats by MCA occlusion for 1 h followed by 24 h of reperfusion. Treatment was administered IV via the tail vein at the onset of reperfusion. Sections were harvested at the end of reperfusion period and examined by bright field microscopy at 40X magnification. Representative images for each treatment group are shown. Scale bar represents 50 μm.

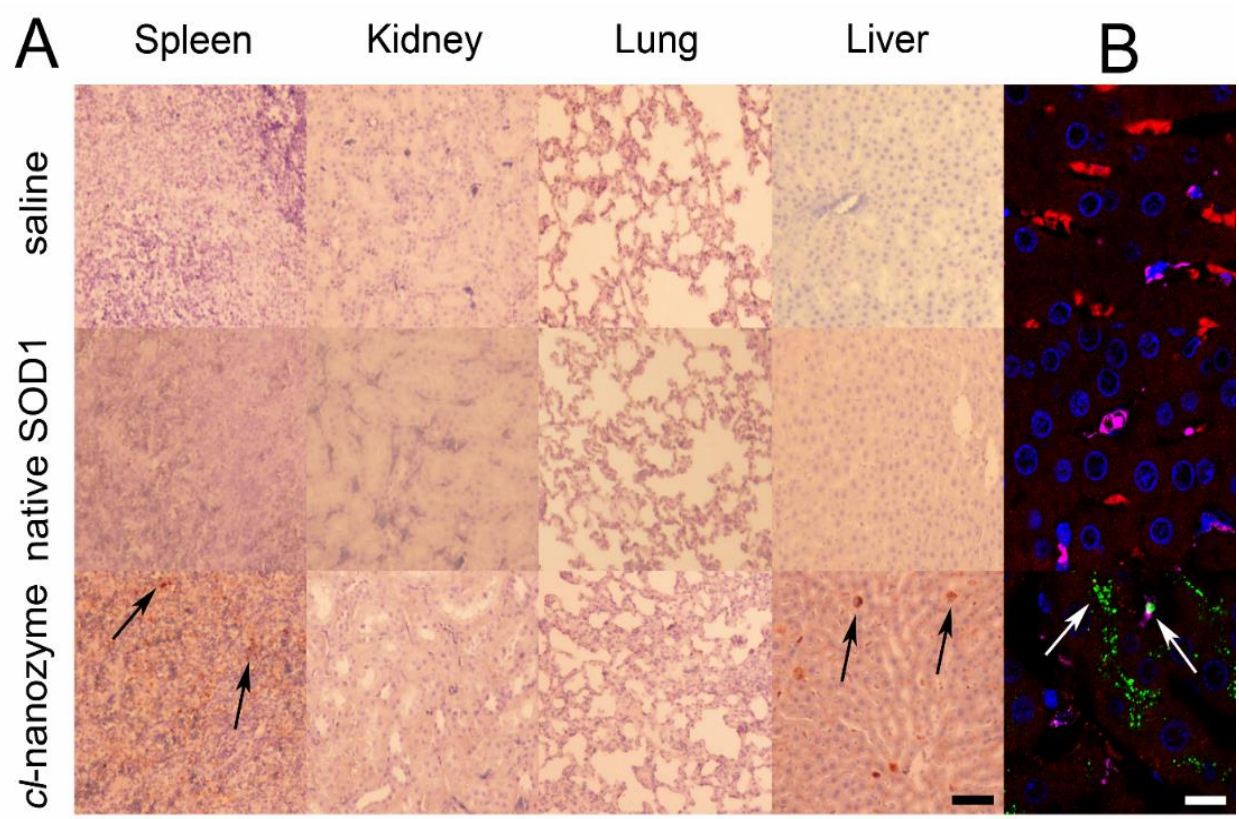

Figure 2.6 Distribution of *cl*-nanozyme in Rat Peripheral Organs.

Representative bright field micrographs of tissue sections harvested from MCAO rats 24 h after reperfusion. DAB was used to visualize *cl*-nanozyme in the tissue sections (black arrows). Scale bar represents 50 μm. **B.** Representative confocal fluorescent micrograph of liver tissue sections harvested from stroke rats 24 h after reperfusion and *cl*-nanozyme administration. Fluorescent immunohistochemistry demonstrated *cl*-nanozyme micro-distribution within the liver: red – hepatocytes; pink - Kupffer cells; green – *cl*-nanozyme; blue – nuclei. Scale bar represents 10 μm. Treatment groups are the same as shown in **A**.

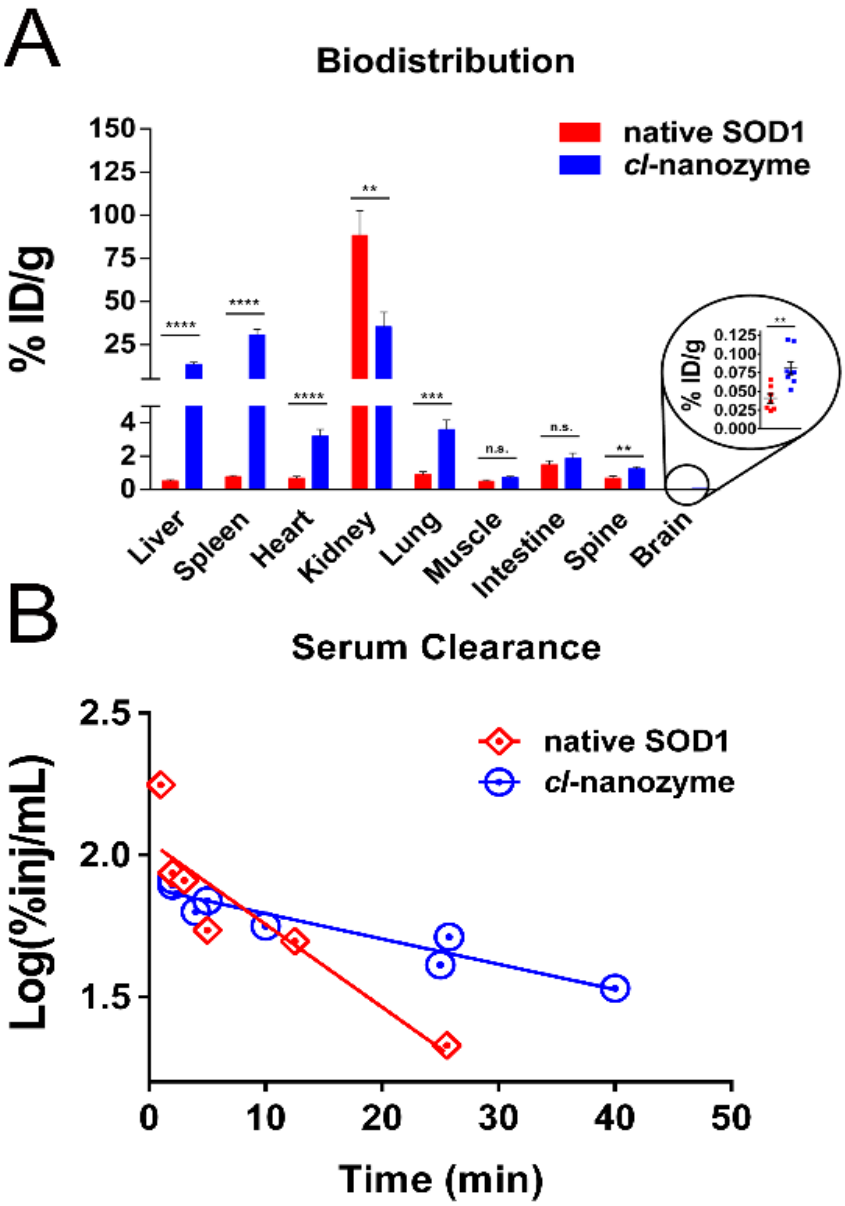

Figure 2.7 Biodistribution and Serum Clearance of Native SOD1 and *cl*-nanozyme in healthy mice.

A. C57BL/6 mice received IV bolus injection of either ^{125}I-labeled native SOD1 (n=7), or *cl*-nanozyme (n=8). One hour later organs were harvested and radioactivity was measured. Results represent mean % of injected dose per gram of tissue (ID%/g) with error bars representing ±SEM. Statistical significance was determined by Student's t-test (indicated as follows: n.s., not significant; *, P<0.05; **, P<0.01; ***, P<0.001; ****, P<0.0001); **B.** Serum clearance profiles of native SOD1 and *cl*-nanozyme were plotted and analyzed by linear regression fitting. The serum half-life was 33.8 min (R^2=8966, P<0.0005; n=1-2 mice/time point) for *cl*-nanozyme, and 10.3 min (R^2=8156, P<0.05; n=1-2 mice/time point) for native SOD1.

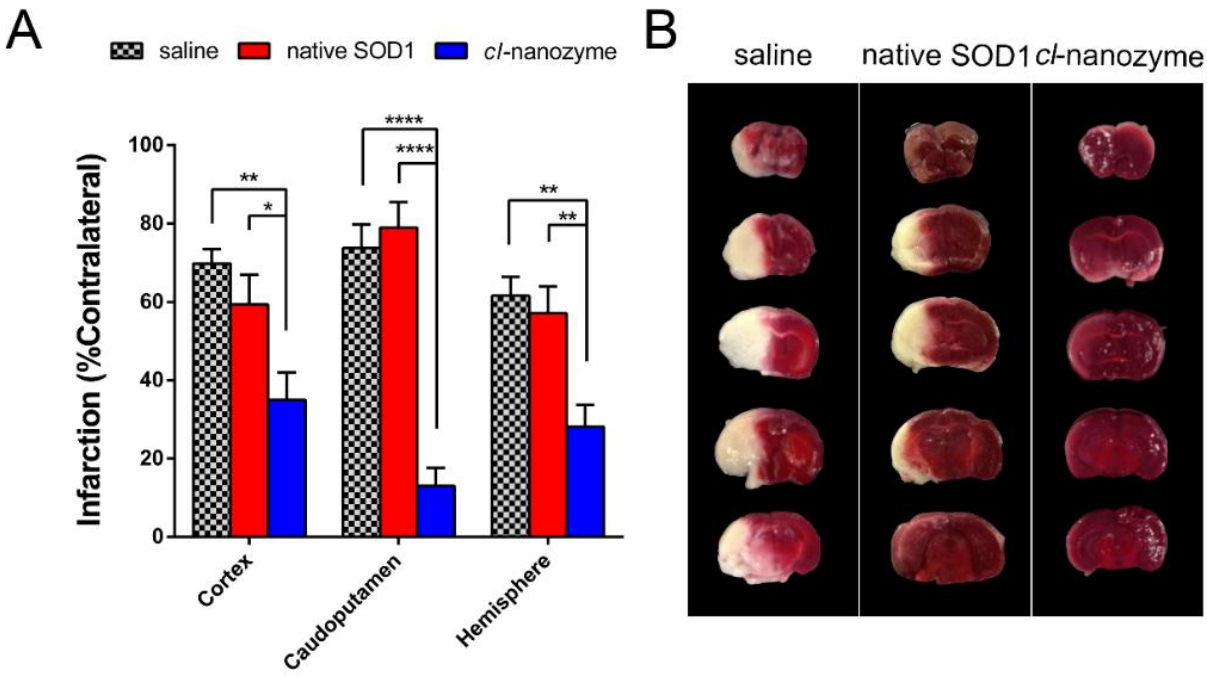

Figure 2.8 Therapeutic Efficacy of *cl*-nanozyme in Mice MCAO Model of I/R Injury.

At the onset of reperfusion, 10,000 U/kg of native SOD1 (n = 8), *cl*-nanozyme (n = 8), or equal volumes of saline (n = 7) were injected through the right jugular vein of the mice under anesthesia. Twenty-four hours after reperfusion, mice were euthanized and their brains were sectioned and stained using TTC solution. A. Bar graph showing infarct volume reduction. Infarction (% contralateral) was quantified as described in the methods section. Data were analyzed using one-way ANOVA with Tukey's post-hoc test and presented as mean ± SEM. Statistical significance is defined as $P<0.05$, and indicated by * ($P<0.05$), ** ($P<0.01$), or **** ($P<0.0001$). B. Representative coronal brain sections from animals receiving different treatments stained using TTC. Dark-colored areas indicate viable tissue; pale-colored areas indicate dead (infarcted) tissue.

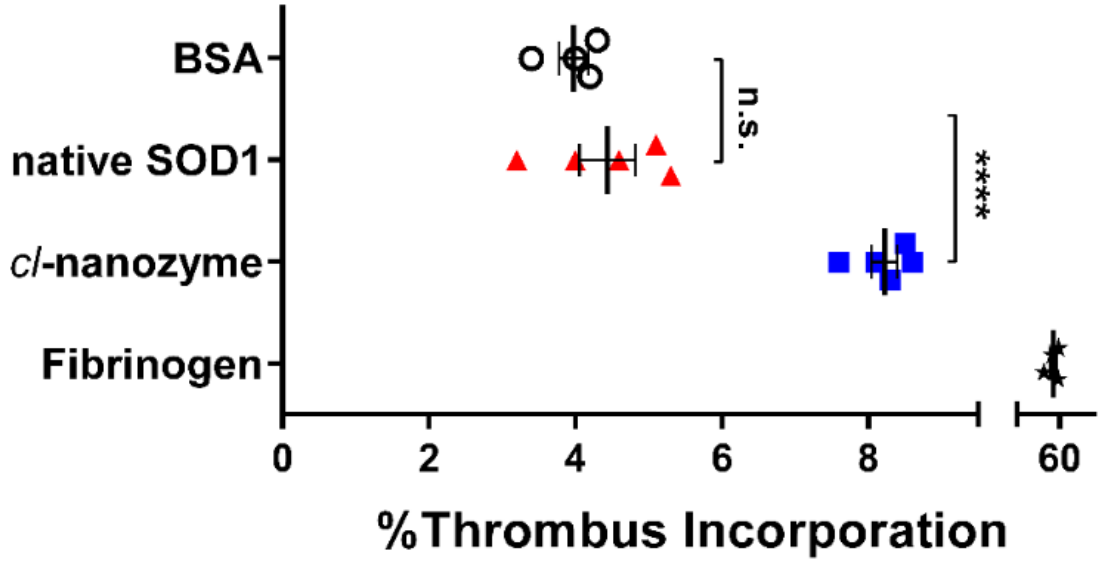

Figure 2.9 Thrombus Incorporation Assay in Mouse Plasma.

Native SOD1 and *cl*-nanozyme were labeled using ^{125}I before incubation with mouse plasma for 24 h at 4 ^{o}C. The plasma was then centrifuged to separate thrombus and serum. The percentage of radioactivity in the thrombus compartment was calculated as described in the methods section. BSA and fibrinogen were also labeled and used in parallel as negative and positive controls. Data were analyzed using unpaired Student's t-test and are presented as mean ± SEM (n=4 or 5). Statistical significance is defined as $P<0.05$, and indicated by n.s. (not significant) or **** ($P<0.0001$)

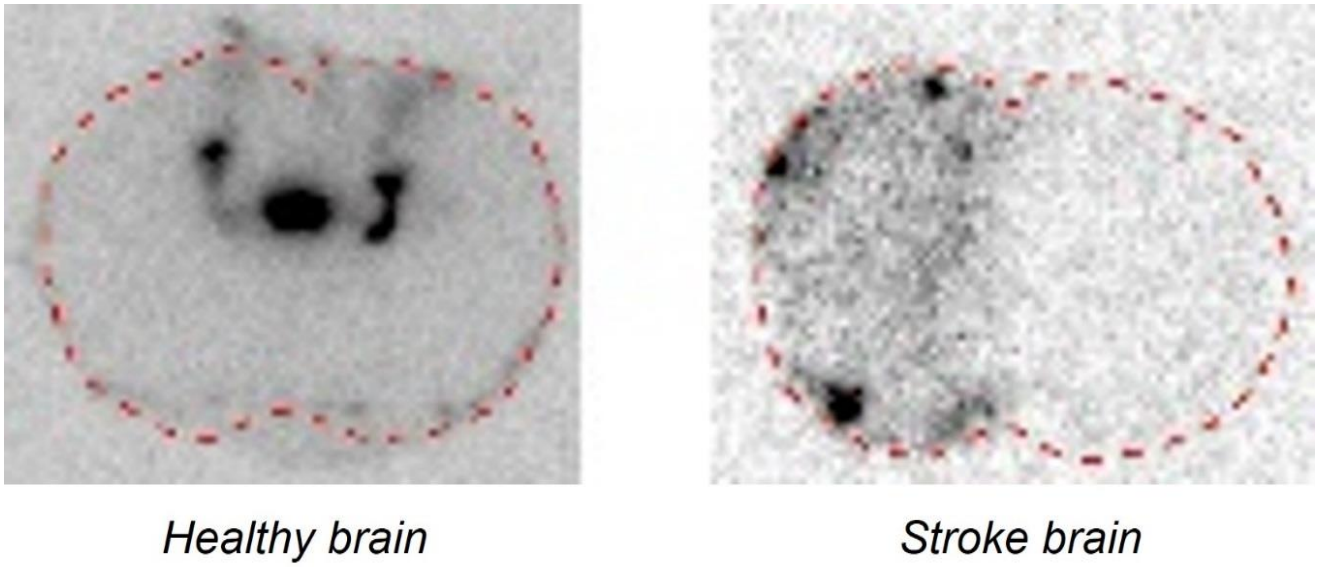

Figure 2.10 Autoradiography of brain slices after IV injection of ^{125}I labelled *cl*-nanozyme

^{125}I labelled *cl*-nanozyme was IV injected in mice with or without stroke. The mice were sacrificed and perfused with PBS 1 hour after injection. The mice brains were sectioned and subjected to autoradiography analysis.

CHAPTER 3 SOD1 NANOZYME WITH REDUCED TOXICITY AND MPS ACCUMULATION[3]

3.1 Summary

We previously developed a "cage"-like nano-formulation (nanozyme) for Copper/Zinc Superoxide Dismutase (SOD1) by polyion condensation with a conventional block copolymer poly(ethylene glycol)-b-poly(L-lysine) (PEG-PLL) followed by chemical cross-linking. Herein we report a new SOD1 nanozyme based on PEG-b-poly(aspartate diethyltriamine) (PEG-PAsp(DET), or PEG-DET for short) engineered for chronic dosing. This new nanozyme was spherical (Rg/Rh = 0.785), and hollow (60% water composition) nanoparticles with colloidal properties similar to PLL-based nanozyme. It was better tolerated by brain microvessel endothelial/neuronal cells, and accumulated less in the liver and spleen. This formulation reduced the infarct volumes by more than 50% in a mouse model of ischemic stroke. However, it was not effective at preventing neuromuscular junction denervation in a mutant $SOD1^{G93A}$ mouse model of Amyotrophic Lateral Sclerosis (ALS). To our knowledge, this work is the first report of using PEG-DET for protein delivery and a direct comparison between two cationic block copolymers demonstrating the effect of polymer structure in modulating the mononuclear phagocyte system (MPS) accumulation of polyion complexes.

3.2 Introduction

Reactive Oxygen Species (ROS) are actively involved in the pathophysiology of a variety of neurological disorders [162]. They cause oxidative damage to tissues by reacting

[3] Part of this chapter previously appeared as an article in the Journal of Controlled Release. The original citation is as follows: *Jiang, Yuhang et al., J Control Release. 2016 Jun 10;231:38-49. doi: 10.1016/j.jconrel.2016.02.038.*

with lipid, protein, and DNA molecules [163]. As a primary component of the anti-oxidative system in the body, SOD1 has been considered a promising therapeutic candidate for preventing oxidative damage [164]. However, the direct use of SOD1 for therapeutic purpose has been hampered by the poor stability and pharmacokinetics of this protein after intravenous (IV) injection [165] as well as low permeability across cellular membranes [108]. Several nano-formulations or chemical modification approaches have been proposed to protect SOD1 from proteolysis [113], reduce SOD1 renal clearance [116, 117, 166], increase SOD1 membrane permeability [167, 168], and target SOD1 to the site of disease [118]. In particular, the concept of "caging" SOD1 in semi-permeable nanoparticles has recently gained considerable attention [169-171]. In this approach the proteins are preserved inside a polymeric "cage" that enables unimpeded diffusion of ROS to SOD1 active site. Thereby, the encaged SOD1 is spontaneously available for catalyzing superoxide dismutation without the need for the release and exposure of the enzyme to proteinases or other components of the blood.

We have developed such "caged" SOD1 nanoparticles (SOD1 nanozymes) [32] using the enzyme self-assembly with PEG-PLL followed by chemical cross-linking of the copolymer with 3,3'-dithiobis(sulfosuccinimidyl propionate) (DTSSP). Recently we further demonstrated that PEG-PLL based nanozyme passively accumulates in the micro-thrombus and effectively reduces infarct volumes in rodent models of ischemic stroke [12]. The promising *in vivo* therapeutic efficacy of this formulation encouraged us to explore its potential to treat ALS, where ROS-related damage contributes substantially to its pathogenesis [172].

ALS is a chronic disease and its therapy requires long-term dosing regimens. From this standpoint, possible toxicity due to the relatively high cationic charge density of PLL used for SOD1 nanozyme synthesis may be a concern. Although no acute toxicity was observed with the PEG-PLL based nanozyme in our stroke study during a 24 hour time frame after a single IV bolus [12], we decided to forego using this formulation for a chronic dosing regimen.

Possible side effects of systemic administration of cationic nanoparticles include hemolysis and blood clotting [173]. Such nanoparticles are also well known to accumulate in organs of the MPS like the liver and spleen, thereby increasing MPS burdens and decreasing drug bioavailability to other organs [174]. To address this problem, we replaced PEG-PLL with another cationic block copolymer, PEG-DET to minimize potential toxicity during treatment. This block copolymer, originally developed for DNA delivery by Kataoka et al., as part of DNA polyplexes, has shown minimal toxicity during multiple chronic dosing regimens [175-179].

PEG-DET is a cationic diblock copolymer with diethyltriamine side chains, which can form polyion complexes with negatively charged nucleotides [89, 175, 180, 181]. In comparison to other existing transfection reagents (i.e. lipofectamine, polyethyleneimine, and cationic polymers), PEG-DET is less toxic and more effective at achieving long-term gene transfection [180, 182, 183]. As shown in **Figure 3.1** and **Figure 3.2**, PEG-DET has two pK_a values that induce stable complex formation with DNA ($pK_a = 9.9$) and a large buffering effect for efficient endosomal escape ($pK_a = 6.1$). We expect stable complex formation will protect SOD1 from enzymatic degradation in the bloodstream, while the buffering capacity of PEG-DET will reduce cationic polymer-mediated toxicity. Specifically, its cytotoxicity towards ALS-relevant cell lines (*in vitro*) and MPS organ accumulation (*in vivo*) were of utmost interest before moving to efficacy studies in ALS.

The first mouse model for ALS was developed after the identification of mutations in SOD1 gene in 1993 [184], and accordingly most of our knowledge of the etiology and pathogenesis of the disease comes from studies carried out using this animal model [185]. As one of the most deadly phenotypes in this model, the denervation of the neuromuscular junctions (NMJ) has been demonstrated to be highly associated with muscle-mitochondria-generated ROS [186], and occurred markedly prior to the onset of clinical symptoms [187]

Previous work in our laboratory has also shown that peripheral administration of recombinant heat shock protein 70 (rHsp70) in the $SOD1^{G93A}$ mouse delays symptom onset and increases lifespan [188-190] even though rhHsp70 was localized in the muscle instead of the spinal cord or brain [190]. Importantly, when administration began at postnatal day (P)30, rHsp70 promoted a significant increase in neuromuscular junction innervation at P75 [190].

In this study, we investigated whether peripheral administration of DET-based SOD1 nanozyme could scavenge muscle-mitochondria-generated ROS and consequently increase NMJ innervation. Towards this end, we characterized the physicochemical and biological properties of DET-based nanozyme including size, surface charge, cytotoxicity, biodistribution and pharmacokinetics, and further compared them with the PLL-based nanozyme in every aspect. The therapeutic activity of this new formulation was first tested in a mouse middle cerebral artery occlusion (MCAO) model of ischemic stroke to confirm *in vivo* efficacy before moving onto a transgenic mouse model ($SOD1^{G93A}$) of ALS. In the ALS experiment, the nanozyme was administered intraperitoneally (IP) with considerations on patient compliance from a translational perspective.

3.3 Materials and Methods

3.3.1 Chemicals.

3,3'-Diaminobenzidine (DAB), SOD1 (from bovine erythrocytes), 2,3,5-triphenyltetrazolium chloride (TTC), Triton® X-100, Tween-20, Dithiothreitol (DTT) and xylene were from Sigma-Aldrich (St. Louis, MO). PEG-PLL was purchased from Alamanda Polymers™ (Huntsville, AL). The PEG was 5 kDa, and the number of repeating units of PLL block was 51. PEG-DET was synthesized and characterized as described previously [28]. The PEG was 5 kDa, and the number of repeating units of the DET block was 49. Bovine serum albumin (BSA), 3,3´-dithiobis(sulfosuccinimidylpropionate) (DTSSP), ethanol, ethylene¬diamine¬tetraacetic acid (EDTA) disodium salt, 10% neutral buffered formalin,

trichloroacetic acid (TCA), and copper, zinc standard solutions were from Thermo Fisher Scientific (Rockford, IL). AlexaFluor® secondary antibodies, Dylight 594 carboxylic acid succinimidyl ester dye, Hoechst 43580, were from Life Technologies (Grand Island, NY).

3.3.2 SDS-PAGE and fluorescent labeling of SOD1 protein.

In the Sodium dodecyl sulfate polyacrylamide gel electrophoresis (SDS-PAGE) experiment, one group of samples containing 5 μg SOD1 were diluted with Laemmli loading buffer (Bio-Rad, Hercules, CA), and denatured by heating at 95 ^{o}C for 5 minutes (non-reducing condition). With another group of sample, 20 mM DTT was added into the loading buffer and incubated with the samples for 30 minutes at 37 ^{o}C before heating (reducing condition). Samples were then loaded on 4-20% polyacrylamide gels and electrophoresed at a constant voltage of 200V for 90 minutes. After electrophoresis, gels were stained using Bio-Safe Coomassie Stain solution (Bio-Rad, Hercules, CA) following manufacturer's protocol, and then imaged on a FluorChem™ E series imager (ProteinSimple, San Jose, CA) at 100ms exposure time.

Fluorescent labeling of native SOD1 was performed using maleimide chemistry targeting the free thiol groups on SOD1. Briefly, 1mg of maleimide conjugated Dylight 594 (Life technologies, Grand Island, NY) was dissolved in 100 μL of DMSO and added to 5 mg of native SOD1 dissolved in HEPES buffered saline (HBS), pH = 7.0. Reaction was performed overnight at 4 oC, followed by dialysis to remove the unreacted free dye. SDS-PAGE for dye-labeled samples were run in the dark, and imaged immediately with a FluorChemTM E series imager with a 590/50 nm filter to record the fluorescence signal. The same gel was then stained with Coomassie Blue to visualize protein bands.

3.3.3 Synthesis of PLL and DET-based nanozymes and their catalytic activity characterization.

PLL-based nanozyme and DET-based nanozyme were synthesized at the polycation to SOD1 charge (at pH=7.4) ratio $Z_{+/-}$ = 2 and 1, respectively. DTSSP was used as a cross-linker

at stoichiometric ratio to the amount of primary amine groups on the polycation, as described previously [16]. After synthesis and desalting (to remove unreacted DTSSP), nanozymes were purified to remove any unconjugated proteins and polymers. For the purification, nanozymes in 10 mM HEPES buffer (pH=7.4) containing 0.15 M NaCl were loaded onto Macrosep centrifugal devices (Pall Corporation, Port Washington, NY) and concentrated twice to about 10% of its initial volume by centrifugation at 4,500 rpm at 4°C. SOD1 enzyme activity was determined using a microplate version of pyrogallol assay [16], and normalized to protein content determined by inductively coupled plasma mass spectrometry (ICP-MS) using copper and zinc as standards.

3.3.3.1 Potentiometric titration.

PEG-DET (30 mg) was dissolved in 50 mL of 0.01 N HCl containing 150 mM NaCl, and titrated with 0.05 N NaOH containing 150 mM NaCl at 37 °C. The titrant was added in quantities of 50 μL after the confirmation that pH values were stabilized (minimal interval: 30 s). In a similar manner, titration experiments of PEG-PLL (30 mg) were completed. The relationship between pH and the protonation degree of polycations (α) was calculated from the obtained titration curves.

3.3.3.2 Dynamic light scattering (DLS).

Intensity-mean Z-averaged particle diameter (D_{eff}), polydispersity index (PDI), and surface charge (ζ-potential) were measured by using a Zetasizer Nano ZS (Malvern Instruments Ltd., MA). Data is presented as mean values ± standard deviation (SD) (n=3).

3.3.3.3 Size-exclusion chromatography coupled to a multi-angle light-scattering detector (SEC-MALS).

SEC-MALS was performed using a Fast Protein Liquid Chromatography system (FPLC, Agilent Technologies, CA). Sample was loaded on a Superdex 75 10/300 GL column (GE Healthcare, Rahway, NJ) to perform SEC and separate particles based on size. Phosphate-buffered saline (PBS) with sodium azide (NaN_3) (0.02% w/v), pH = 7.4 was used as eluent.

Scattered light was detected using an on-line connected multi-angle light-scattering DAWN HELEOS II detector (MALS with 18 angles) operating at a wavelength of 658 nm. The refractive-index increment (dn/dc) value was set at 0.185 mL/g assuming the nanozyme as a protein complex. Data acquisition and analysis were carried out using the Astra 6.1 software (Wyatt Technology Corporation, CA).

3.3.3.4 Atomic force microscopy (AFM).

Five μL of an aqueous dispersion of 0.01mg/mL DET-based nanozyme was deposited onto freshly cleaved mica (Ted Pella, CA) for 2 min, washed with water and air-dried overnight. AFM imaging was performed using a MFP3D system (Asylum Research, Santa Barbara, CA) operated in tapping mode. Particle sizes were quantified using ImageJ software (National Institute of Health (NIH), Bethesda, MD).

3.3.4 Cytotoxicity assay.

Cytotoxicity on immortalized human brain microvascular endothelial cells (hCMEC/D3) and immortalized mouse motor neuron cells (NSC-34) was determined using CellTiter 96® AQueous One Solution Cell Proliferation Assay (Promega, Madison, WI) according to manufacturer's instructions. Briefly, hCMEC/D3 and NSC-34 cells were seeded into different 96-well plates and cultured in 100 μL medium. When hCMEC/D3 cells reached 100%, and NSC-34 reached 70-80% confluency, serum-free media containing the SOD1 formulations (native, PLL and DET-based nanozymes) or free polymers (PEG-PLL and PEG-DET) at various concentrations were added to separate wells (n=4). After 24 h of incubation, the cells were washed and incubated in MTS assay reagent for 1 hour before absorbance at 490nm was measured using a SpectraMax® M5 microplate reader (Molecular Devices, CA). Percent (%) cell viability was calculated using the formula (Asample/Auntreated cells)×100%. Data represents mean ± standard error of the mean (SEM) (n=4).

3.3.5 Preparation of ^{125}I-labeled proteins and nanozymes.

Native SOD1, fibrinogen, BSA, or nanozymes was radioactively labeled with ^{125}I using chloramine-T method as previously described [38]. Briefly, 5 μg of protein or equivalent amount of nanozyme was mixed with 0.5 mCi Na^{125}I (PerkinElmer Life Sciences, Boston, MA) in a final volume of 40 μL in sodium phosphate buffer (0.25 M, pH=7.5). Five μL of freshly-made chloramine-T solution (2 μg/ μL in sodium phosphate buffer) was added to the mixture. After 1 min incubation, the ^{125}I-labeled samples were purified using Illustra NAP-5 desalting columns (GE Healthcare, Piscataway, NJ). Fractions were collected in Eppendorf tubes pretreated with 1% BSA in lactated Ringer's solution (1% BSA-LR) to prevent non-specific absorbance and radioactivity was measured in a PerkinElmer γ-counter. TCA precipitation was conducted to determine the ^{125}I association of labeled samples. Briefly, 1 μL of collected fractions was added to 0.5 mL of 1% BSA-LR and then precipitated in 0.5 mL of 30% TCA followed by centrifugation at 5000 xg for 10 min at 4 °C. The resulting supernatant and pellet were measured in a γ-counter and the values were used to calculate the % radioactivity that precipitated with acid (% protein bound-^{125}I = [CPMpellet/(CPMpellet + CPMsupernatant)]*100). Samples containing >100,000 CPM/μL of radioactivity and >90% precipitation from TCA were used for animal studies.

3.3.6 Animals.

Charles River Laboratories (Wilmington, MA) supplied 12-week old male C57BL/6 mice (20-28 g). Animals were housed and humanely handled in accordance with the Principles of Animal Care outlined by NIH. They were allowed free access to food and water and were maintained under temperature, humidity, and light-controlled conditions. Institutional Animal Care and Use Committees (IACUC) of the University of North Carolina at Chapel Hill and Wake Forest School of Medicine approved all experiments involving animal subjects.

3.3.7 Biodistribution and pharmacokinetics.

Twelve week-old male C57BL/6 mice were anesthetized with an intraperitoneal (IP) injection of 0.2 mL of urethane (4.0 g/ kg). Approximately 500,000 CPM of radiolabeled substances was injected IV via the jugular vein in a volume of 0.2 mL LR buffer containing 1% BSA.

For biodistribution study, the abdomen and rib cage were opened and venous blood was collected by cardiac puncture at one hour post-injection of radiolabeled substances. Next, 20 mL of 1x PBS was perfused through the left ventricle of the heart. Organs were dissected and wet-weighed. Levels of radioactivity were measured in a PerkinElmer γ-counter.

For pharmacokinetics study, multiple-time regression analysis was applied as previously described [191, 192] to calculate the blood-to-tissue unidirectional influx rates (K_i). Blood from the carotid artery was collected between 2 to 60 min after IV injection, the mice were immediately decapitated, and the whole brain removed and weighed. The arterial blood was centrifuged at 5400 x g for 10 min at 4ºC and the serum was collected. The levels of radioactivity in serum (50 µL) and brain samples were counted in a PerkinElmer γ-counter. The brain/serum ratios (µL/g) of radiolabeled substances in each gram of brain was calculated separately and were plotted against their respective exposure time. Exposure time was calculated from the following formula:

$$\frac{A_m}{Cp_t} = \frac{K_i \left[\int_0^t Cp(t)dt\right]}{Cp(t)} + V_i$$

where A_m is cpm/g of brain, Cp_t is cpm/µL of arterial serum at time t, and exposure time is measured by the term:

$$\frac{\int_0^t Cp(t)dt}{Cp(t)}$$

The linear portion of the relation between the brain/serum ratios versus Expt was used to calculate K_i (μl/g-min). The slope of the linearity measures K_i and is reported with its error term. To determine the rate of clearance of different SOD1 formulations from the serum, results were expressed as the percent of the injected dose (ID) in each milliliter of serum (%Inj/ml) and these values were plotted against time (min).

3.3.8 MCAO model of ischemic stroke in mice.

Experimental mice were randomly assigned before surgery into one of the following groups: DET-based nanozyme (n = 8), native SOD1 (n = 8), or saline (n = 7). The mice were weighed and subjected to 90 min ischemia under isoflurane anesthesia (5% v/v for induction and 1.5% v/v during surgery) as previously described [12]. Briefly, after midline ventral neck incision, unilateral MCAO was performed by inserting a silicone rubber coated monofilament into the right internal carotid artery 6 mm from the internal carotid/pterygopalatine artery bifurcation via an external carotid artery stump. Upon reperfusion, 10,000 U/ kg of native SOD1, DET-based nanozyme, or equal volumes of saline were injected through the right jugular vein of the mice under anesthesia.

3.3.9 TTC staining and brain infarct volume quantification.

After 90 min of ischemia and 24 h of reperfusion, the mice were euthanized and the brains were chilled at -80 °C for 4 min to slightly harden the tissue. Five 2-mm-thick coronal sections were made from the olfactory bulb to the cerebellum and then stained with 1.5% TTC in PBS (pH=7.4). The sections in TTC solution were incubated in a water bath maintained at 37 °C for 30 min, then transferred to 10% phosphate-buffered formalin and incubated overnight at 4 °C before pictures were taken for analysis. The infarct volumes were calculated blinded to the treatment given, and in each of the five slices the infarct size was quantified using Image J software (NIH). In addition to total hemisphere, the infarct areas were determined separately for cortex and caudoputamen in each slice. Then the infarct areas on each slice were summed

up and multiplied by slice thickness to give infarct volumes. The infarct volumes were calculated by Swanson's method [129] to correct for edema, and processed as % contralateral hemisphere to avoid mis-measurements secondary to edema.

3.3.10 Thrombus incorporation assay.

As described previously [12], 100,000 CPM of ^{125}I labeled fibrinogen, BSA, native SOD1, and nanozymes were added into an Eppendorf tube containing 1 mL C57BL/6 mouse Lithium heparin-stabilized plasma (Innovative Research, MI). Half mg of protamine sulfate was then added to neutralize heparin and allow thrombus to form. The tube was incubated on a rotary-shaker for 24 h at 4 °C before centrifuging at 5000xg for 10 min. Serum was separated from the white thrombus at the bottom of the tube, and then subjected to TCA precipitation assay to correct for error caused by ^{125}I dissociation during incubation according to the above-mentioned method. Percentage of protein sequestered in the thrombus compartment were calculated using the following formula: %Thrombus incorporation = $[CPM_{thrombus} /(CPM_{thrombus} + CPM_{serum})]*100$.

3.3.11 Methods for treatment of SOD1^{G93A} mice.

All animal experiments conformed to National Institutes of Health guidelines and were approved by the Wake Forest University Animal Care and Use Committee. Wild type females and SOD1^{G93A} males [B6SJL-TgN (SOD1-G93A) 1Gur], obtained from The Jackson Laboratory (Bar Harbor, ME), were bred to generate SOD1^{G93A} mice. Genotyping was performed with standard primers against mutant SOD1 [32, 42] Animals were injected intraperitoneally with 100ul of saline, native enzyme or DET-based nanozyme (5, 15 or 25 kU/kg) three times a week starting at P28-P32, and sacrificed at P75 to determine neuromuscular junction (NMJ) innervation as described below.

3.3.12 NMJ innervation.

For counting innervated hind limb skeletal muscle NMJs, immunohistochemistry was performed on soleus and TA muscles. Animals were deeply anesthetized and transcardially perfused with 2% paraformaldehyde in 0.1 M sodium phosphate buffer. The muscles were dissected, rinsed twice with PBS and placed in 20% sucrose for at least 72 hours at 4oC. The muscles were embedded in 20% sucrose:OCT (2:1), cut at 30μm on the cryostat., and the sections were stained for the vesicular acetylcholine transporter (VAChT; Santa Cruz Biotechnology, Santa Cruz, CA) and neurofilament light chain (NF-L; Santa Cruz Biotechnology, Santa Cruz, CA). Alexa-fluor 488 secondary antibodies were used for detection (green). Sections were also labeled with Alexa-fluor- alpha-bungarotoxin (α-BTX; Invitrogen, Eugene, OR; red) [43]. NMJs that exhibited an overlap of red and green were considered innervated, while those that exhibited only α-BTX expression were considered denervated. The percentage of innervated NMJs was determined by counting at least 600 NMJs in each treatment group using previously established counting criteria [36].

3.3.13 Western blots.

To determine that nanozyme administered via intraperitoneal injection could be detected in muscle five microliters (5 kU/kg, 15 kU/kg or 25 kU/kg doses) were injected unilaterally into the tibialis anterior (TA). After one hour, animals were deeply anesthetized, decapitated and the TA was dissected and frozen in liquid nitrogen and stored at -80C. Additional SOD1 mice were treated intraperitoneally with 100ul of nanozyme (5 kU/kg, 15 kU/kg or 25 kU/kg doses) for five consecutive days, sacrificed and the TA was removed and frozen in liquid nitrogen. Protein isolation from the TAs was performed using RIPA buffer and sonication. 50 ug of protein from each sample were resolved on a 10% SDS-PAGE before transferring onto an Immobilon-FL PVDF membrane (IPFL00010 Millipore, Billerica MA). The membrane was then blocked in an Odyssey Blocking buffer (Li-Cor, Lincoln, NE) that

was diluted 1:1 with PBS, for one hour at RT followed by an overnight incubation at 4C with an anti-Polyethylene glycol antibody (PEG-B-47 ab 51257 Abcam, Cambridge MA). The membrane was washed in PBST the next day before being incubated with a Li-Cor IRDye 680RD secondary antibody (Li-Cor, Lincoln, NE) for one hour at RT. The membranes were washed in PBST and rinsed in PBS before being scanned on an Odyssey Infrared Imaging System (Li-Cor, Lincoln, NE), and quantified on ImageJ using densitometry analysis.

3.3.14 Statistical analysis.

Statistical analysis was done using Prism 5.0 software (GraphPad, CA). Statistical differences between treatment groups were determined using unpaired Student's t-test for groups of two and one-way ANOVA followed by Tukey's multiple comparison test for groups of three and above. A minimum P-value of 0.05 was estimated as the significance level. Results of all experiments are presented as mean ± (SEM) if not specified. The number of animals used in the ALS study was based on experimental requirements for analysis and were chosen for a two-sided analysis of population means with an acceptable probability of a Type I error (p-value) of 0.05 or less and a probability of a Type II error of 0.05 or less. Statistical significance occurred when power was determined to be 80% or better and the p value was equal to or less than 0.05. In all animal studies, experimenters were blinded to treatment groups until all results were obtained and statistical analysis completed.

3.4 Results

3.4.1 Analysis of nanozyme formation by SDS-PAGE.

Formation of DET-based nanozyme was confirmed by monitoring its migration pattern on a denatured polyacrylamide gel at different stages of the synthesis. SDS-PAGE for native SOD1 typically shows two bands representing monomer (16 kDa) and dimer (32 kDa, **Figure 3.1 B**, lane 1). By simply mixing the enzyme with PEG-DET copolymer, the dimer band disappeared while the monomer band became more intense (lane 2). After cross-linking of the

nanozyme with DTSSP, most staining was observed near the wells, which is consistent with formation of a larger and electrically neutral cross-linked nanozyme that is not disrupted by SDS [32, 63] (**Figure 3.1 B**, lane 3). In addition, SOD1 monomer band was diminished, and a new band appeared at a position slightly lower than the SOD1 dimer. This band could be either DTSSP crosslinked PEG-DET or a conjugate of SOD1 monomer and PEG-DET, or a mixture of both, since the molecular weight of SOD1 monomer (16 kDa) is very similar to that of PEG-DET (15 kDa). After purification, the relative intensity of both these bands decreased (**Figure 3.1 B**, lane 4). Under the reducing condition where all samples were incubated with 20mM DTT for 30 minutes at 37 ^{o}C before loading onto the gel, all samples were reduced to the SOD1 monomer state. Protein smears characteristic of PEG-SDS interactions [193] were observed in the cross-linked nanozyme samples (**Figure 3.1 B**, lanes 3 and 4), suggesting effective and complete reduction of nanozyme, which released polymer-protein conjugates as well as the native protein.

The above-described phenomenon of the disappearance of the SOD1 dimer band after mixing the enzyme with PEG-DET copolymer was intriguing (**Figure 3.1 B**, lane 2). Since the dimer was not observed in any of the samples at the reducing conditions, we hypothesized that in the case of the native SOD1 the cross-linked dimer was formed upon heating of the sample before electrophoresis due to oxidation and conjugation of the SOD1 free thiol groups. Indeed, bovine SOD1 is a homodimer stabilized by hydrophobic interactions, and the only free thiol group on the monomer happened to be located at the interface between the two monomers [194] (Cysteine 6, **Figure 3.1 D**). To examine the role of the thiol groups in the cross-linking of SOD1, we conjugated a fluorescent dye (Dylight 594) to native SOD1 cysteine via the maleimide chemistry to block the free thiol groups, and ran the samples on SDS-PAGE under non-reducing conditions. The conjugation was validated by the appearance of the fluorescent signal in the same location as the SOD1 monomer band (**Figure 3.1 C**, lane 6). After this

modification, the dimer band of native SOD1 again disappeared, which suggests that the thiol groups of SOD1 play a critical role in the formation of the cross-linked dimer. For some reason (e.g. steric hindrance or allosteric effects) such cross-linking did not take place when SOD1 was incorporated into the polyion complex with PEG-DET.

3.4.2 Characterization of DET-based nanozyme

We used several physicochemical techniques to analyze purified samples of DET-based nanozyme in aqueous dispersion. The DLS *Z*-average hydrodynamic radius (R_h), PDI, and ζ-potential of DET-based nanozyme are presented in **Table 3.1** in comparison with the parameters of the PLL-based nanozyme while the representative particle size distribution is shown in **Figure 3.3 A**.

These two nanozyme formulations appeared to be very similar in terms of their sizes and charge. The catalytic activity of these two nanozymes measured by pyrogallol assay was also very similar (45% vs. 51% of the activity of native SOD1). The further detailed analysis of the DET-based nanozyme was carried out by SEC-MALS. Using this method we determined the *Z*-average radius of gyration (R_g) and molar mass (M_w) of the nanozyme to be 13.0 (±8.0%) nm, and 2.8 x 10^6 (±0.4%) Da, respectively (**Figure 3.3 B**). The structure-sensitive parameter (R_g/R_h) has a value of 0.783, which is consistent with the theoretical value (0.775) for spherical particles [195]. The spherical morphology of DET-based nanozyme was further confirmed by AFM in the amplitude mode (**Figure 3.3 C**). DET-based nanozymes were well dispersed on the mica and displayed uniform size and spherical shape, consistent with the theoretical calculations from SEC-MALS data. The particle radius was plotted on a histogram (**Figure 3.3 D**), and the data approximately followed Gaussian distribution, with a mean of 13.6 nm, and a SD of 3.1 nm. This value is consistent with its R_g and R_h measurements from SEC-MALS and DLS.

3.4.3 Cytotoxicity of nanozyme

Cytotoxicities of nanozymes and polymers used for the nanozyme synthesis were evaluated in 2 different cell lines by MTS assay after 24 h of incubation (**Figure 3.4 A, B**). The hCMEC/D3 cell line is an immortalized human cerebral microvascular endothelial cell line that is commonly used to model the blood-brain barrier (BBB) *in vitro*. The NSC-34 cell line is a motor neuron-like cell line produced by fusion of a neuroblastoma cell line with mouse motor neuron-enriched primary spinal cord cells. DET-based nanozyme was well-tolerated by both cell lines with cell viabilities around 86 ± 1.6% (hCMEC/D3) and 78 ± 1.6% (NSC-34) even at SOD1 concentrations as high as 0.5 mg/mL. These values are very similar to those measured for native SOD1 alone (84 ± 2.6% in hCMEC/D3 cells, and 84 ± 1.9% in NSC-34 cells). In contrast, PLL-based nanozyme was more cytotoxic at the same concentration resulting in lower cell viabilities of 51 ± 2.6% (hCMEC/D3) and 51 ± 2.9% (NSC-34), respectively.

Similar results were observed when we compared the cytotoxicity of PEG-PLL and PEG-DET free polymers by incubating them at different concentrations in the absence of SOD1. More drastic differences in viability of both cell lines were observed after incubation with the two polymers (**Figure 3.4 C, D**). In the hCMEC/D3 cell line, PEG-DET had an IC_{50} value of 104.9 μM, and was about 3227% less toxic than PEG-PLL, whose IC_{50} value was 3.251 μM. In the NSC-34 cell line, both polymers were less tolerated than in the hCMEC/D3 cell line, with IC_{50} values of 14.68 μM (PEG-DET) and 2.027 μM (PEG-PLL), respectively.

3.4.4 Biodistribution and Pharmacokinetics

Biodistribution profile of the two nanozymes was compared in healthy C57BL/6 mice 1 hour after IV administration (**Figure 3.5 A**). As reported and extensively discussed in our previous work [12], PLL-based nanozyme formulation could significantly reduce kidney accumulation of native SOD1, and increase its uptake in almost all other organs, most notably liver (13.6% of ID) and spleen (30.7% of ID) due to its high cationic charge density. In the

current work, DET-based nanozyme showed remarkably lower uptake in these two organs (4.7% of ID in the liver, and 6.6% of ID in the spleen) compared to PLL-based nanozyme, although the uptake is still significantly higher than native SOD1.

In organs other than liver and spleen, no statistically significant difference in uptake was observed between the two formulations. In the serum clearance analysis, both nanozyme formulations demonstrated statistically significant linear relationships between log(%Inj/mL) and time, indicating first-order kinetics in their early phases of clearance (**Figure 3.5 B**). The serum half-life ($t_{1/2}$) for DET-based nanozyme was 28.4 min ($R^2 = 0.6804$, $P = 0.0136$), comparable but shorter than that of PLL-based nanozyme (33.8 min), and longer than native SOD1 (10.3 min).

In addition to the biodistribution study where the total drug amount was measured at a fixed time point after injection, we also performed multiple time linear regression analysis, which adopts a graphical approach and evaluates the unidirectional influx rate (K_i) into different organs over a period of time. This experiment was performed in selected organs of interest (liver, spleen, and kidney) during 1-70 min of exposure time after an IV bolus injection of ^{125}I-SOD1 samples (**Figure 3.5 C-E**). The unidirectional influx rates (K_i) were calculated as described in **section 3.3.7** , and summarized in **Table 3.2**. Not surprisingly, the K_i values of ^{125}I-labeled SOD1 nanozymes were highly consistent with their biodistribution pattern. Both nanozymes entered the kidney at an influx rate about 70% slower than that of native SOD1. PLL-nanozyme showed the fastest influx rates into the liver and spleen while DET-based nanozyme had much slower rates at only 23.2% and 20.6% (respectively) relative to PLL-based nanozymes. Native SOD1 was mainly sequestered in the kidney while almost negligible uptake was noted in the liver and spleen.

3.4.5 Infarct volume analysis in mouse MCAO model of ischemic stroke

In vivo therapeutic efficacy of DET-based nanozyme was tested in a well-established mouse MCAO model of ischemic stroke. The DET-based nanozyme treatment reduced the infarct size in this model of stroke. Specifically, in the nanozyme treatment group the volumes of infarct as determined by TTC staining in the three different brain regions analyzed (cortex: 32.0±6.9%; caudoputamen: 30.7±8.9%; hemisphere: 25.6±6.4%) were significantly smaller compared to those in animals injected with saline or native SOD1 (**Figure 3.6**). This protection effect is comparable to that previously reported by us using PLL-based nanozyme in the same animal model [12].

3.4.6 Treatment of the mutant SOD1^{G93A} mouse model of ALS

As reviewed in our recent paper, initial muscle denervation occurs in the TA muscle (fast fatigable and fatigue resistant fibers) between postnatal day (P) 14 and P30, while little denervation occurs in soleus muscle (slow and fatigue resistant fibers) even later in disease [196, 197]. In this study SOD1 mice were treated beginning at P30 to determine if the DET-based nanozyme could promote NMJ innervation. Two groups of animals were initially treated with 5 or 15 kU/kg native enzyme or nanozyme. No significant differences in NMJ innervation were detected in any treatment group (**Figure 3.7 C**; 15 kU/kg data not shown). Given the lack of positive effect, we next determined if the nanozyme reached muscle and therefore had access to the NMJ, muscles from treated animals (5, 15 or 25 kU/kg) were collected and western blot analysis performed to detect the DET-based nanozyme. Nanozyme was not detected in the TA muscles of animals treated at the 5 or 15 kU/kg doses (not shown); however, nanozyme was readily detected at the 25 kU/kg dose. When animals were treated with the 25 kU/kg dose, there was a slight increase in NMJ innervation in the native enzyme and nanozyme groups; however, this was not significantly different from the saline treated control group (**Figure 3.7 D**).

3.5 Discussion

In this paper we reported a new SOD1 nanozyme formulation based on a cationic copolymer PEG-DET, which had received considerable attention over the past decade as an excellent gene delivery carrier due to its low toxicity and high transfection efficiency. The preparation of this DET-based nanozyme was monitored and characterized first by SDS-PAGE experiment, where samples collected from different stages of preparation were analyzed by denaturing gel electrophoresis similar to our previous report on PLL-based nanozyme [32, 63], and the migration patterns were consistent between the two nanozyme formulations. Most of the crosslinked nanozymes were unable to migrate in the gel, consistent with the expected size increase and charge neutralization after formulation. Interestingly, when we loaded a simple physical mixture of SOD1 and PEG-DET on the gel (**Figure 3.1 B**, lane 2), the SOD1 dimer band at 32 kDa disappeared and the intensity of the monomer band increased notably.

Intrigued, we further investigated this phenomenon. Native SOD1 dimer is stabilized by 4 hydrogen bonds and extensive hydrophobic interactions at the interface between its two monomers [198]. Incubation with 1% SDS is enough to interrupt these interactions, and converts all the protein to its monomer form after native gel electrophoresis [199]. In our SDS-PAGE experiments, the SOD1 dimer was probably formed due to partial oxidation during heating the sample to 95 °C which led to disulfide bond formation between the free thiol groups of Cys 6 (**Figure 3.1 D**, the only free thiol group on the bovine SOD1 monomer [200]) residues on each monomer, because the dimer band completely disappeared in the DTT reduced samples. We proved this hypothesis by reacting the Cys 6 group with a maleimide-Dylight 594 fluorophore. After electrophoresis, the fluorescence was readily detectable on the 16 kDa monomer band after the thiol-maleimide conjugation reaction, and the dimer band again disappeared (**Figure 3.1 C**).

Our data indicates an interaction between PEG-DET and native SOD1 that inhibits the formation of disulfide bonds between free cysteine groups located in the hydrophobic interface of the monomers. This kind of disulfide bond formation has been reported to be involved in the oxidation pathways of SOD1 protein *in vitro* and *in vivo* [201-203], and blocking the free thiol group on SOD1 has been shown to confer nearly complete protection against peroxide induced oxidation [201]. Although non-cross-linked nanozyme is not an ideal formulation for SOD1 delivery due to its instability in *in vivo* conditions [32], its oxidation-inhibiting effect can be potentially utilized to develop a simple way for SOD1 storage without the need to chemically block its free thiol groups. To our knowledge, this work is the first report demonstrating inhibition of SOD1 oxidation through a non-covalent formulation approach.

The hydrodynamic size, ζ-potential, and SOD1 catalytic activity of DET-based nanozyme were very similar to PLL-based nanozyme (**Table 3.1**). Moreover, dynamic/static light scattering and atomic force microscopy data confirmed the shape of DET-based nanozyme to be spherical, again same as PLL-based nanozyme [32]. Structural density (ρ) of DET-based nanozyme can be calculated using the equation $\rho = 3M_w / (4\pi N_A R_g^3)$, where M_w denotes molar mass, N_A denotes the Avogadro constant, and R_g denotes the radius of gyration. Based on our data obtained from the SEC-MALS experiment, DET-based nanozyme had a structural density (ρ) value of 0.597g/mL, which is about 40% of the reported average density of compact proteins (1.47g/mL) [204]. This value is consistent with the "cage"-like hollow structure of the nanozyme formulation [32]. While it is reasonably compact after chemical cross-linking, there is still a large aqueous environment (~60%) inside the core, which is available for superoxide anions to freely access the SOD1 active sites and undergo dismutation, as well as for the reaction products (hydrogen peroxide and oxygen) to escape from them .

This structure allows the SOD1 activity to be immediately available without the need of being released, which is a major advantage compared to most other nano-formulations of

SOD1, and makes this formulation especially useful in scavenging acute ROS. Indeed, in a mouse MCAO model of ischemic stroke, DET-based nanozyme significantly reduced the brain infarct sizes by more than 50% (**Figure 3.6**), comparable to our previous reports on PLL-based nanozymes [12, 32].

The major advantage of DET-based nanozyme over PLL-based nanozyme involves the unique molecular structure of the DET repeating units which makes its toxicity much lower than PLL as described earlier. Consistent with theoretical speculations, PEG-DET appeared to be remarkably less toxic than PEG-PLL in both cell lines tested. The hCMEC/D3 cell line appeared to be more resistant to cationic toxicity than NSC-34 cells, which can be explained by the hierarchy of susceptibility to injures among brain cells (i.e. neurons are generally more vulnerable than endothelial cells) [205].

Interestingly, the dose-response curve for DET-based nanozyme was very similar to native SOD1, reflecting toxicity primarily caused by SOD1 overdose [206]. On the contrary, PLL-based nanozyme started to exert the same level of toxicity at lower doses, and was 2 to 3-fold more toxic than native SOD1 at the highest dose tested. Indeed, most primary amine groups on the polymers were cross-linked with stoichiometric DTSSP in both nanozyme formulations. However, considering the reaction efficiency and possible reaction between DTSSP and SOD1, DTSSP cannot conjugate 100% of the free amine groups on the polymers. Therefore, the cytotoxicity at high PLL-based nanozyme doses likely involved free lysine groups. The lack of cytotoxicity in DET-based nanozyme can be explained by the two-step protonation behavior of the free DET unit with a distinctive *gauche-anti* conformational transition, which can effectively reduce its charge density at physiological pH, and improve its cyto-compatibility [89]. This two-step protonation behavior of PEG-DET is further characterized by potentiometric titration (**Figure 3.2**). The protonation degree (α)/pH curve calculated from the titration curves indicates ~40% increase in α value through the pH drop

from 7.4 to 5.0. In contrast, PEG-PLL showed one step protonation with very little change in α value over all pH values below 9. Apparent pK_a values of PEG-DET were determined to be 9.9 (α =0.25) and 6.1 (α =0.75), respectively, consistent with previous reports on this polymer [89].

The distinct protonation behavior of the two polymers also resulted in remarkable differences in biodistribution and pharmacokinetics between DET and PLL-based nanozymes. Nanoparticles are well known for extensive accumulation in the liver and spleen after IV injection, primarily due to sequestration by the MPS [207]. This process is mediated by macrophages and phagocytic cells which can recognize opsonins (serum proteins) adsorbed onto nanoparticles [208]. In our study, the MPS accumulation (13.6% in the liver, and 30.7% in the spleen) of PLL-based nanozyme at 1h after injection appears to be very high for a PEGylated nanoparticle of its size (~40nm). Shah et al. reported PEGylated 30nm gold nanoparticles to have 30% accumulation in the liver and 60% accumulation in the spleen at 24 hours after IV injection. However, only 7% and 6% (respectively) were detected at the 1h time point [209], which is more consistent with DET-based nanozyme accumulation in the liver and spleen (4.7% and 6.6%). The rapid accumulation of PLL-based nanozyme into the MPS organs reflects the interaction between free ζ-lysine groups on PLL-based nanozyme with serum proteins, which has been shown in our previous work in a thrombus incorporation assay [12]. To further understand the difference, we also looked at the thrombus incorporation level of DET-based nanozyme (**Figure 3.8**). The fraction of DET-based nanozyme incorporated into the thrombus compartment was determined to be 5.9 ± 0.5%. This value is about 30% higher than those of BSA and native SOD1, but significantly lower than PLL-based nanozyme (8.2 ± 0.2%). This result is understandable considering the charge-shielding effect of free ethylenediamine groups on the PEG-DET polymer as we mentioned earlier. While free lysine groups in PLL-based nanozyme quickly activates opsonization and MPS sequestration,

the free ethylenediamine groups in DET-based nanozyme masks its charge by the *gauche* conformation and therefore effectively slowed down MPS sequestration.

Interestingly, the ability to be incorporated into thrombus happened to be an important feature for PLL based-nanozyme to passively target to injured blood vessels after stroke and exert therapeutic effects [12]. To see whether the DET-based nanozyme also displays the therapeutic potential in stroke, we tested this formulation in the same mouse MCAO model of ischemic stroke. To our surprise, the DET-based nanozyme formulation was almost as effective as PLL-based nanozyme in terms of infarct volume reduction. On the contrary, while native SOD1 also showed about 4% thrombus incorporation, it almost had no therapeutic effect as compared to saline. This result signifies the importance of formulation to protect the therapeutic protein. When native SOD1 was most likely deactivated after being chemically crosslinked into the thrombus, nanozyme formulations of SOD1 were able to remain active and rescued the injured blood vessels.

3.6 Conclusion

We have developed a new SOD1 nanozyme formulation by replacing PLL with the DET polymer in its composition. Compared to PLL-based nanozyme, the new formulation has similar morphology and colloidal properties, as well as anti-oxidant activity *in vitro* and *in vivo*. Moreover, this formulation proved to be significantly less toxic to endothelial cells and neurons, and accumulates less into the liver and spleen. While being effective in stroke, this formulation did not show significant prevention against NMJ denervation in the ALS model, suggesting the need for further engineering to better target the brain and spinal cord.

3.7 Future directions

With the exact cause and the progression pathways of ALS still not fully understood, the choice of protecting the peripheral vs. central nervous system appears to be especially complicated. The lack of therapeutic efficacy of DET-based nanozyme in the ALS model

countered our initial hypothesis, nevertheless these results offer an insight for further development of anti-oxidant based therapies for ALS management. We confirmed that the DET-based nanozyme achieved detectable levels in the tibialis anterior muscle, while the dose or dosing frequency was likely not optimized well enough for this therapy to be effective. Alternately, delivery of the nanozyme to the periphery (muscle, NMJ and axon) alone may not be sufficient to delay or prevent NMJ denervation that is a hallmark of the disease progression. Our biodistribution data indicate that the nanozyme does not achieve high concentrations in the brain (and presumably spinal cord) suggesting insufficient delivery across the BBB. As such, the nanozyme may not reach the motor neuron cell bodies or non-neuronal cells affected in ALS.

Could the administration route of nanozyme be a reason to explain its lack of efficacy in the ALS model? It is possible. In the introduction, we mentioned that the IP route was chosen with considerations on patient compliance from a translational perspective, as compared with IV administration. However, with this injection route we would expect to lose a considerable portion of the drug before it reaches the muscle tissues although we were able to detect their existence by western blot. If we performed direct intramuscular injection, we could be able to deliver a much higher dose to the muscle and see a better therapeutic response with that approach. Its down side would possibly be uneven distribution of nanozyme in the body, and the site of muscle tissue collection will need to be carefully selected and consistent throughout the study.

Future studies will test if delivery specifically to the central nervous system is effective in decreasing muscle denervation. This can be achieved by surface modification of the nanozyme formulation so that they can actively target to transporter or receptors on the BBB which can hopefully facilitate their trans-BBB delivery.

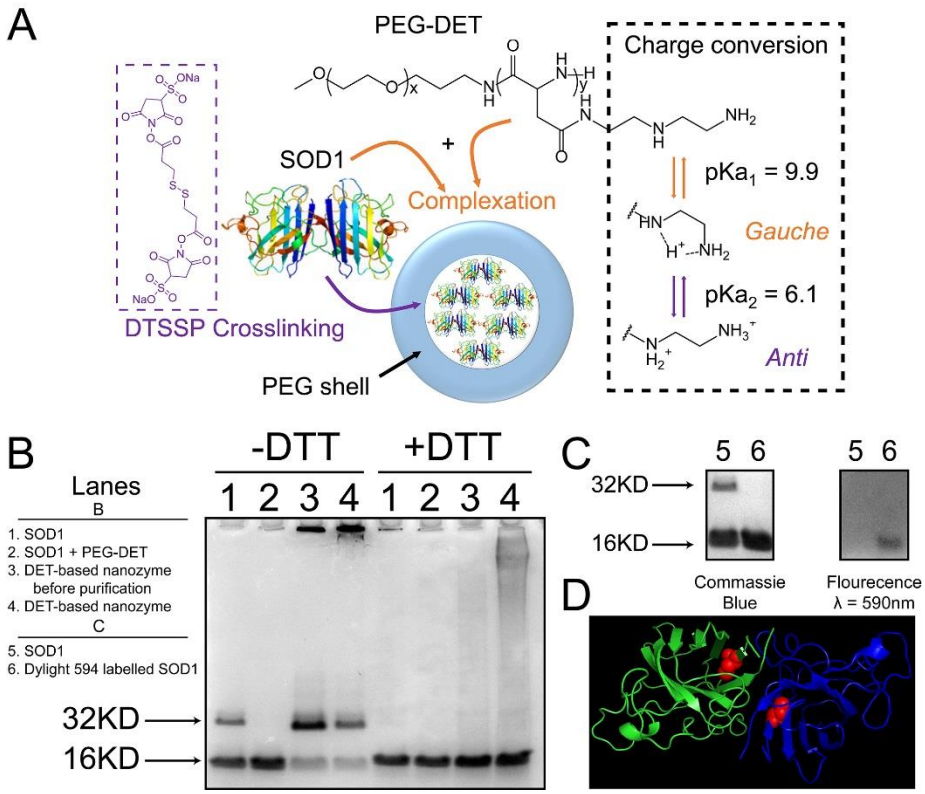

Figure 3.1 SDS-PAGE analysis of DET-based nanozyme.

A. Schematic representation of the synthesis of DET-based nanozyme (polyion complexation followed by chemical cross-linking using DTSSP) and the two-step protonation behavior of the DET polymer; B. DET-based nanozyme samples were collected at different stages of formulation (1. Native SOD1, 2. Physical mixture of SOD1 with PEG-DET copolymer, 3. Crosslinked non-purified DET-based nanozyme, 4. Purified DET-based nanozyme), and incubated with either Laemmli loading buffer (-DTT) or laemmli loading buffer with 20mM DTT (+DTT) before SDS-PAGE; C. The free thiol group on Cysteine 6 of SOD1 was reacted with Dylight 594 using the maleimide chemistry, and the samples before and after conjugation (5. Native SOD1, 6. SOD1 – Dylight 594 conjugation) was compared on a SDS-PAGE gel; D. Illustration of the position of Cysteine 6 on the bovine SOD1 molecule, drawn with the PyMOL software package (http://www.pymol.org/). The red balls represent Cysteine 6 and the blue and green loops each represents a SOD1 monomer.

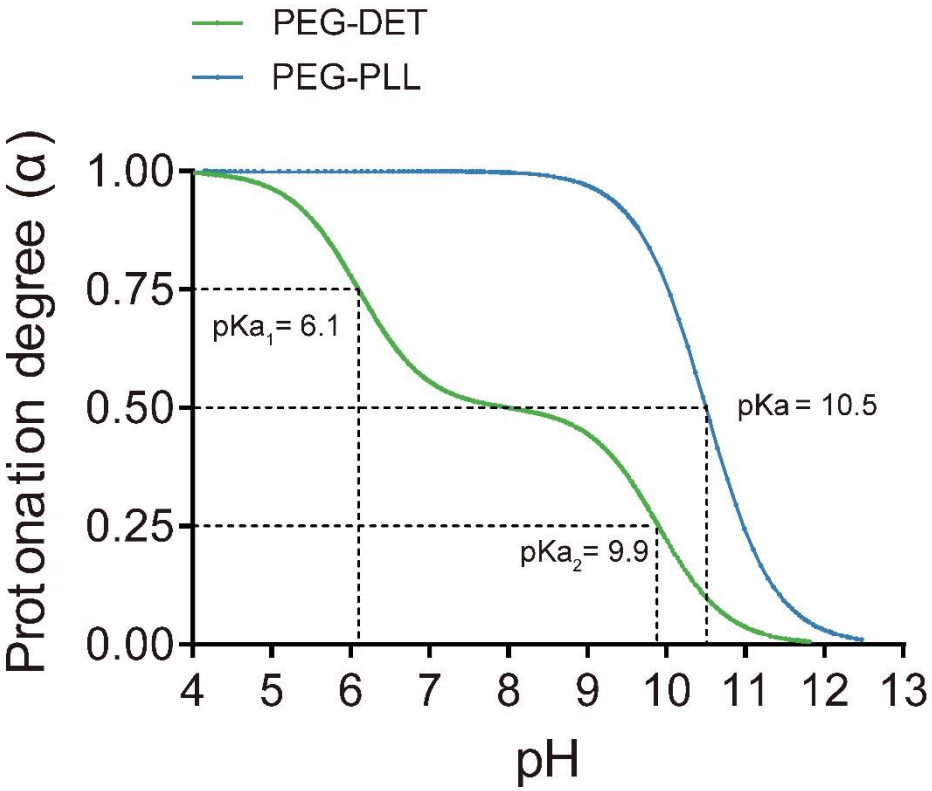

Figure 3.2 Protonation behavior of PEG-DET and PEG-PLL.

Change in protonation degree (α) with pH (α/pH curve) (150 mM NaCl, 37 ° C).

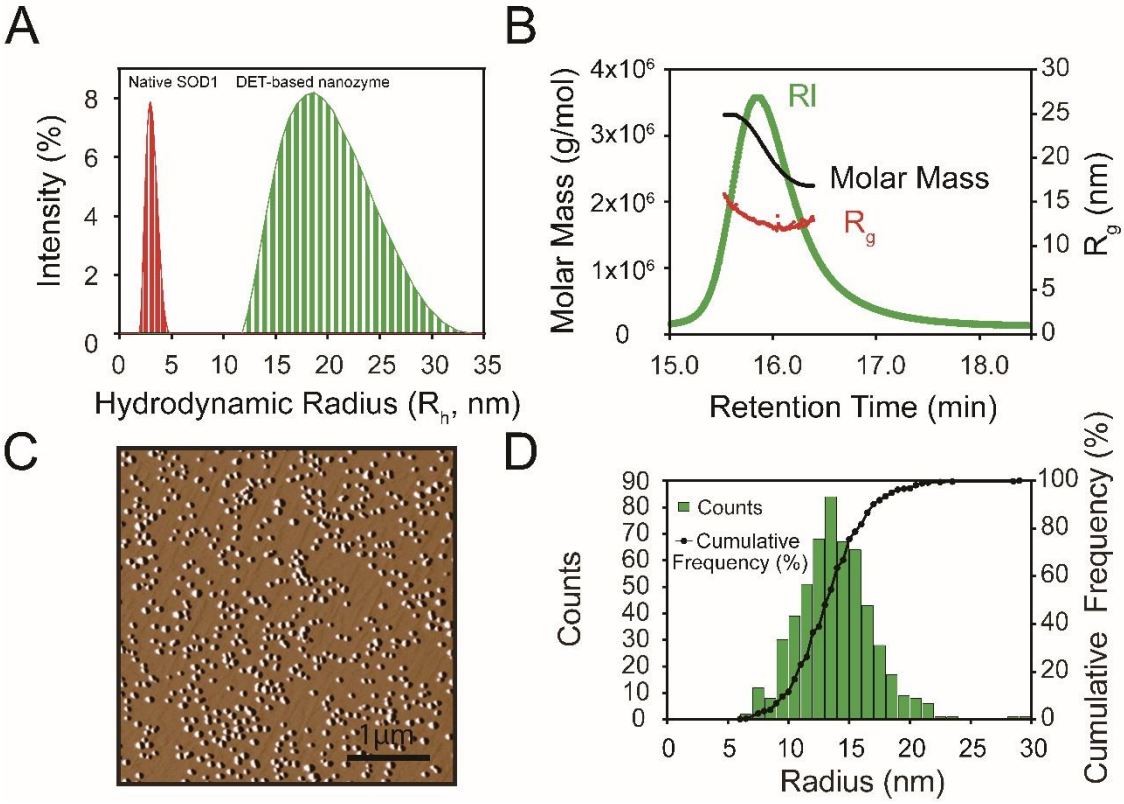

Figure 3.3 Characterization of DET-based nanozyme.

Crosslinked and purified nanozyme made from PEG-DET polymer and native SOD1 was characterized with a combination of different techniques. **A.** Representative graph of hydrodynamic size measurements for DET-based nanozyme and native SOD1 by DLS. The size distribution by intensity was plotted in the range of 0-70nm. **B.** A typical RI peak from SEC-MALS chromatogram of DET-based nanozyme together with the molar mass and radius of gyration (R_g) vs. retention time throughout the peak. **C.** AFM image of DET-based nanozyme in amplitude mode at ambient conditions. **D.** Histogram of DET size distribution (n = 540) as measured on the AFM image shown in **C**.

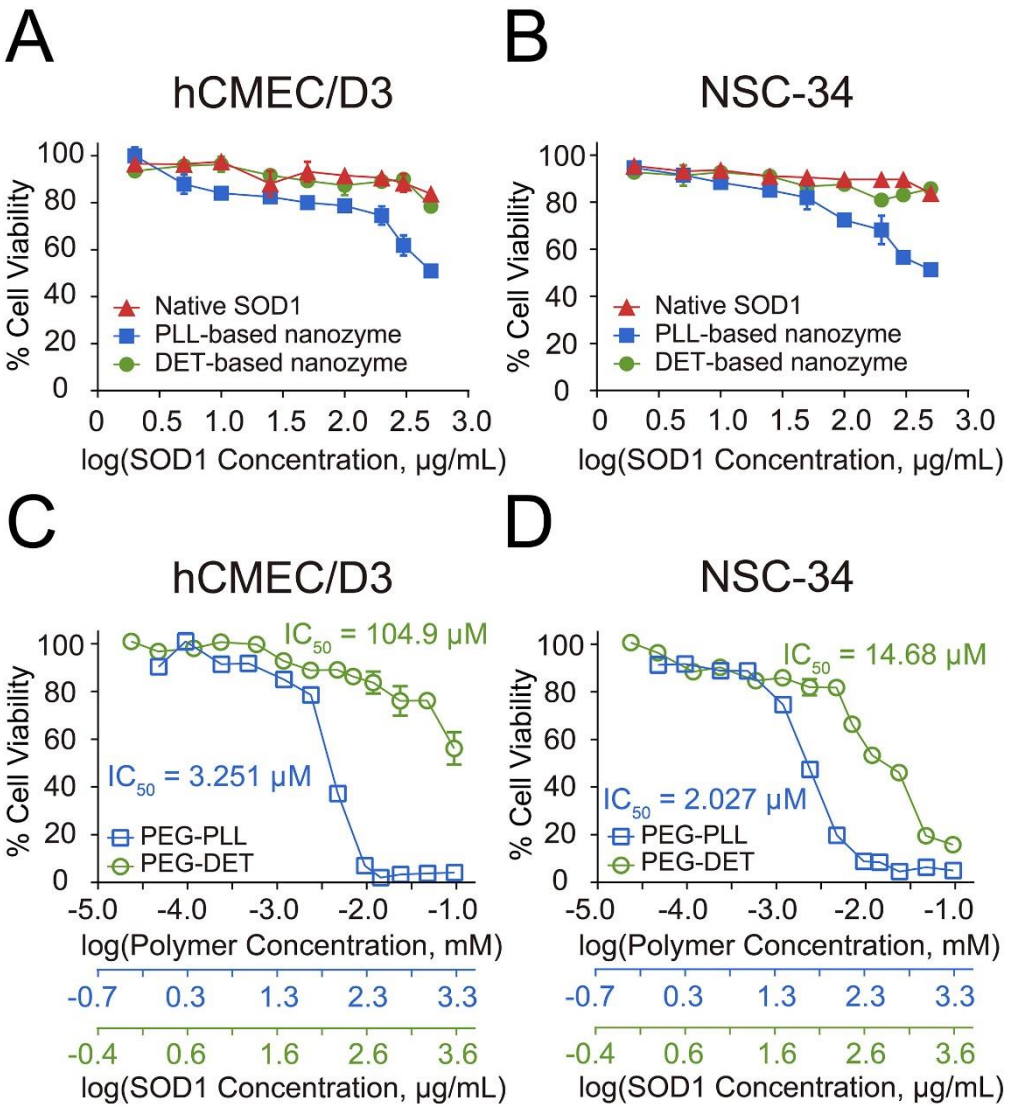

Figure 3.4 In vitro cytotoxicity to endothelial and neuronal cells after 24 h incubation.

Different concentrations of native SOD1, PLL-based nanozyme, DET-based nanozyme, PEG-DET, and PEG-PLL were diluted in serum-free cell culture medium, and added to cultured hCMEC/D3 (**A, C**) and NSC-34 (**B, D**) cells (n = 4, each). Twenty-four hours later, cell viability was assessed by MTS assay. Values are shown as mean ± SEM. (Some error bars are smaller than the symbol and thus not seen.) The extra color-coded X-axes underneath **C** and **D** represent the expected concentration of SOD1 when the respective amount of each polymer were used to synthesis SOD1 nanozymes.

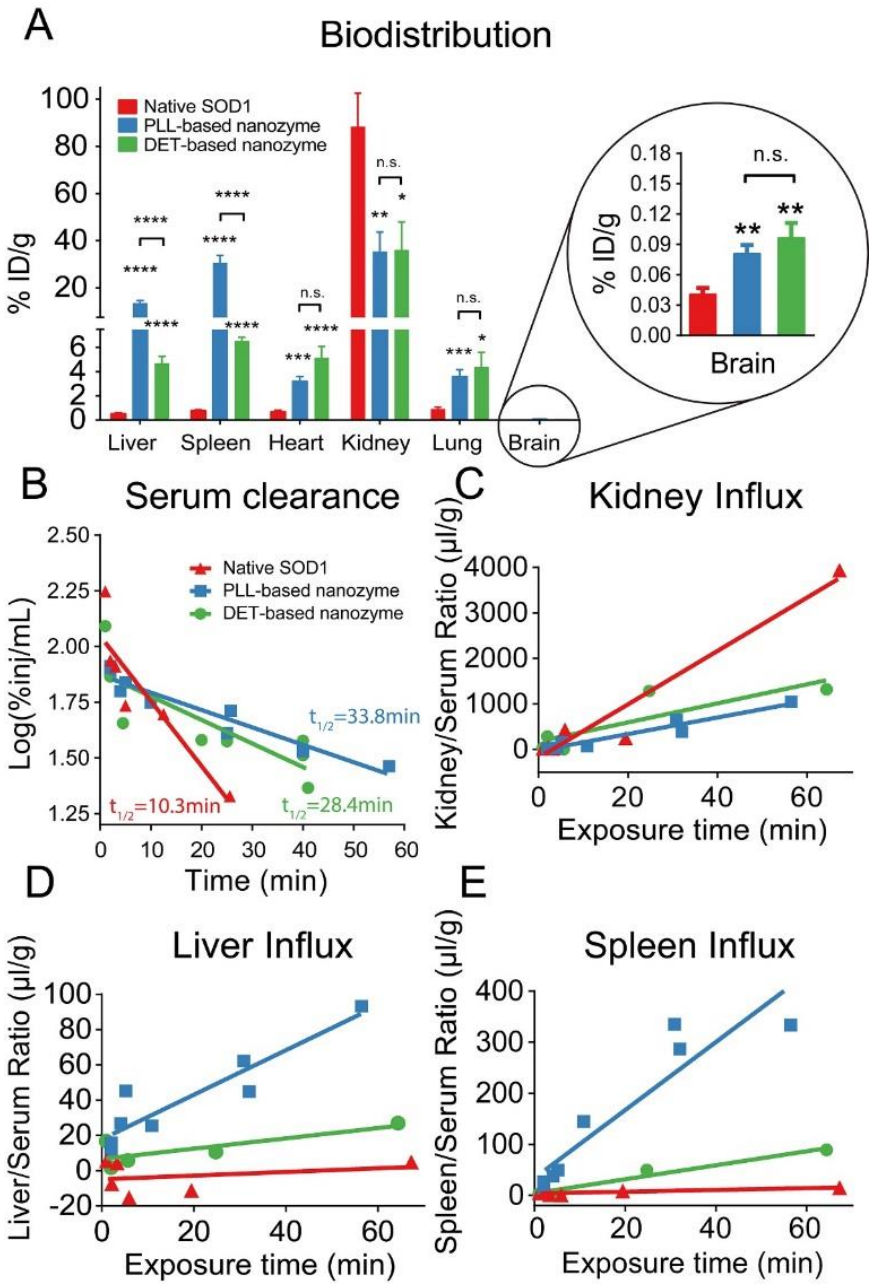

Figure 3.5 Polymer properties affecting biodistribution and influx rates of nanozyme.

A. Biodistribution of ^{125}I-labeled native SOD1 (n = 7), PLL-based nanozyme (n = 8), and DET-based nanozyme (n=8) 1h after IV administration in C57BL/6 mice. Symbols above nanozyme groups denote significance levels compared to the native SOD1 group. Results represent percentage of ID per gram of tissue (ID%/g). **B.** Serum clearance profiles of ^{125}I-SOD1 in different formulations after IV injection plotted and analyzed by linear regression fitting. DET-based nanozyme prolonged the circulation half-life ($t_{1/2}$) of native SOD1 from 10.3 min to 28.4 min, comparable to that of PLL-based nanozyme (33.8 min). **C-E.** Influx of ^{125}I-SOD1 into kidney, liver, and spleen over the exposure time of 1-70 min after IV injection. The influx rates confirmed the same patterns as we observed in the biodistribution experiment.

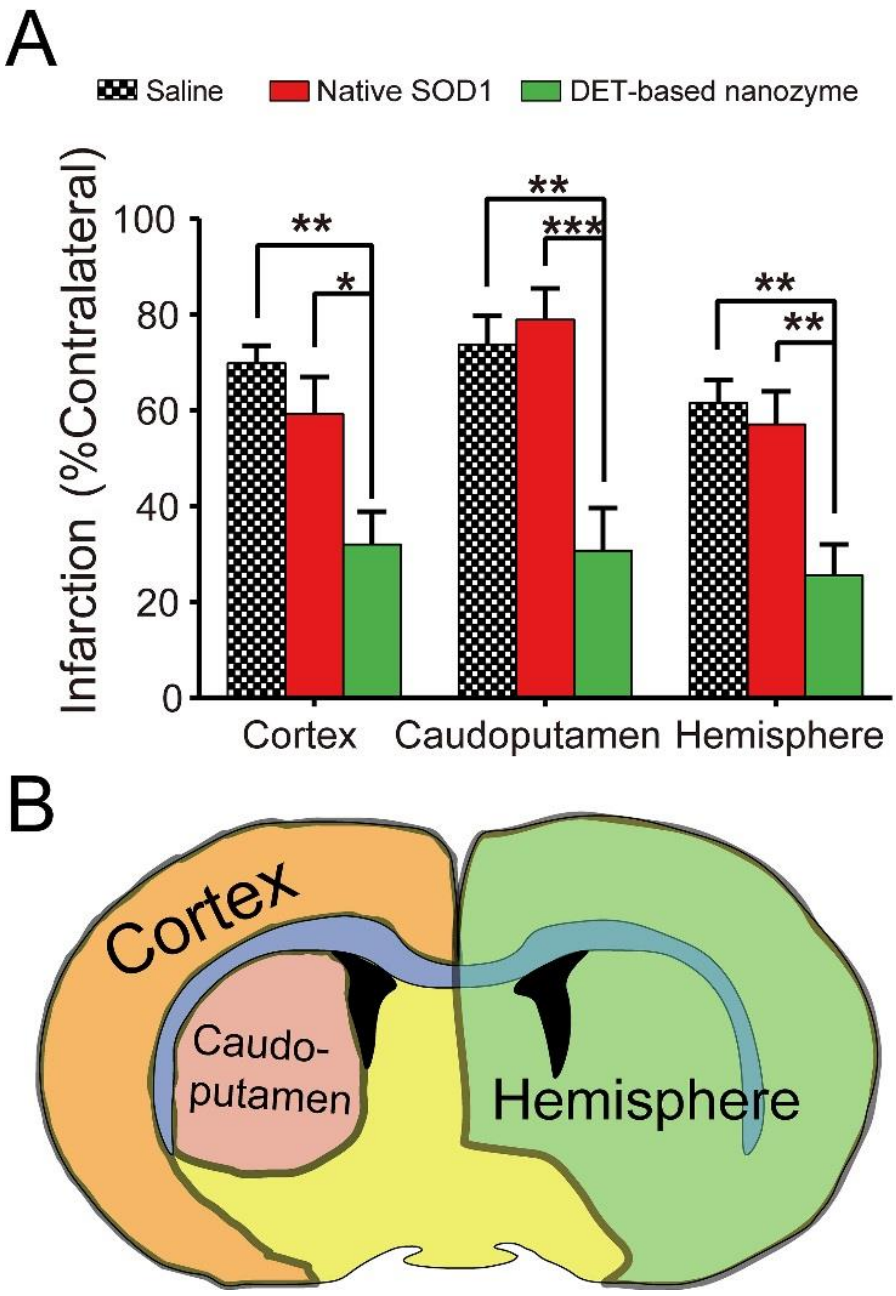

Figure 3.6 DET-based nanozyme reduced infarct volumes in the mouse MCAO model of ischemic stroke.

At the onset of reperfusion, 10,000 U/kg of native SOD1 (n = 8), DET-based nanozyme (n = 8), or equal volumes of saline (n = 7) was injected through the right jugular vein of the mice under anesthesia. Twenty-four hours after reperfusion, mice were euthanized and their brains were sectioned and stained using TTC solution. **A.** Bar graph showing infarct volume reduction. Infarction (% contralateral) was quantified as described in **section 3.3.9** . Data were analyzed using one-way ANOVA with Tukey's post-hoc test and presented as mean ± SEM. Statistical significance is defined as $P < 0.05$, and indicated by * ($P < 0.05$), ** ($P < 0.01$), or **** ($P < 0.0001$). **B.** Illustration of brain regions indicated in **A**.

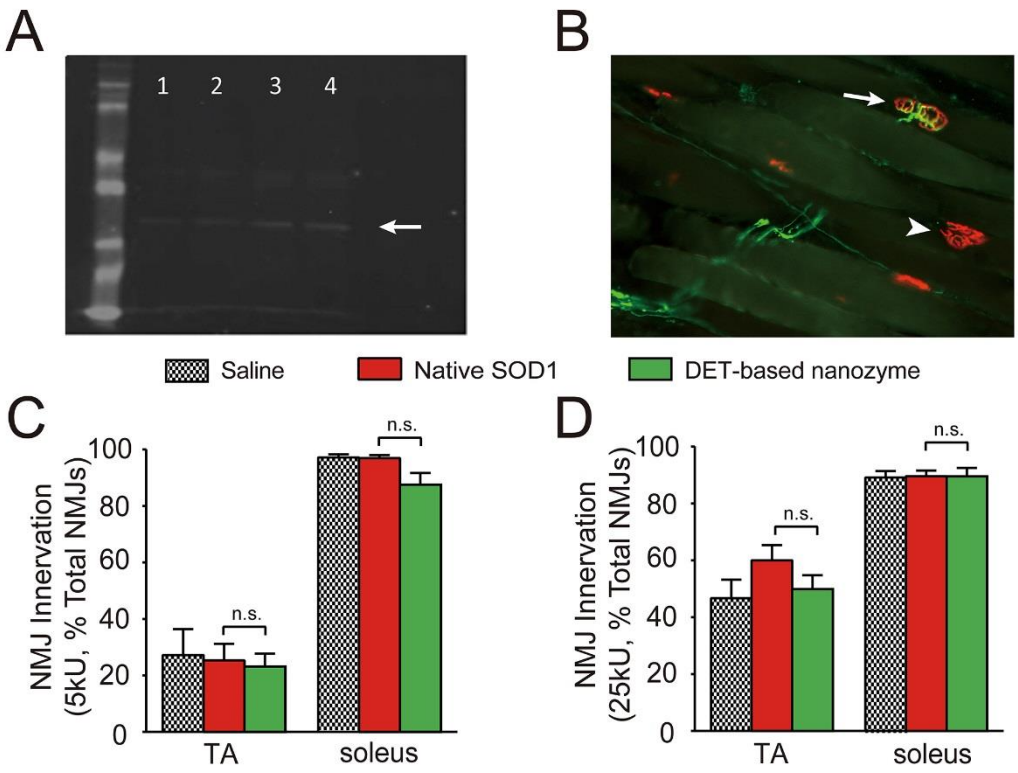

Figure 3.7 DET-based nanozyme was not effective against NMJ denervation in SOD1^{G93A} mice.

A. To determine if the nanozyme accumulated in muscle western blot analysis was performed to detect PEG. One wild-type (lane 1) and SOD1 (lane 2) mouse was intramuscularly injected with nanozyme (5ul) and TA collected after one hour. Additionally, two SOD1 mice (lanes 3, 4) were treated with 25 kU/kg nanozyme via intraperitoneal injection for 5 days and TA's collected after the 5th IP treatment. PEG-nanozyme was detected in TA of all mice treated with 25 kU/kg nanozyme either with intramuscular or IP injection. No PEG-labeled nanozyme was detected at the 5 or 15 kU/kg doses. **B.** Innervation of neuromuscular junctions (NMJs) was determined with immunohistochemistry where presynaptic terminals were identified with antibodies to vesicular acetylcholine transporter (VAChT) and axons identified with an antibody to neurofilament (NF). Both antibodies were detected with Alexa Fluor 488 conjugated secondary antibodies (green). Postsynaptic acetylcholine receptors were identified with Alexa Fluor 555 conjugated alpha-bungarotoxin (α-BTx; red). NMJs where no co-label for VAChT and only α-BTx were considered denervated (arrow head). Those NMJs with overlap, even if partial were counted as innervated (arrow). **C-D.** SOD1^{G93A} mice were treated at a SOD1 dose of either 5 kU/kg (n = 5-7) or 25kU/kg (n=13-16) via IP injection every other day starting on P30 through P75 and NMJ innervation were determined in the tibialis anterior (TA) and soleus muscles. There was no difference in the extent of NMJ innervation among the treatment groups in either tissue. Results are expressed as mean ± SEM.

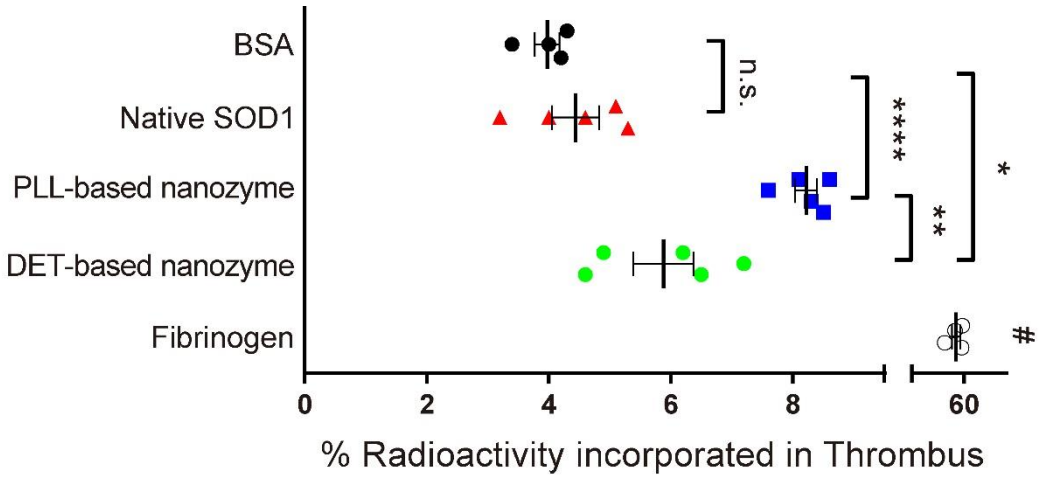

Figure 3.8 Thrombus incorporation in mouse plasma.

DET-based nanozyme showed higher level of thrombus incorporation than native SOD1, but lower than that of PLL-based nanozyme. Red, blue and green color represent native SOD1, PLL-based nanozyme, and DET-based nanozyme, respectively in all figures. Data were presented as mean ± SEM. Statistical significance was determined by unpaired Student's t-test (indicated as the following: n.s., not significant; *, $P < 0.05$; **, $P < 0.01$; ****, $P < 0.0001$, #, $P<0.0001$ compared with all other groups).

Table 3.1 Characterization of native SOD1 and different formulations of nanozymes.[a] [b]

Sample	R_h, (nm)	PDI	ζ-potential, (mV)	Enzyme activity, (% of initial)[c]
Native SOD1	2.8	0.60	-1.3	100
PLL-based nanozyme [32]	16.9	0.03	0.6	45
DET-based nanozyme	16.6	0.09	0.4	51

[a] Nanozymes were prepared at polycation to SOD1 protein charge ratio $Z_{+/-} = 2.$, chemically crosslinked and purified as described in **section 3.3.3** . R_h, PDI and ζ-potential were measured in 10 mM HEPES, pH=7.4. Catalytic activity of SOD1 was measured by pyrogallol autoxidation assay and normalized to Cu^{2+} and Zn^{2+} concentrations determined by ICP-MS.

[b] R_h, PDI, ζ-potential data are representative of > 5 independent experiments. Measurement error was typically < 10%.

[c] Enzyme activity data is representative of > 5 independent experiments. Measurement error was typically < 5%.

Table 3.2 Influx rates (Ki, µl/g-min) of different SOD1 formulations into brain, kidney, liver, and spleen during 1-70 min of exposure time after an IV bolus of ^{125}I-SOD1.

Formulation	Kidney	Liver	Spleen
Native SOD1	59±7.0	0.10±0.17	0.17±0.05
PLL-based nanozyme	18±2.0	1.3±0.2	6.7±1.1
DET-based nanozyme	21±7.7	0.29±0.13	1.4±0.2
F[a]	0.16	12	17
P[b]	0.70	0.0069	0.0025

[a] F denotes the results of F-tests assuming the null hypothesis that PLL-based nanozyme and the DET-based nanozyme have identical K_i values.

[b] P denotes the P-values associated with the F-values indicated on the row above.

CHAPTER 4 BLOCK IONOMER COMPLEX NANOFORMULATION STABLIZES BRAIN DERIVED NEUROTROPHIC FACTOR AND INCREASES ITS DELIVERY TO THE BRAIN AFTER INTRANASAL ADMINISTRATION[4]

4.1 Summary

Delivery of protein therapeutics to the brain has proven to be an intractable obstacle to effective treatments of neurological disorders. For example, brain derived neurotrophic factor (BDNF) has been identified as a possible therapeutic for a variety of neurological diseases. However, its delivery is hampered by poor serum stability and brain-to-blood efflux. Here, we report a simple block ionomer complex (BIC) formulation composed of a biocompatible polymer, poly(ethylene glycol)-*b*-poly(L-glutamic acid) (PEG-PLE), that hosts the BDNF molecule in a nanoscale complex, termed here Nano-BDNF. We show that Nano-BDNF forms as monodisperse, spherical particles with a core-shell structure. Molecular dynamics (MD) simulations suggest that binding between BDNF and PEG-PLE is mediated through electrostatic coupling as well as hydrogen bonding. The formation of BIC stabilizes BDNF and protects it from interacting with nonspecific binding partners while allowing it to associate with the BDNF receptor, tropomyosin receptor kinase B (TrkB). Nano-BDNF compared to BDNF is retained by brain after INB administration and has increased accumulation throughout the brain with targeting to the hippocampus and hypothalamus.

4.2 Introduction

Brain derived neurotrophic factor (BDNF) promotes neuron survival and long term potentiation, thus implicating it as a prime therapeutic candidate for a host of neurological disorders [210-215]. However, despite an endogenous transporter for BDNF across the BBB,

[4] This chapter previously appeared as a manuscript soon to be submitted.

its serum half-life is short [216-218]. Consequently, BDNF's efficacy for the treatment of CNS diseases after peripheral administration is low [219-222]. To overcome this problem, intranasal to brain (INB) administration has emerged as a promising route for delivering peptides and proteins to the CNS [223-228] . Briefly, the candidate drug is delivered high into the nasal cavity to the level of the olfactory bulb/cribriform plate where it can travel up along the olfactory and trigeminal nerves to reach the CNS without encountering the BBB [228, 229]. A recent report demonstrated efficacy in delivering intranasal insulin to the brains of Alzheimer's patients [230]. By bypassing the BBB and permitting only minimal exposure to the peripheral organs, INB administration can overcome the primary obstacles preventing BDNF delivery. Additional advantages of this approach include non-invasiveness and rapid onset of effects[228].

In its native, unmodified state, BDNF is not an immediately attractive candidate for intranasal delivery. In *Alcala-Barraza et al*., BDNF was delivered via INB administration, pharmacokinetic studies then demonstrated that BDNF was primarily localized in the olfactory bulb and trigeminal nerve with little appearance in more therapeutically relevant regions like the cortex or hippocampus. [231]. Poor penetration to the relevant portions of the brain has been attributed to entrapment and subsequent degradation of BDNF within the nasal mucosa [232]. Indeed, BDNF features cationic surface charges and extensive binding to a variety of polysaccharides [233, 234], inhibiting penetration through the negatively charged and sialic-acid-rich nasal mucosa [235].

Protein PEGylation, either through direct modification of the protein with a poly(ethylene-glycol) (PEG) chain or encapsulation in a nanoparticle with a PEG exterior, has been reported to increase nasal absorption [236, 237]. Unfortunately, PEGylation [238-241] can also sterically hinder the binding of cargo proteins with their receptors. In this particular context, BDNF must be released in a functionally active conformation to bind TrkB. Thus, an

ideal delivery vehicle should not only protect BDNF from mucosal interactions, but also release it in the native conformation and present minimum hindrance to interaction with TrkB.

Here, we present a block ionomer complex (BIC) formulation of PEG-PLE and BDNF that self-assembles in an isotonic solution at proper charge ratios. PEG-PLE, an anionic biocompatible polymer, interacts with the highly positively charged surface of BDNF while simultaneously constructing a PEG shell that protects BDNF from interactions with the nasal mucosa. This non-covalent assembly allows release of the native BDNF molecule to TrkB while protecting BDNF from non-specific interactions. Indeed, Nano-BDNF maintains activity before and after formulation in an NIH 3T3 cell line stably transfected with human TrkB. Furthermore, we demonstrate effective INB administration to the brain in CD-1 mice.

4.3 Materials and methods

4.3.1 Chemicals.

Methoxy-poly(ethylene glycol)-block-poly(L-glutamic acid sodium salt) (PEG-PLE) was purchased from Alamanda Polymers™ (Huntsville, AL). Its molecular mass determined by gel permeation chromatography was 13 KDa, and polydispersity index was 1.00-1.20; the PEG molecular mass was 4.5 - 5.5 KDa and the degree of polymerization of the PLE block was 45-55. Recombinant human BDNF was purchased from PeproTech (Rocky Hill, NJ). Human Serum Albumin (HSA), Bovine Serum Albumin (BSA) powder, and SuperSignal™ West Pico Chemiluminescent Substrate was from Thermo Fisher (Waltham, MA). Lactate buffered Ringer's solution (LR), uranyl acetate, Protease&phosphatase Inhibitor Cocktail, and agarose tablet were purchased from Fisher Scientific. Chloramine T, RIPA Buffer, urethane, and IgG from human serum were purchased from Sigma-Aldrich (St. Louis, MO); Mini-PROTEAN® TGX™ Precast Protein Gels, bio-safe commassie stain solution, sample loading and running buffers for electrophoresis were purchased from Bio-rad (Hercules, CA). Recombinant human TrkB Fc chimera protein (TrkB-Fc) was purchased from R&D systems

(Minneapolis, MN). $Na^{125}I$ was purchased from PerkinElmer Life Sciences (Boston, MA); GlutaMAX™ high glucose Dulbecco's Modified Eagle Medium (DMEM) was purchased from Invitrogen (Carlsbad, CA); Anti-Phospho-TrkA (Tyr490)/TrkB (Tyr516) rabbit monoclonal antibody (used in 1:1000 dilutions in 5% BSA), Anti-Phospho-p44/42 MAPK (ERK1/2) (Thr202/Tyr204) rabbit polyclonal antibody (used in 1:1000 dilutions in 5% BSA), Anti-p44/42 MAPK (ERK1/2) Rabbit monoclonal Antibody (used in 1:1000 dilutions in 5% non-fat dry milk), and HRP-conjugated secondary antibodies was purchased Cell Signaling Technologies (Beverly, MA); Anti-TrkB rabbit polyclonal antibody (used in 1:2000 dilutions in 5% non-fat dry milk) was purchased from Millipore (Bedford, MA); Tris-buffered saline (TBS) and Tris-buffered saline with 0.1% Tween 20 (TBST) 10X stock solutions were purchased from Boston Bioproducts (Ashland, MA).

4.3.2 Preparation and characterization of Nano-BDNF

Nano-BDNF was prepared by mixing BDNF and PEG-PLE in water. Briefly, a concentrated PEG-PLE solution was added drop-by-drop to a concentrated BDNF solution with gentle vortex at room temperature (RT). The mixture was then diluted with either 10mM phosphate buffer (pH = 7.4, PB) or LR to desired concentrations, and gently vortexed for another 30 seconds. Complexes were allowed to incubate at RT for 30 min before use in experiments. The charge ratio ($Z_{-/+}$) was calculated as the ratio of the total number of carboxylate groups in PEG-PLE (50) to that of arginine and lysine residues in BDNF (44, Based on the sequence provided by manufacturer).

4.3.3 Dynamic light scattering (DLS)

Nano-BDNF was prepared at various Z ratios and analyzed at 25°C using a Zetasizer Nano ZS (Malvern Instruments Ltd., UK) with a scattering angle of 173°.

4.3.4 Transmission electron microscopy (TEM)

Samples were deposited on copper grids coated with thin layers of carbon film and dried for 5 minutes. We performed positive staining for 10 seconds with 2% uranyl acetate which was then removed using filter paper. All samples were observed under a JEOL 100CX II transmission electron microscope set at 100kV. Images were acquired with a digital imaging system.

4.3.5 Atomic force microscopy (AFM)

Five μL of aqueous dispersion of .01 mg/mL native BDNF or Nano-BDNF ($Z_{-/+} = 10$) were deposited on the surface of a glass slide and air dried for 15 minutes. We utilized a MFP3D system (Asylum Research, Santa Barbara, CA) operated in tapping mode to image the particles.

4.3.6 Horizontal agarose gel electrophoresis (HAGE)

Samples containing 2μg of BDNF were electrophoresed through a 0.5% agarose gel at 80V for 1 hour in Tris/Glycine running buffer, and then stained using Bio-Safe Coomassie Stain solution (Bio-Rad, Hercules, CA). We obtained images using the FluorChem™ E series imager (ProteinSimple, San Jose, CA) with a 100ms exposure time. The center of mass as determined by optical density was obtained using ImageJ (NIH) and defined as the migration distance of the sample loaded in that lane.

4.3.7 Isothermal titration calorimetry (ITC)

ITC measurements were performed at 25.0 °C by using an auto-ITC200 titration calorimeter (Malvern Instruments, MA). The sample cell was loaded with 360 μl of BDNF solution (12.5 μM) in 10mM phosphate buffer, pH 7.4 and titrated with1 mM PEG-PLE solution in 2 μL aliquots with 3 minute intervals. The first injection was 0.2 μL. We used MicroCAl ORIGIN software to determine the site binding model which provided the best fit (lowest $\chi 2$ value) in order to obtain ΔH^0, K_d, and the stoichiometry of association. ΔG^0 and ΔS^0 were obtained using the following equations.

$$\Delta G = \Delta H - T\Delta S$$

$$\Delta G = \mathrm{RT}\ln k$$

4.3.8 Molecular dynamic (MD) simulations

MD simulations were performed in GROMACS 4.6.3 using OPLS-AA force field with slightly modified parameters to suit for PEG-PLE simulation as previously reported for PEGylated proteins [242]. We extracted the monomer structure (PDB ID 1BND) and constructed a dimer by placing to copies in close vicinity and performing a molecular dynamics simulation until steady state was achieved [14]. We generated a simulation box around the protein and polymers using the *editconf* module of the *GROMACS* package. The dimensions were selected so that the minimum distance between the protein molecule and the edge of the box was 9 Å. Protein models were solvated with the TIP4P water model and, wherever necessary, the system was neutralized with Na^+ and Cl^- ions using the program genbox. All MD simulations were performed at constant temperature of 300K and pressure of 1bar for a time period of 100 ns. The electrostatic surface potential of BDNF dimer was calculated using APBS tool 2.1. The numbers of hydrogen bonds and non-bonding contacts in the trajectory were calculated using HBplus program at each step of the trajectory [243] with parameters set the same as described by Baker and Hubbard[244] for maximum comparability. . The amino acid sequences forming the β-sheets and β-turns on BDNF are identified by PDBsum (https://www.ebi.ac.uk/thornton-srv/databases/cgi-bin/pdbsum/GetPage.pl?pdbcode=1bnd).

4.3.9 Protein thermal shift (PTS) assay

Samples were prepared by mixing 2 ug of BDNF or equivalent amount of Nano-BDNF ($Z_{-/+}$ = 1, 5, and 10) with the environmentally sensitive dye provided in the Protein Thermal Shift™ Dye Kit (Thermo Fisher). We performed the PTS assay using an Applied Biosystems® StepOnePlus™ 7500 Real-Time PCR system, and increased the temperature at a rate of 0.395°C/min. Melting temperature (T_m) was visualized by plotting the negative first-order

derivative of fluorescence over temperature (-dF/dT) versus temperature (T), and determined as the local minimum of the curve in the range of 70°C to 95°C.

4.3.10 Radioactive labelling of BDNF

^{125}I-BDNF and ^{125}I-Nano-BDNF were produced using a previously described Chloramine T method [12]. Briefly, 5ug of BDNF was mixed with 0.5 mCi Na^{125}I in a final volume of 45 µL sodium phosphate buffer (PB, 0.25 M, pH 7.5). Five µL of freshly prepared 2 µg/ µL chloramine-T solution in PB was then added to the mixture and incubated for 1 minute at RT. ^{125}I-BDNF was purified from the mixture with Illustra NAP-5 columns (GE Healthcare, Piscataway, NJ), and fractions were collected in Eppendorf tubes pretreated with either 1% BSA in lactated Ringer's solution (1% BSA-LR, for collecting ^{125}I-BDNF) or 0.1% PEG-PLE solution in LR (for collecting ^{125}I-Nano-BDNF) to prevent adsorption and the radioactivity of each fraction was counted in a PerkinElmer γ-counter. The integrity of ^{125}I-BDNF was determined by trichloroacetic acid (TCA) precipitation. Briefly, 1 µL of each fraction was added to 0.5 mL of 1% BSA-LR and then precipitated in 0.5 mL of 30 % TCA followed by centrifugation at 5400 g for 10 min at 4°C. The radioactivity in the supernatant and pellet were counted with γ-counter and the values used to calculate the integrity of ^{125}I-BDNF. Samples containing more than 100,000 count per minute (cpm)/µL of radioactivity and precipitate more than 95% in TCA were used for animal studies.

4.3.11 Cell culture and western blot

NIH 3T3 cells expressing TrkB were cultured in GlutaMAX™ DMEM supplemented with calf serum (10%), G418 (100 µg/mL) and Penicillin-Streptomycin (100 U/mL-100 µg/mL) and were maintained at 37 °C in a humidified CO_2 (5%) incubator. Half a million cells were seeded 24 hours before treatment. DMEM, 500ng/ml of BDNF, Nano-BDNF ($Z_{-/+}$ = 946), or equivalent amount of PEG-PLE polymer in the Nano-BDNF formulation were incubated with the cells for 5 minutes at 37°C in serum-free DMEM then moved to ice for 20

minutes and lysed using RIPA buffer with proteinase and phosphatase inhibitors. 10ug total protein from the cell lysates were loaded in each well of 7.5% TGX pre-cast gels and run at 150V for 1 hour. Proteins were then transferred to 0.45µm PVDF membranes at 500mA current for 1 hour. The membranes were then blocked in either 5% BSA (for detection of phosphorylated TrkB and ERK) or 5% non-fat dry milk (for detection of total TrkB and ERK) for 30 minutes at RT followed by an overnight incubation at 4 °C with primary antibody. Bands were visualized using HRP-conjugated secondary antibodies after incubation with SuperSignal™ West Pic Chemiluminescent Substrate for 1 minute. Chemiluminescent signal was recorded by a FluorChem™ E series imager, and quantified by Image J software (National Institute of Health (NIH), Bethesda, MD) using densitometry analysis.

4.3.12 Animals.

Charles River Laboratories supplied 8-week-old male CD-1 mice (24-28 g). Animals were housed and humanely handled in accordance with the Principles of Animal Care outlined by National Institutes of Health. They were allowed free access to food and water and were maintained under temperature, humidity, and light-controlled conditions. Institutional Animal Care and Use Committees (IACUC) of the University of North Carolina at Chapel Hill approved all experiments involving animal subjects.

4.3.13 INB administration and pharmacokinetic study.

INB administration of ^{125}I-BDNF or ^{125}I-Nano-BDNF was performed by pipetting 10µL of sample solution (total radioactivity is 1,000,000 cpm, Z ratio is 1100, PEG-PLE concentration is 0.91 mg/ml) with a thin tip advanced 5 mm into the left nare of the mice pre-anesthetized with an intraperitoneal injection of 0.2 mL of 40% urethane. The abdomen and rib cage of the mice were opened and venous blood was collected by cardiac puncture at each time point (5, 10, and 30 minutes) after INB administration. Next, 20 mL of PBS was perfused through the left ventricle of the heart. Mice were quickly decapitated and different brain regions

were immediately dissected on ice and weighed. Serum samples were obtained by centrifugation of whole blood at 5000g for 10 minutes. Peripheral organs were also collected and weighed. Levels of radioactivity in mice serum, brain regions, and peripheral organs were measured with a γ-counter.

4.3.14 BDNF efflux measurement.

To measure the rate of BDNF efflux from the brain, the mouse scalp was removed and a hole was made into the skull and 1 ul LR containing 500,000 cpm of ^{125}I-BDNF or ^{125}I-Nano-BDNF was slowly injected into the lateral ventricle of the brain. Mice were decapitated at 2, 5, 10, 20 minutes and the whole brain was removed and weighed. The level of ^{125}I-BDNF available for transport at t = 0 was estimated in mice that had been overdosed with urethane for 20 min and had received an injection of ^{125}I-BDNF 10 min earlier. To determine the residual levels of radioactivity in the brain, samples were counted with a γ-counter.

4.3.15 Statistical analysis.

Statistical analysis was done using Prism 6.01 software (GraphPad, CA). Statistical differences between treatment groups were determined using unpaired Student's t-test for groups of two and one-way ANOVA followed by Tukey's multiple comparison test for groups of three and above. A P-value less than 0.05 was considered significant. Results of all experiments are presented as mean ± SEM unless otherwise specified.

4.4 Results

4.4.1 A simple and straightforward nanoformulation.

Native BDNF forms large and highly heterogeneous aggregates with an effective diameter (D_{eff}) of about 600 nm and polydispersity index (PDI) greater than 0.4 (**Figure 4.1 A, B**). Thereby it cannot be used as an injectable pharmaceutical agent without proper formulation. Our approach addresses this problem by simple mixing BDNF and PEG-PLE aqueous solutions. The Nano-BDNF complexes form spontaneously, without sonication or other extensive agitation and are nearly monodisperse with PDI less 0.1 at the charge ratios ($Z_{-/+}$)

from 0.5 to 5 (**Figure 4.1 A, C**). The polydispersity increases above $Z_{+/-}$ = 5 but still remains relatively low. (Here and below we use the charge ratio i.e, the molar ratio of total number of glutamic acid residues on PEG-PLE to the total number of lysine and arginine residues on BDNF as a parameter defining the composition of Nano-BDNF mixtures). The particle size increases from 191 nm to 246 nm as $Z_{+/-}$ changes from 0.5 to 3 and then remains essentially constant. The transmission electron microscopy (TEM, **Figure 4.2**) and atomic force microscopy (AFM, **Figure 4.3**) suggest that Nano-BDNF consists primarily of smaller roundish shaped particles, while BDNF forms irregularly shaped aggregates.

4.4.2 Stoichiometry of the complex formation.

The stoichiometry of the complex formation was further characterized by horizontal agarose gel electrophoresis (HAGE). As expected, native BDNF (known to bind to various polysaccharides [233]) does not migrate in the agarose gel and remains immobilized in the well (**Figure 4.4 A**). In contrast, Nano-BDNF migrates towards the anode suggesting that the nanoformulation prevents BDNF immobilization on a gel and the complex particles acquired negative charge. Since BDNF alone is highly positively charged this indicates that the charges are neutralized by PEG-PLE. At a low $Z_{-/+}$ (lanes 1-10, **Figure 4.4 B**) Nano-BDNF migrates as a diffuse band, which grows as the amount of copolymer increases due to increasing complexation of BDNF. We then observe a second species forming (lanes 11-19, **Figure 4.4 B**) that is present until saturation, beyond which (lanes 20-24, **Figure 4.4 B**) we observe only one type of the complex species. By plotting the weighted distance of the complex migration in the gel over the charge ratio, the saturation $Z_{-/+}$ in this experiment is determined to be 6.4 (**Figure 4.4 C**), suggesting incorporation of a considerable excess of polyanion PEG-PLE. This value is further supported by the isothermal titration calorimetry (ITC) results where the exothermic reaction between BDNF and PEG-PLE was recorded until $Z_{-/+}$ of 6.8 is reached (**Figure 4.5**).

4.4.3 Molecular dynamics (MD) simulation of the complex formation.

Disproportioning (simultaneous formation of several distinct types of complexes) and overcharging (incorporation of an excess of polyion) is common for polyion complexes when interacting species can aggregate due to hydrophobic or other molecular interactions[245]. However, the charge excess of PEG-PLE (6 to 7 fold) incorporated in Nano-BDNF seems to be unusually high compared to similar complexes of other proteins and nucleic acids. To better understand possible molecular interactions between the reacting species we carried out MD simulations to model how the charged PEG-PLE associates with the local charge patches on the BDNF. We simulated single PEG-PLE chains and a BDNF dimer for 100 ns using four starting seed positions (**Figure 4.6 A**). We observed association and binding in every simulation, although the binding at any given residue was transient (**Figure 4.6 A-D**). The interaction interface consists of many residues on BDNF and PEG-PLE that come into close contact and are indicative of hydrogen bonding. We used HBplus, a program designed to identify and analyze hydrogen bonds, to determine if hydrogen bonds were formed. Indeed, we noted that there are residues with high frequency of interaction and H-bond formation with the glutamic acid residues of PEG-PLE (**Figure 4.7 A, B**, **Table 4.1**). BDNF is a compact globular protein consisting of approximately 70% ß-strands and 20% ß-turns [40]. Our simulations suggest that the binding sites are located primarily on the highly charged regions of the BDNF molecule, characterized by high β-turn/random coil content (**Figure 4.7 C**). Furthermore, due to the distance between the cationic patches (**Figure 4.8)**, a single PEG-PLE chain is unable to saturate both sites present in the BDNF dimer (**Figure 4.9 A**). Hence, we simulated higher molar ratios of PEG-PLE to BDNF (**Figure 4.9 B-F**). Taking into account all H-bonds that can occur we demonstrate that the stoichiometry of Nano-BDNF formation is between molar ratio of 2 and 3 (equivalent to $Z_{-/+}$ of 2.3 and 3.4).

While the MD simulation serves well to locate the binding sites on BDNF, it does not capture the full complexity of the BICs where more than one BDNF molecules actually participate in the interaction simultaneously. In context with the DLS data, we noticed that Nano-BDNF maintained an extremely narrow size distribution at $Z_{-/+}$ of 5 (PDI = 0.026), suggesting non-cooperative incorporation of free polymers into the micelle at charge ratios beyond stoichiometry [31]. At $Z_{-/+}$ of 10, we started to observe the presence of free PEG-PLE in the solution as evidenced by elevated polydispersity (PDI = 0.214), indicating the formation of a saturated BIC with $Z_{-/+}$ between 5 and 10. Hence, we hypothesize that Nano-BDNF can recruit free PEG-PLE past stoichiometry and form an overcharged species. Overcharged BIC's have been well documented before, attributing the incorporation of additional host polyelectrolytes (PEG-PLE in our case) to a favorable decrease of the free energy in the system as a consequence of the redistribution of interpolymeric ionic bonds between the BIC and the host polyelectrolyte that is in excess [246-248].

4.4.4 Stability of the complexes.

The nano-stabilization effect could also explain the formation of BIC in an isotonic solution like LR. Indeed, high salt concentrations usually lead to dissolution of BICs by electrostatic screening of its constituent parts [249]. Although Nano-BDNF prepared at low charge ratios ($Z_{-/+} \leq 3$) is able to form in LR, high ionic strength compromises its integrity, allowing BDNF to bind agarose (**Figure 4.10 A, B**). In contrast, overcharged Nano-BDNF ($Z_{-/+} > 3$) resists dissolution in higher ionic strength solutions (**Figure 4.10 C, D, E**) and a fraction is observed migrating even at 1.05 M NaCl. This fraction of Nano-BDNF features lower migration velocity in high ionic strength environments, possibly due to detachment of BDNF from the core of the complex and subsequent osmotic swelling of the remaining species which are the two typical steps of salt-induced BIC dissolution [248]. Furthermore, an excess of free

PEG-PLE ($Z_{-/+}$ = 100) in the solution decreased the amount of free BDNF that is stripped from the BIC, suggesting an easy approach to prepare stable BIC formulations.

Agarose gel shares several key characteristics with mucus in containing a microenvironment that is porous and contains polysaccharide chains. We propose that there is similarity in how the nanozymes would travel through the agarose gel and penetrate mucus. Mucus as a barrier features a highly glycosylated, porous mucin network which is aided by numerous mucosal proteins [250]. Albumin for example, is negatively charged and accounts for about 15% of nasal mucosal proteins [251]. While it associates with positively charged BDNF after incubation, it showed no interaction with Nano-BDNF (**Figure 4.11 C**). Similarly, serum IgG and secretory IgA do not compromise the integrity of Nano-BDNF as evidenced in HAGE experiments (**Figure 4.11 A, D**). This is likely because of the protective effect of the 5KDa PEG corona that is dense enough to shield the hydrophobic core of Nano-BDNF, which has been reported to facilitate nanoparticles diffusion through mucus [252].

4.4.5 Nano-BDNF releases active BDNF without compromising its intrinsic stability

The greatest challenge of the use of nano-particulate carriers is to deliver an uncompromised cargo to a specific location. In context, our objective is to maintain integrity of BDNF and release it to the relevant receptor (TrkB) in the brain. We characterized the interaction of TrkB and Nano-BDNF by incubating the soluble, recombinant extracellular domain of TrkB with BDNF and Nano-BDNF before HAGE experiments. Incubation of Native BDNF and TrkB indicated that they associate and migrate together (**Figure 4.11 B**, Lane 8). Similarly, when mixed with Nano-BDNF, TrkB associates in a 1:1 stoichiometry with the BDNF dimer and destabilizes the BIC, thus causing the band containing Nano-BDNF to proportionally decrease in intensity (**Figure 4.11 B**). Moreover, when Nano-BDNF was incubated with IgG and IgA at the same molar ratios, no change in the Nano-BDNF smear was

observed (**Figure 4.11 A, D**). Similar effects were observed on a low-affinity BDNF receptor, $p75^{NTR}$. (**Figure 4.11 E)**

While it was clear that TrkB could abstract BDNF from the BIC, concerns that BDNF was compromised, and thus inactive, remained. Indeed, previous reports indicated that interaction with polyelectrolytes can destabilize protein cargos [50-52]. We analyzed the protein stability in two distinct assays to determine how the stability and functionality were affected. We assayed the melting temperatures (T_m) of BDNF and Nano-BDNF using a fluorometric dye which responds to environmental changes, namely, hydrophobicity. We showed that Native BDNF has a T_m value of approximately 83°C (**Figure 4.12 A**), which is consistent with previous reports that BDNF denaturation occurs between 60°C and 90°C [253]. Similarly, we demonstrate that Nano-BDNF has a slightly higher stability (~ 0.5°C) at $Z_{-/+}$ of 5 and 10 (**Figure 4.12 B**). In order to determine if functionality was maintained as well, we incubated BDNF and Nano-BDNF with NIH 3T3 cells, a cell line which stably expresses TrkB and does not produce BDNF. Activation of TrkB was tested using a phosphospecific antibody to detect the phosphorylated TrkB kinase domain. TrkB phosphorylation is observed at the same level when stimulated with BDNF and Nano-BDNF, indicating that the vehicle does not inhibit activity or association (**Figure 4.13 A**). Phosphorylated ERK, a downstream target kinase [254], was also observed at similar levels after TrkB stimulation with BDNF and Nano-BDNF (**Figure 4.13 B**) [53, 54].

4.4.6 Nano-BDNF significantly enhanced the delivery of BDNF to brain regions after INB administration.

We next performed an *in vivo* pharmacokinetic study to evaluate the ability of this formulation to deliver BDNF to the brain after INB administration, which is known to rapidly deliver therapeutic proteins to a wide range of brain regions [228]. Indeed, in most of the brain regions, both native and nanoformulated ^{125}I-BDNF was readily detected as soon as 5 min. after INB administration (**Figure 4.14**). Within 30 min. after INB administration, the level of

Nano-BDNF accumulation in the brain was significantly higher than that of the native BDNF in all studied brain regions, except for midbrain, where there was a trend for the increase. Comparing the areas under the curve (AUC) 0 to 30 min for the native BDNF and Nano-BDNF suggests that the nanoformulation increases the delivery of the neurotrophin in all these regions, notably in the olfactory bulb (~6.7 times), hippocampus (~9.9 times), and brainstem (~4.0 times) (Figure 13B and Supplementary Table S2). The overall increase for the whole brain was as also significant albeit less dramatic (~3.5 times) (**Table 4.2**). By dividing the areas under the curve (AUC) for different brain regions we further concluded that relative to the native BDNF, the brain regional distribution pattern of Nano-BDNF was very different. Specifically, there was an increase of the Nano-BDNF distribution to hippocampus vs. olfactory bulb, hypothalamus and the rest of the brain (**Figure 4.15**). In contrast, the distribution to pons and medulla was only slightly increased vs. to the rest of the brain, while the *relative* distribution to the midbrain was decreased vs. both olfactory bulb and the rest of the brain.

We also show that the amount of Nano-BDNF distributed in the serum after intranasal administration was lower than the native BDNF (**Table 4.2)**. Analysis of the peripheral distribution of Nano-BDNF suggests that within 30 min following INB delivery, Nano-BDNF was detected in liver, spleen, kidney, lung and heart – albeit at levels less than 0.5% inj/g. Marginally higher amounts of the INB delivered Nano-BDNF were found in the esophagus, trachea, and stomach but these amounts still were in the range of 1-2% inj/g tissue (**Figure 4.16**) and were likely due to limitations of our INB procedure in a mouse ("post nasal drip"). In addition, literature [217] as well as our own studies suggest that there is a brain-to-blood efflux mechanism for native BDNF. However, we observed much less efflux of Nano-BDNF from brain to blood when it was directly injected to cerebral ventricle (ICV) relative to native BDNF (**Figure 4.17**). This observation may help to explain why despite the increased

accumulation of Nano-BDNF in the brain, its release into the serum was not increased to the same extent.

The serum clearance and brain uptake of Nano-BDNF after intravenous (IV) administration is shown in **Figure 4.18**.Consistent with ICV data IV Nano-BDNF displays decreased efflux and greater brain uptake than the native BDNF. Comparing the Brain/Serum ratios for IV (~60 to 80 µl/g) and INB (~1000 to 3000 µl/g) Nano-BDNF suggests that blood to brain route could explain only ~2 to 8% of whole brain uptake of Nano-BDNF after nasal administration. Overall, our data suggest that Nano-BDNF delivered by the INB route has improved delivery to regions of the brain (the brainstem and hippocampus) that are important targets for RTT therapeutics. Moreover, the relatively low distribution to the blood and peripheral organs should decrease the risk of side effects associated with systemic exposure to Nano-BDNF. Taken together our data represent a compelling rationale for advancing the development of Nano-BDNF as a treatment for this disease.

Passage of therapeutic proteins from nose to brain is known to be associated with at least two pathways: the peripheral olfactory system pathway (transporting to the olfactory bulb and rostral brain regions), or the peripheral trigeminal system pathway (transporting to the brain stem and caudal brain regions) [228]. The distribution pattern of native BDNF suggests the shorter, olfactory-associated pathway is its primary route, whereas Nano-BDNF appears to use both pathways to enter the brain (Figure 13A). We postulate this is due to reduced binding to the brain extracellular matrix and increased diffusion rates of BDNF as a result of encapsulation inside PEG-coated nanoparticles [255].

Higher accumulation of BDNF in the BIC formulation could also be related to decreased efflux from brain to the blood. Indeed, BDNF is known to be transported from the brain to the blood in association with the reabsorption of the cerebral spinal fluid [217]. A recent report has shown that the distribution of INB administered therapeutic proteins in the

brain is carried by bulk flow within the perivascular space (PVS) of cerebral blood vessels [229] where CSF plays an important role in the clearance of substances [256]. Therefore, we hypothesize that Nano-BDNF could reduce the rate of BDNF efflux. This hypothesis is tested by intracerebroventricular (ICV) injection of ^{125}I-BDNF into the mouse brain followed by measurement of its radioactivity in the brain at different time points after injection (**Figure 4.17**). Consistent with our hypothesis, we observed significantly slower efflux rate of Nano-BDNF from brain to blood as compared to that of native BDNF.

4.5 Conclusion

In this manuscript, we present a simple and readily translational formulation of BDNF. As a protein delivery system, Nano-BDNF remains stable in high salt concentrations, protects BDNF from non-specific binding within the environment, and readily releases active BDNF upon interaction with its receptor. Most current nanoparticulate formulations of BDNF (PLGA microspheres [257], nanoporous PLE particles [258], hydrogel scaffolds[259]) controls its release temporally, ie. sustained release during a period of time. In contrast, Nano-BDNF releases BDNF in a spatially controlled manner. That is, the release of BDNF is triggered by the presence of a BDNF receptor. At the same time, Nano-BDNF maintained the advantages of PEGylated nanoparticles in terms of cargo protection and mucus penetration. The delivery of Nano-BDNF significantly increased BDNF accumulation in a variety of brain regions via the INB route, and decreased the efflux rate of BDNF from brain to blood after ICV injection.

4.6 Future directions

In this chapter we focused our research on the composition of Nano-BDNF and its application for intranasal-to-brain delivery. We are also interested in exploring the possibility of using this formulation for BDNF delivery via the IV route. During my graduate study, I have also contributed to some experiments led by Dr. Xiang Yi to explore PK differences between native BDNF and Nano-BDNF after IV administration. This is a big part of our plan for the

future of this project. Some of these data has already been incorporated in the main text of this dissertation (**Figure 4.17, Figure 4.18**), but others were not since they were not relevant to the intranasal delivery story. We have also worked in collaboration with Dr. Rajkumar Verma to demonstrate preliminary therapeutic efficacy of Nano-BDNF in stroke (Pharmacol Biochem Behav. 2016 Sep 13;150-151:48-56. doi: 10.1016/j.pbb.2016.09.003). Here I'm incorporating the preliminary data obtained from experiments led by Dr. Xiang Yi (**APPENDIX I**) and the abstract of the published paper from Dr. Rajkumar Verma's work (**APPENDIX II**) in the appendices of this dissertation for completeness.

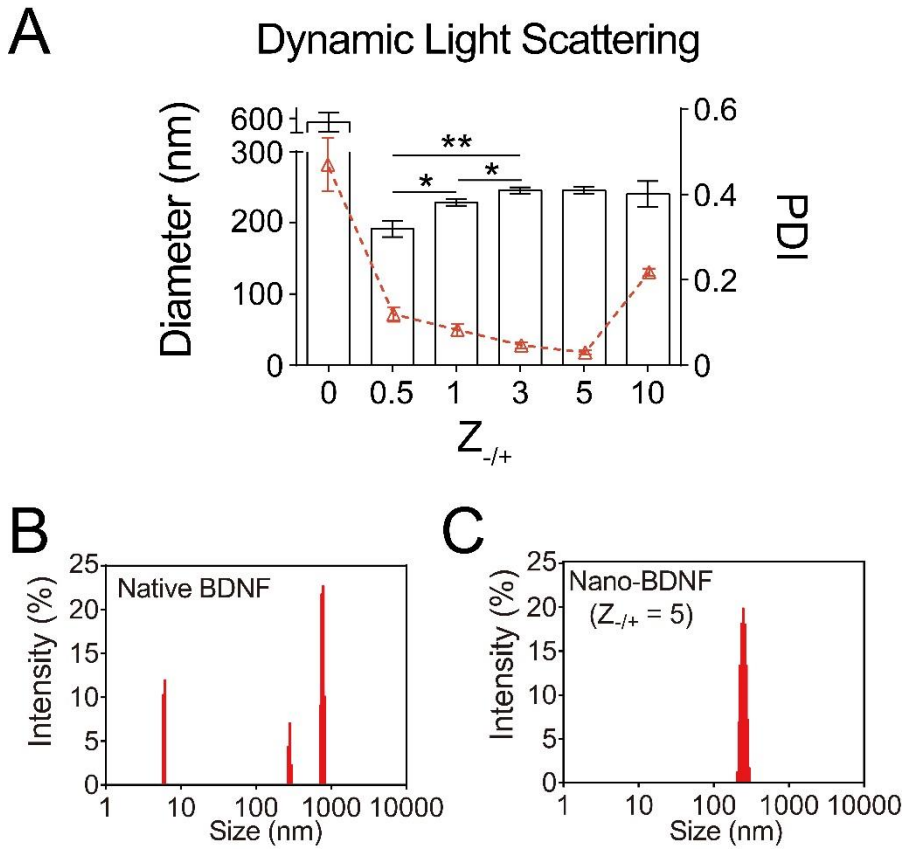

Figure 4.1 Dynamic light scattering.

A. Effective diameter of native BDNF and Nano-BDNF samples prepared at different $Z_{-/+}$ values were measured with DLS. The Z-averaged diameter was plotted to the left Y-axis, and the PDI was plotted to the right Y-axis (n = 5). Statistical significance is defined as $P < 0.05$, and indicated by: *, $p < 0.05$; **, $p < 0.01$; **B-C.** Representative intensity-size graphs of native BDNF and Nano-BDNF ($Z_{-/+} = 5$).

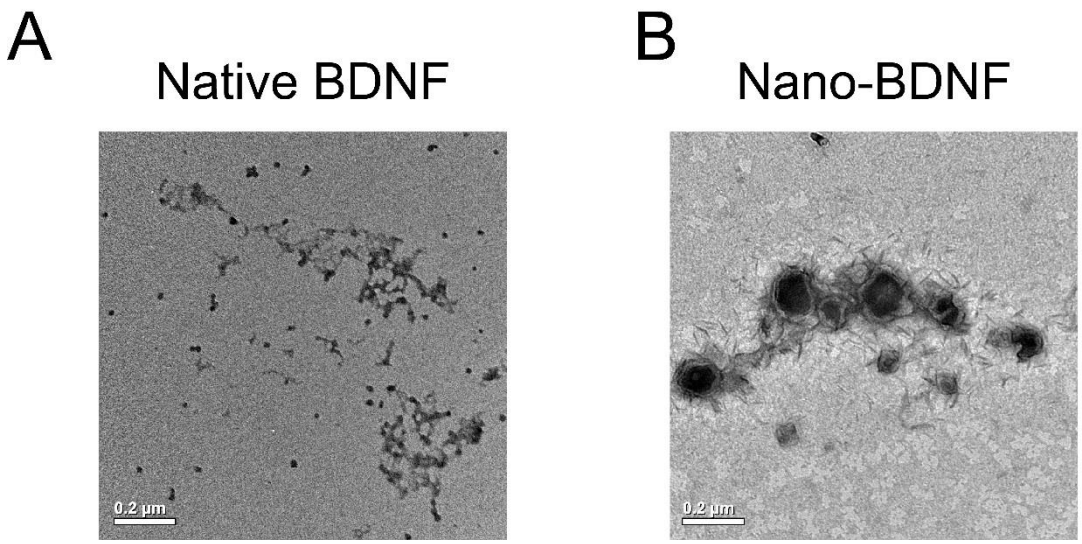

Figure 4.2 Representative TEM images.

A. native BDNF and **B.** Nano-BDNF ($Z_{-/+}$ = 10).

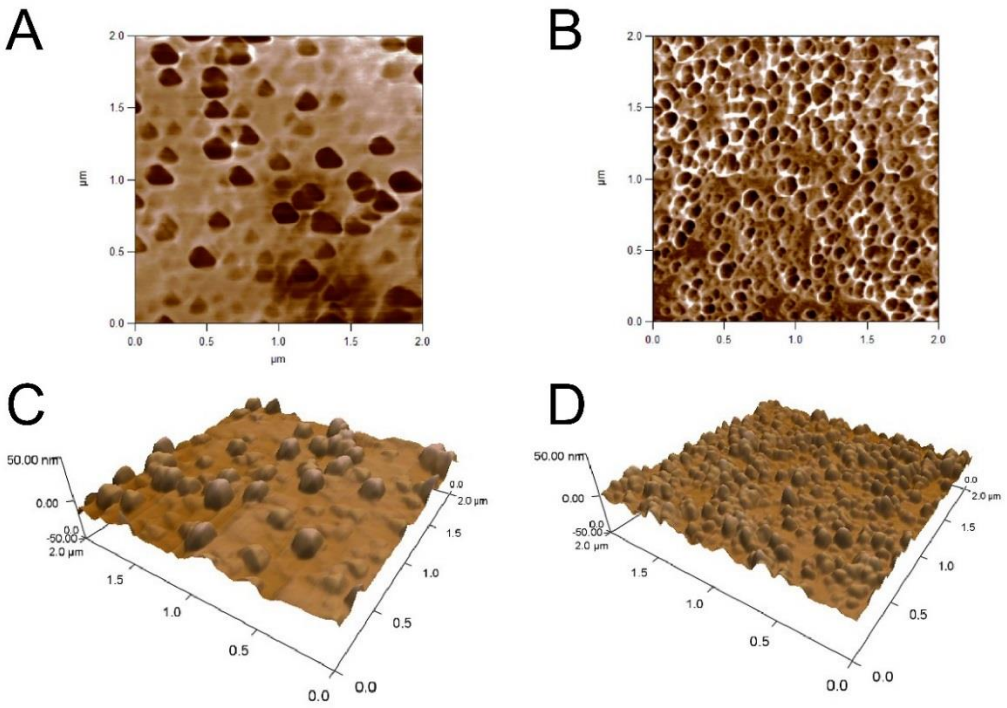

Figure 4.3 Representative AFM pictures.

Phase diagrams (**A,B**) and 3D topographies (**C,D**) of native BDNF (**A,C**) and Nano-BDNF (Z-/+ = 10, **B, D**).

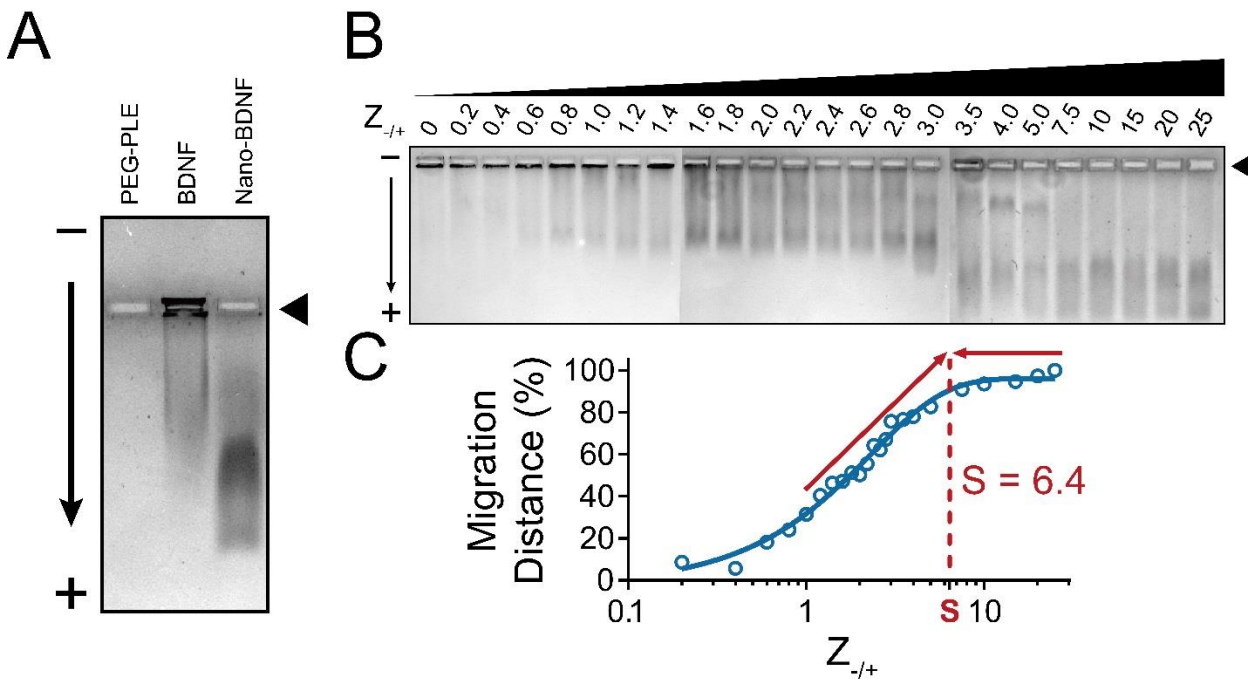

Figure 4.4 Horizontal agarose gel electrophoresis.

A. The electrophoretic mobility of PEG-PLE (lane 1), Native BDNF (lane 2) and Nano-BDNF ($Z_{-/+}$ = 100, lane 3) were determined by running on a 0.5% agarose gel (pore size around 500nm [260]) at 80V for 1 hour. Samples were loaded in the rectangular wells indicated by the black triangle. The "-" and "+" signs denote cathode and anode, respectively. The black arrow indicates direction of electron flow. Commassie Blue staining was performed to visualize BDNF, since it has minimal staining of free PEG-PLE copolymer. Despite the positive charge on BDNF at the pH of the running buffer, a small fraction of BDNF was always observed to migrate towards the anode, possibly due to binding and subsequent charge-conversion by free agarose oligomers and/or polymers that are not completely immobilized in the gel. **B.** The electrophoretic mobility of Nano-BDNF prepared at different $Z_{-/+}$ values were evaluated and presented in the same way as described in **A.** Lanes 1–24 represent samples with different $Z_{-/+}$ values from 0 to 25. **C.** To quantify the migration distance of BDNF, we located the center of mass of the BDNF smear in each lane of **B.** and measured its distance from the loading well of that lane. The distances were then quantified and normalized with the value obtained at $Z_{-/+}$ = 25 being 100% and plotted against their $Z_{-/+}$ values on a logarithmic scale. A sigmoidal curve was fitted to the plot, and the minimum saturation $Z_{-/+}$ value "S" was determined to be about 6.4 by elongating and intersecting the two linear portions of the curve on the graph.

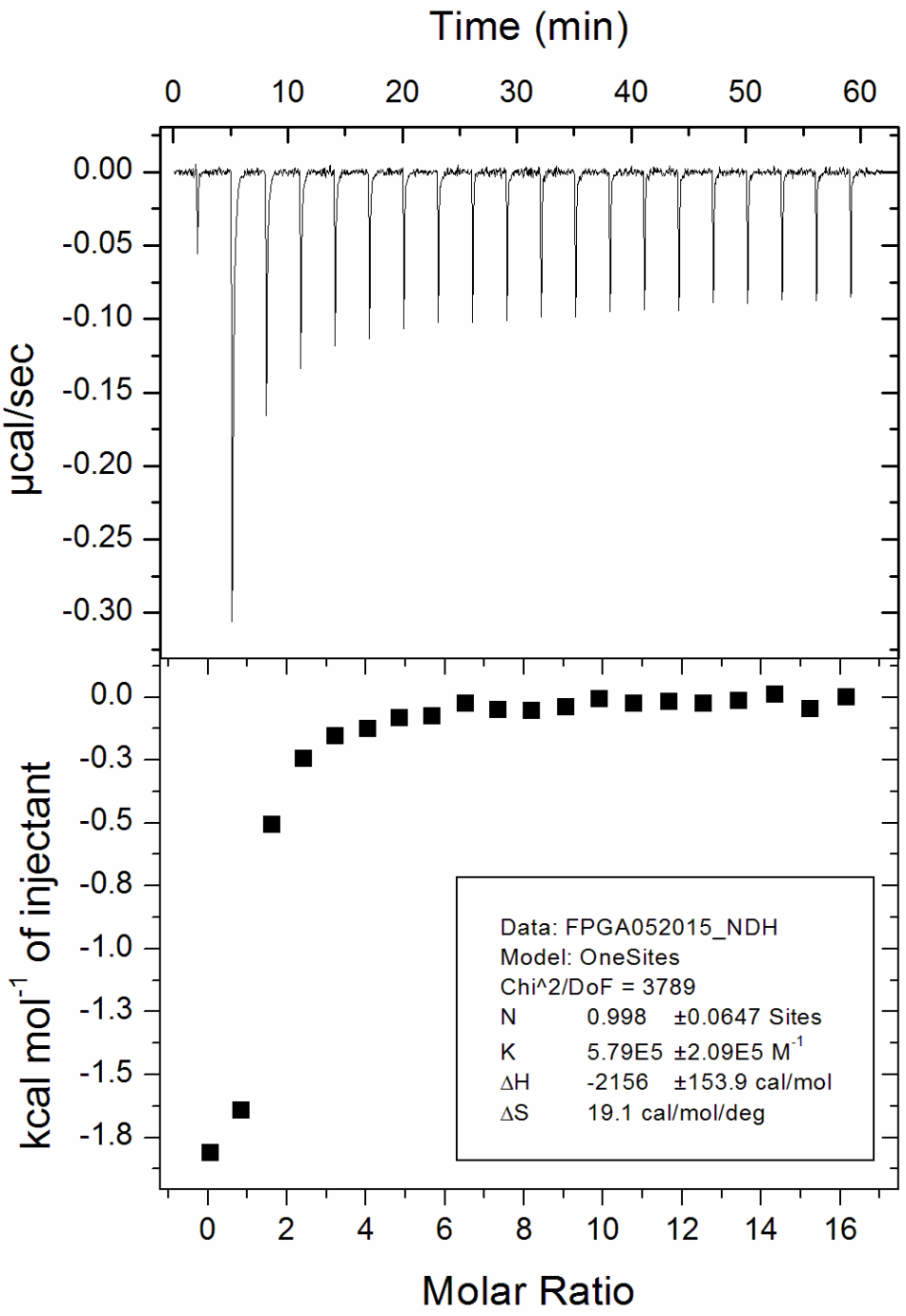

Figure 4.5 ITC measurement of complexation process between BDNF and PEG-PLE

ITC data obtained by slowly titrating PEG-PLE solutions into an isothermal chamber containing BDNF corroborates the saturation $Z_{-/+}$ of Nano-BDNF to be between 6 and 7.

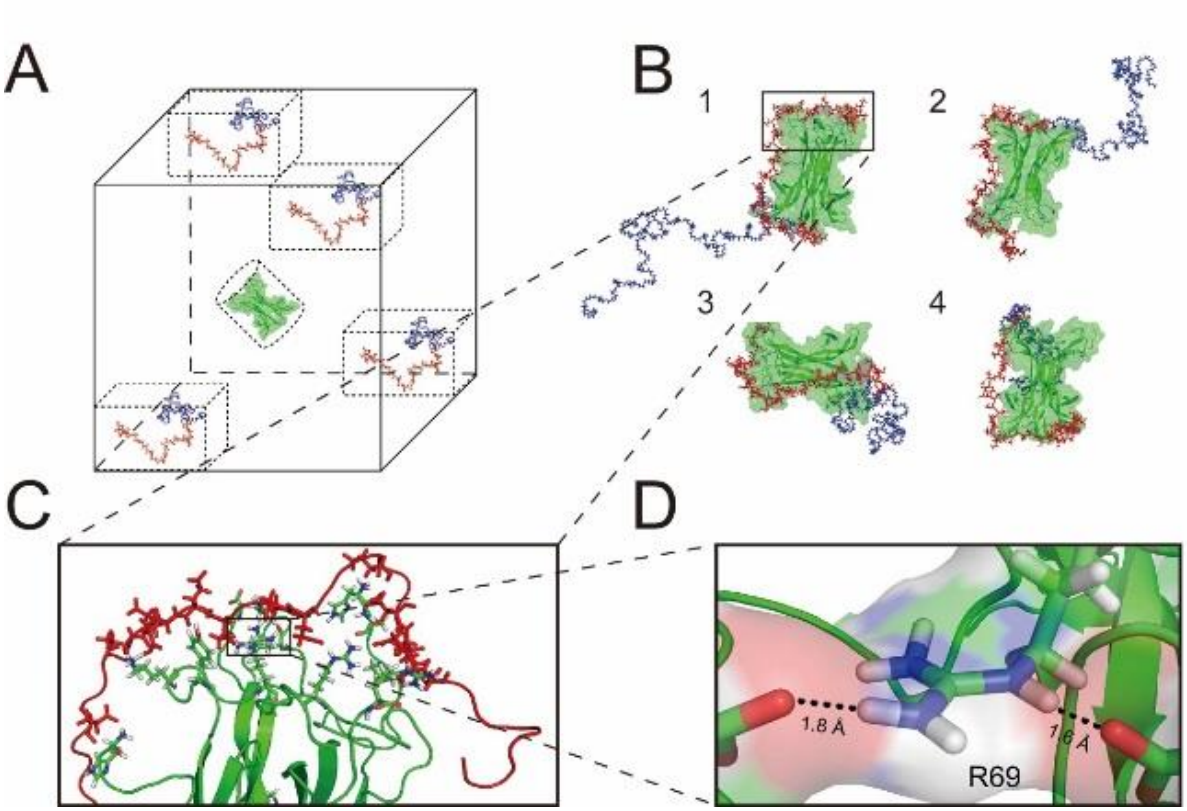

Figure 4.6 Molecular dynamics simulation.

A. Simulations were prepared with PEG-PLE in various starting positions (Boxed Polymers). **B.** Final frames of all the trajectories indicated tight binding between BDNF (visualized in cartoon mode) and PEG-PLE (visualized in stick mode) resulted from the simulations. **C.** Magnified picture of the squared area shown in **B**. The amino acids on BDNF that are within 3.9 Å of a glutamic acid residue on PEG-PLE are visualized in stick mode. **D.** Magnified picture of the squared area shown in **C**. Two hydrogen atoms on Arginine 69 of BDNF are shown to be located within 2 Å of oxygen atoms on PEG-PLE.

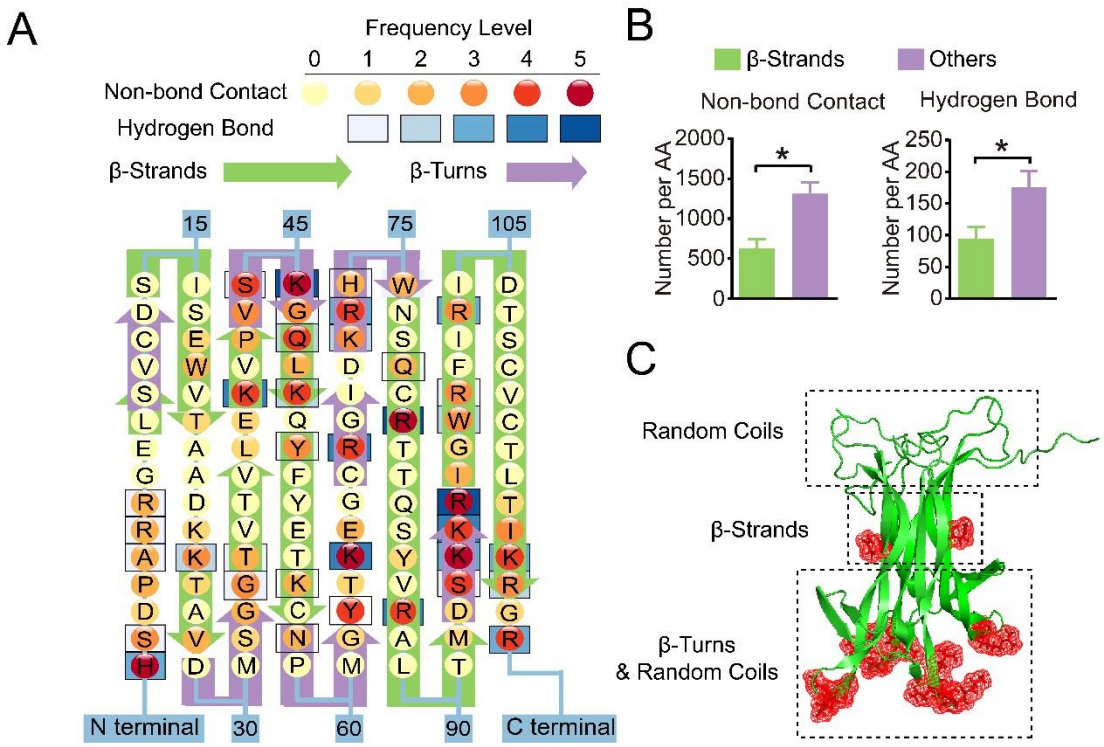

Figure 4.7 Binding site determination.

A. Frequency map of BDNF-polymer interactions on each amino acid of BDNF. The frequency levels of hydrogen bonds and Non-bonding contacts are determined separately based on their total counts (summarized in table 1) in the trajectories obtained from 4 independent simulations with 1 BDNF dimer and 1 PEG-PLE chain. **B.** Quantification of BDNF – polymer interaction occurring on β-strands versus other structural domains. The result is presented as the number of occurrences averaged by the number of amino acids (denoted by AA in the figure) forming each structural domain. "*" denotes statistical significance between two groups ($P < 0.05$). **C.** Cartoon visualization of a BDNF dimer molecule with illustrations of predominant structural domains at each part of the protein. The red meshes represent amino acids that are actively involved in the binding between BDNF and its receptor, TrkB.

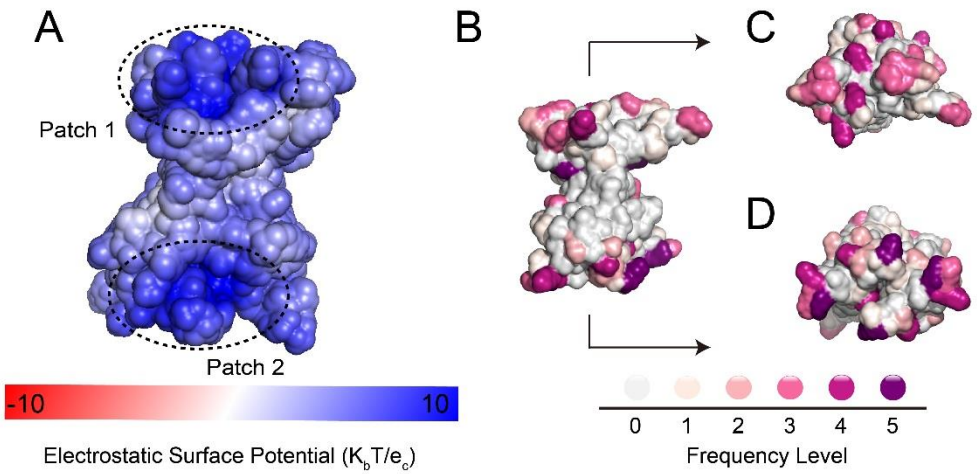

Figure 4.8 Identification of charge patches on BDNF and 3D density map of BDNF binding sites with PEG-PLE.

A. Electrostatic potential of BDNF plotted on the solvent-accessible surface. Potential surfaces are visualized ($-5K_bT/e_c$ (red) and $+5K_bT/e_c$ (blue) around a BDNF dimer molecule at pH 7, calculated with APBS tool 2.1. The two major cationic cavities are highlighted with the dashed circles. **B.** 3D-Heatmap of BDNF-polymer hydrogen bonds on each amino acid of BDNF. Frequency levels were defined in the same way as shown in Figure 3; **C.** Top view of **B.**; **D.** Bottom view of **B.** Frequency levels in **B**, **C**, and **D** are defined as described in **Table 4.1**.

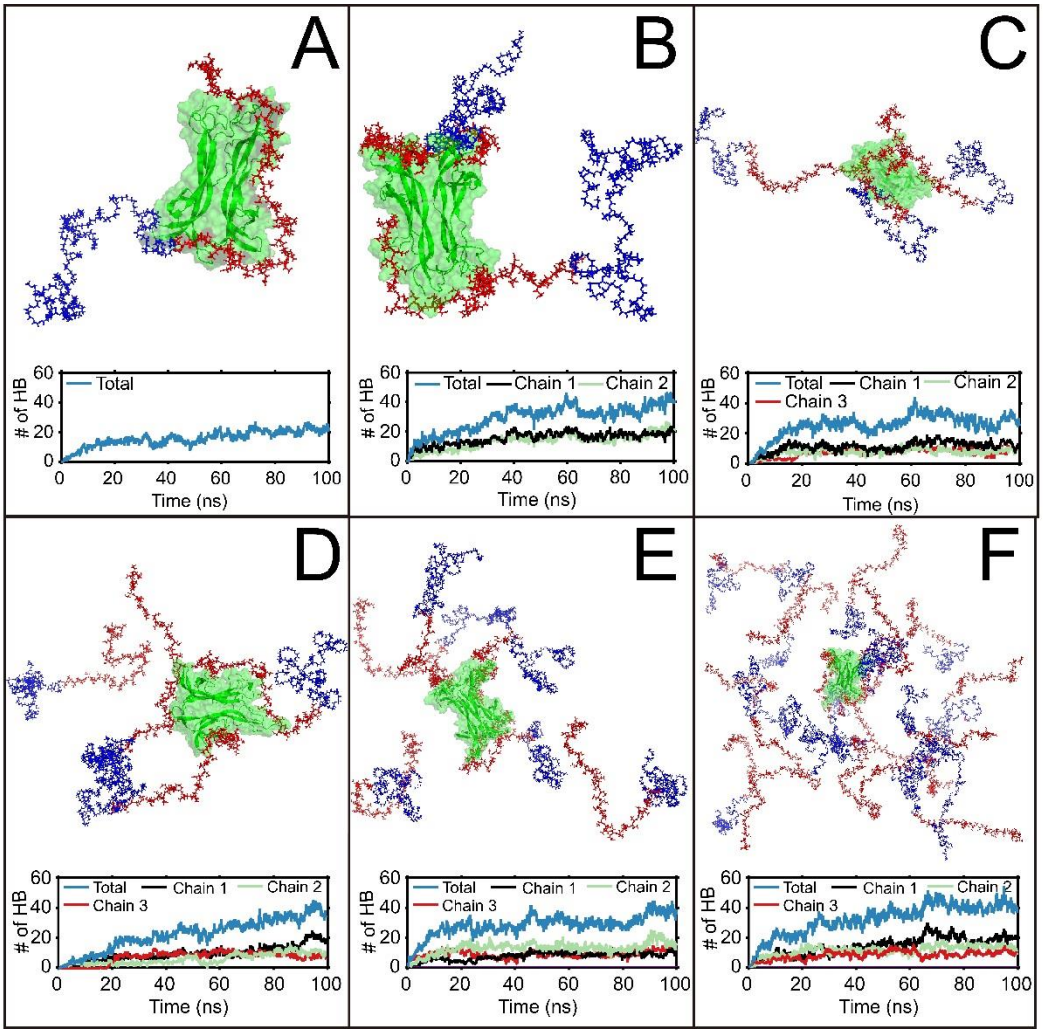

Figure 4.9 Molecular dynamics simulation of 1 BDNF molecule binding to different number of PEG-PLE chains.

A-F. Final frames of simulations with 1 BDNF molecule binding to 1, 2, 3, 4, 6, and 20 PEG-PLE chains, respectively. The number of hydrogen bonds occurred during the simulation were plotted against time: blue curves represent the total number of hydrogen bonds between BDNF and all polymer chains in the simulation; black, green, and red curves each represent the number of hydrogen bonds formed between BDNF and one single polymer chain. Green: cartoon and surface illustrations of a BDNF dimer molecule; Blue: stick illustration of PEG; Red: stick illustration of PLE. The number of hydrogen bonds formed was plotted as a function of simulation time under each graph. In all simulations a maximum number of 3 polymer chains were observed to be able to form hydrogen bonds with the BDNF dimer.

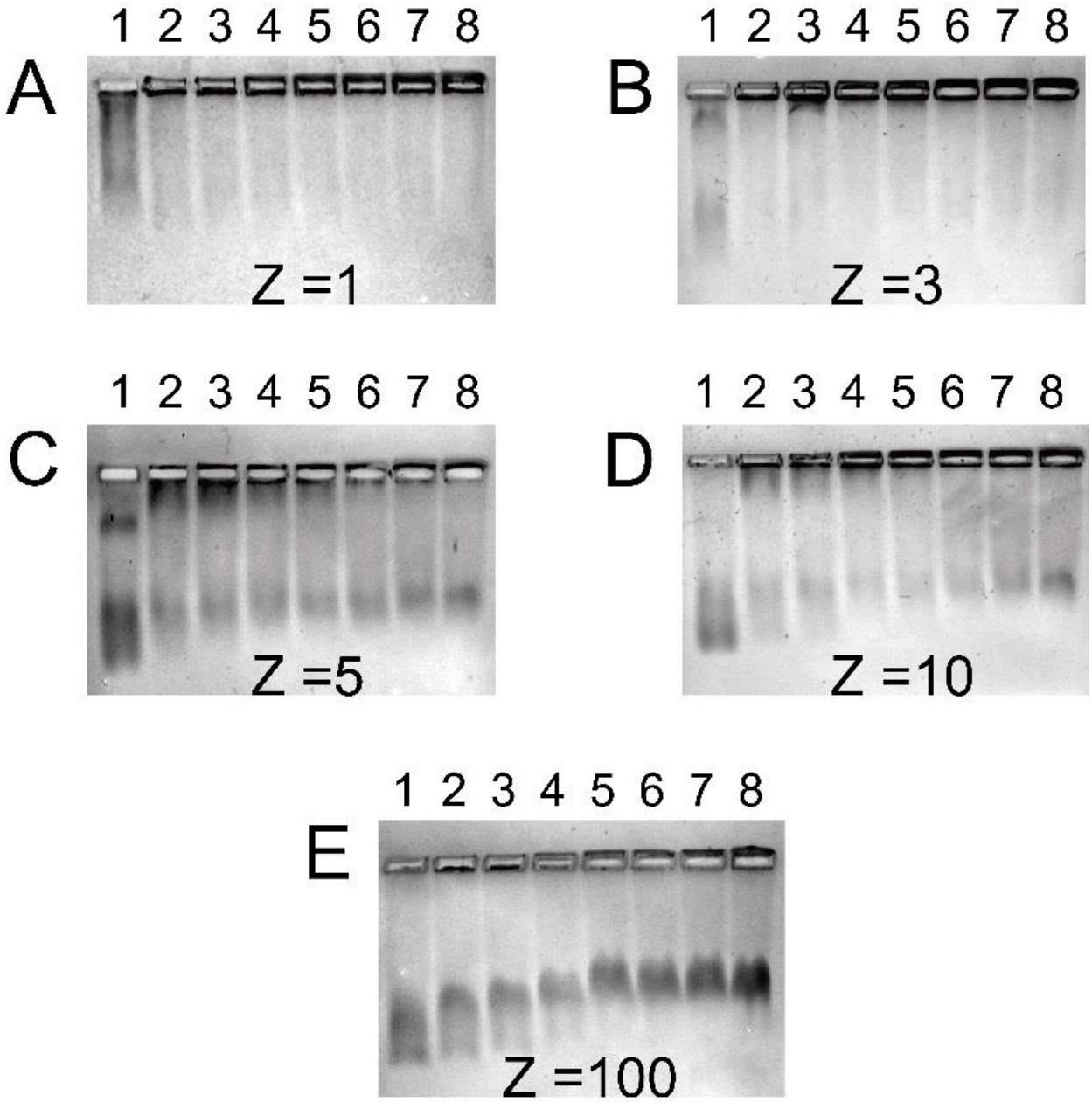

Figure 4.10 NaCl and TrkB challenge studies.

A-E. Nano-BDNF samples of different $Z_{-/+}$ values (1, 3, 5, 10, and 100, as indicated in the graphs) were prepared in NaCl solutions before horizontal agarose gel electrophoresis. The concentration of NaCl in the Nano-BDNF samples gradually increased from lane 1 to lane 8 (0M, 0.15M, 0.30M, 0.45M, 0.60M, 0.75M, 0.90M, and 1.05M, respectively). The amount of free BDNF in each experimental condition can be estimated by the staining at the edge of the respective loading well.

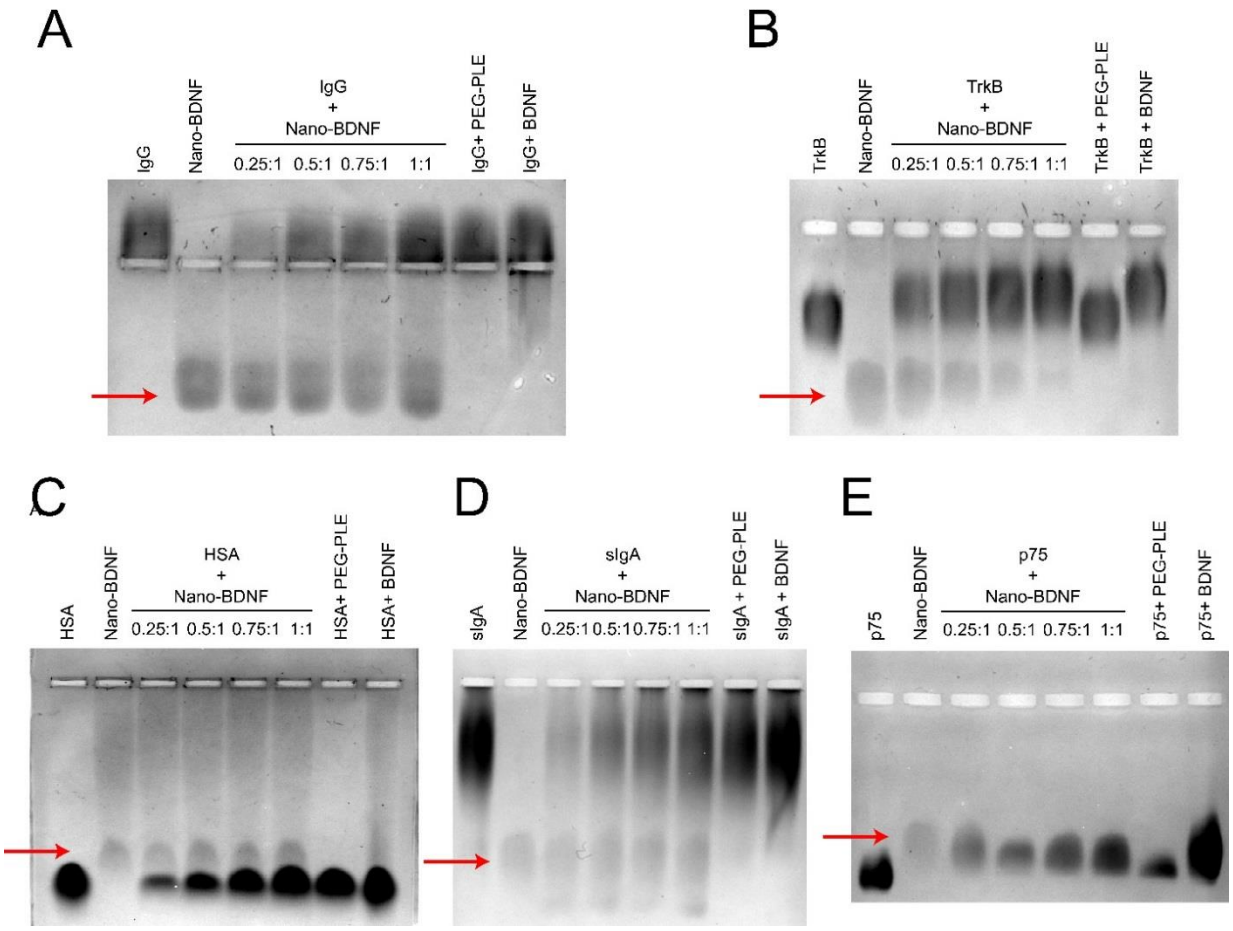

Figure 4.11 Nano-BDNF protects BDNF from challenges of nasal defensive proteins, while readily releasing BDNF upon incubation with the BDNF receptors, TrkB and p75.

Different competitors, including nasal mucosal proteins (**A.** IgG, **C.** HSA, **D.** sIgA), and BDNF receptors (**B.** TrkB, **E.** $p75^{NTR}$) were incubated with Nano-BDNF ($Z_{-/+}$ = 200) in LR for 30 minutes before subjected to horizontal agarose gel electrophoresis. From left to right, lane 1: Competitor; lane 2: Nano-BDNF; lane 3: Competitor incubated with Nano-BDNF (molar ratio 0.25 : 1); lane 4: Competitor incubated with Nano-BDNF (molar ratio 0.5 : 1); lane 5: Competitor incubated with Nano-BDNF (molar ratio 0.75 : 1); lane 6: Competitor incubated with Nano-BDNF (molar ratio 1:1); lane 7: Competitor incubated with PEG-PLE (same amount as in lane 6); lane 8: Competitor incubated with native BDNF (molar ratio 1:1). Red arrows indicate the location of Nano-BDNF bands in each graph.

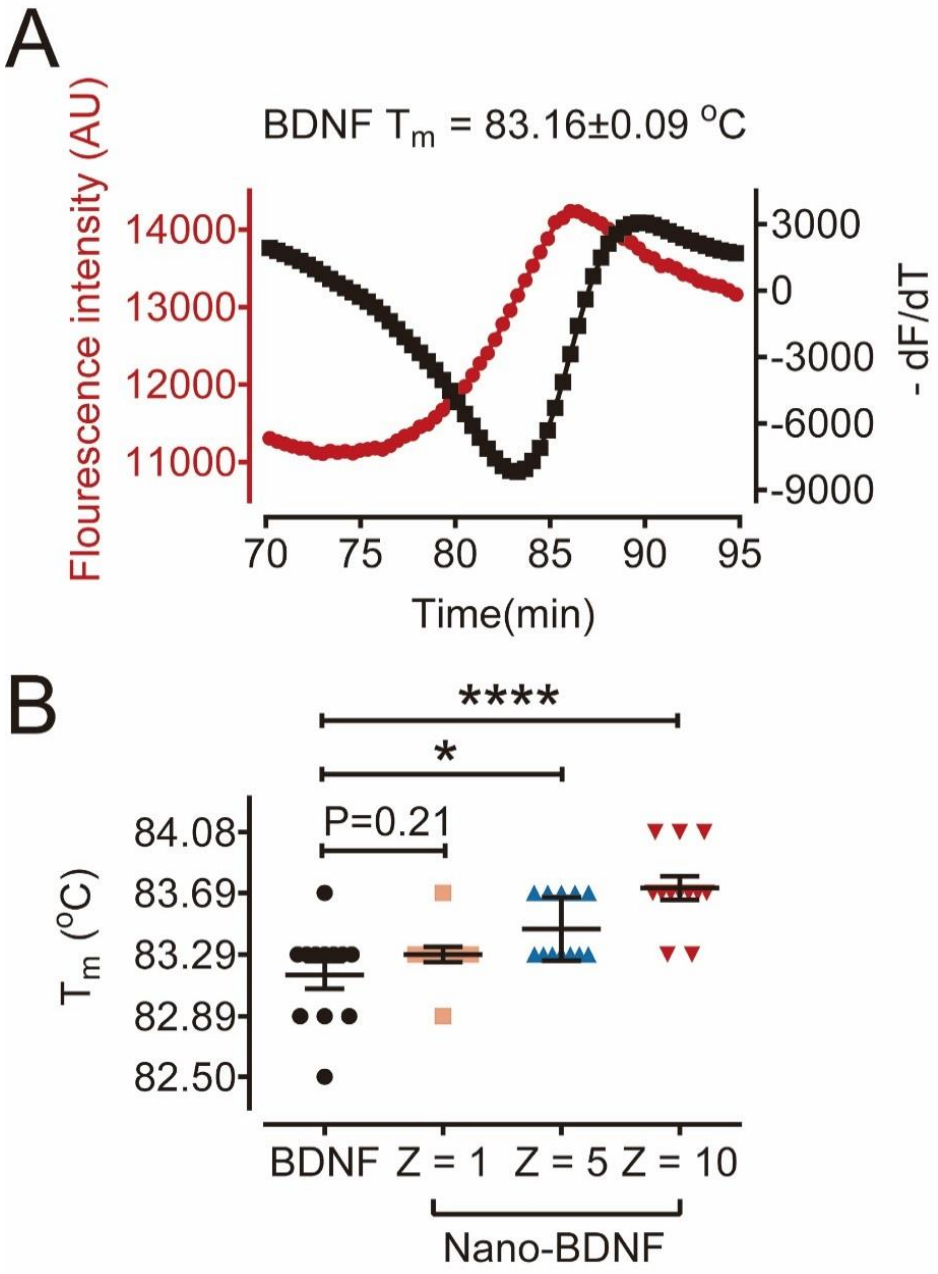

Figure 4.12 Protein thermal shift assay.

A. A representative graph demonstrating the melting curve of native BDNF in the proprietary assay buffer in the Protein Thermal Shift™ Dye Kit. The red dots denote fluorescent signal intensity (left Y-axis), and the black triangles denote the negative first-order derivative of fluorescent signal intensity (right Y-axis) in the temperature range of 70°C to 95°C. The T_m of native BDNF was determined to be 83.16 ± 0.09°C as described in the methods section. **B.** Scatter bar plot summarizing the T_m value of native BDNF and Nano-BDNF at $Z_{-/+}$ = 1, 5, and 10 (n = 12). Symbols above the horizontal lines denote significance levels compared to the native BDNF group, and are indicated by * ($P < 0.05$) and **** ($P < 0.0001$).

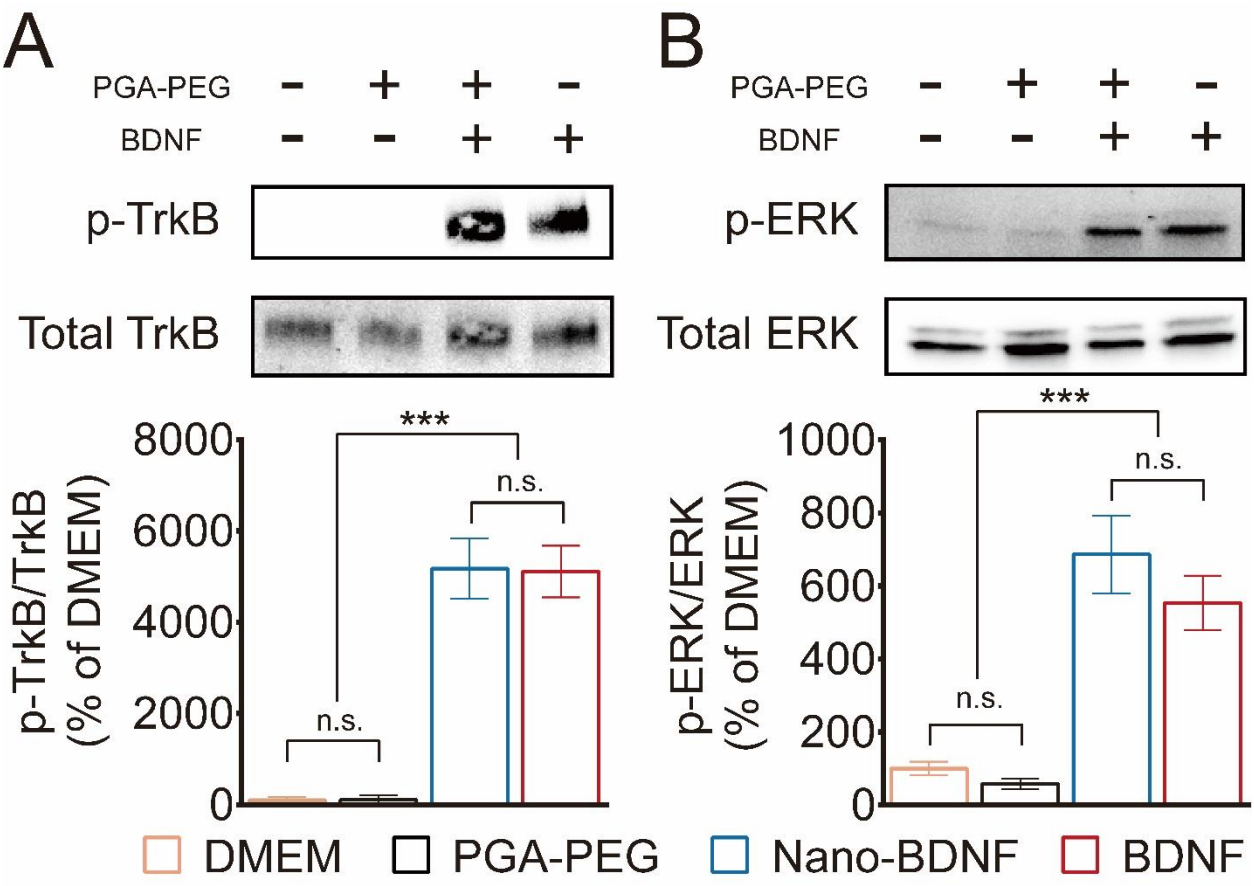

Figure 4.13 Densitometry quantitation of Western blots for lysates from NIH 3T3 cells stably expressing TrkB receptor.

A. Western blots showing the level of TrkB receptor phosphorylation at the site of Tyrosine 515 after treatment with (from left to right) DMEM, PEG-PLE, Nano-BDNF or BDNF for 5 minutes at 37°C (n = 6). Quantification of band density was presented by the ratio of phosphorylated TrkB over total TrkB.; **B.** Western blots showing the level of ERK phosphorylation in the same of samples as described in **A.** Data were analyzed with unpaired Student's t-test between each two groups; *** denotes $p<0.001$, and n.s. denotes no significant difference.

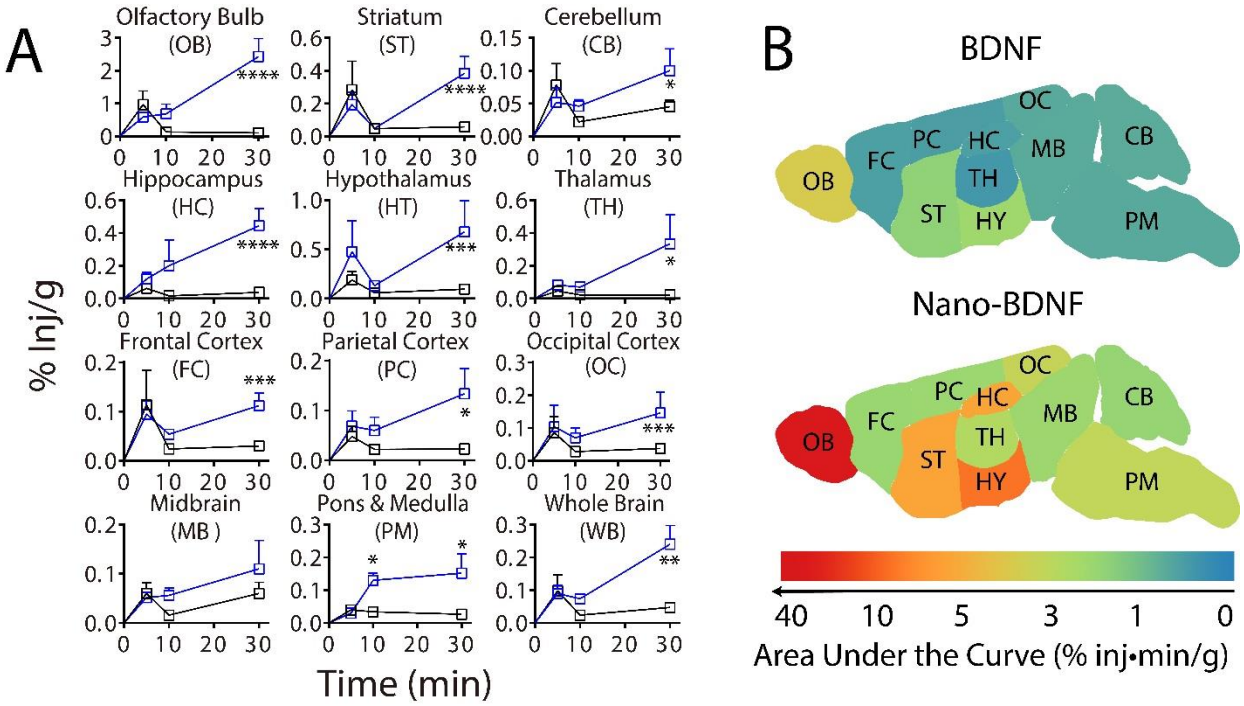

Figure 4.14 Uptake of 125I-BDNF and 125I-Nano-BDNF in different brain regions over 30 min after IN delivery.

A. Heatmap demonstrating the area under the curve (AUC) of BDNF or Nano-BDNF exposed to different brain regions over a period of 30 min. after INB administration. **B.** Significant differences in the accumulation at a variety of brain regions was observed between BDNF and Nano-BDNF.

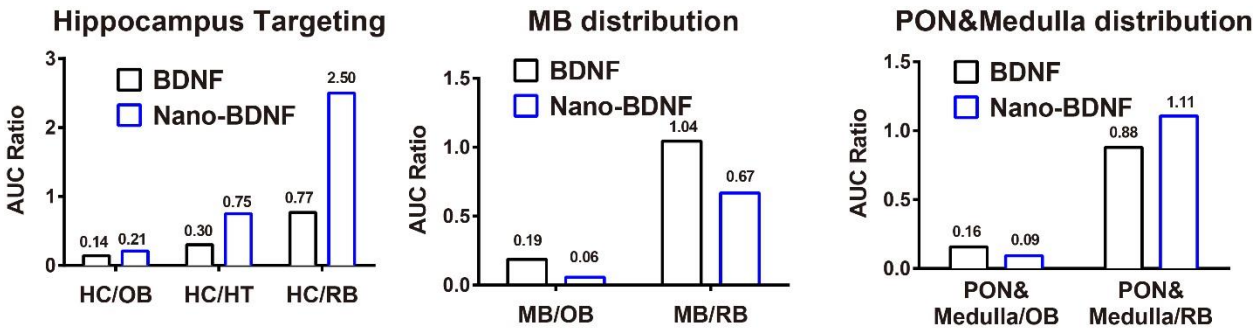

Figure 4.15 Nano-BDNF distribution in different brain regions after INB delivery compared to native BDNF.

Data present AUC ratios for the hippocampus (HC), pons (PON) and medulla, and midbrain (MB) vs. olfactory bulb (OB), hypothalamus (HT), and "rest of the brain" (RB) defined as all brain regions excluding HC and brainstem.

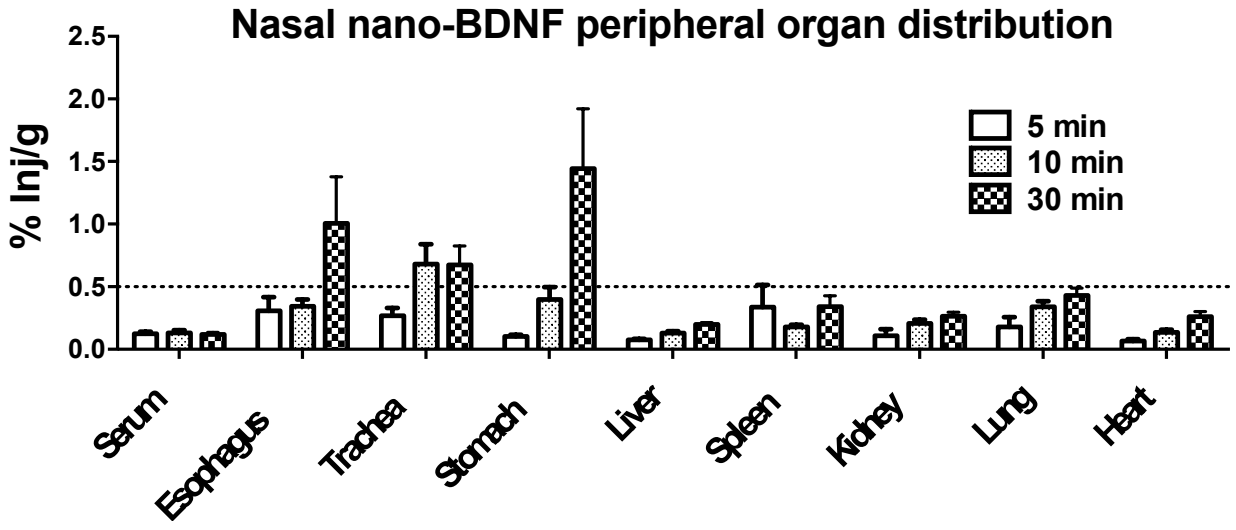

Figure 4.16 Peripheral organ distribution of Nano-BDNF following INB delivery.

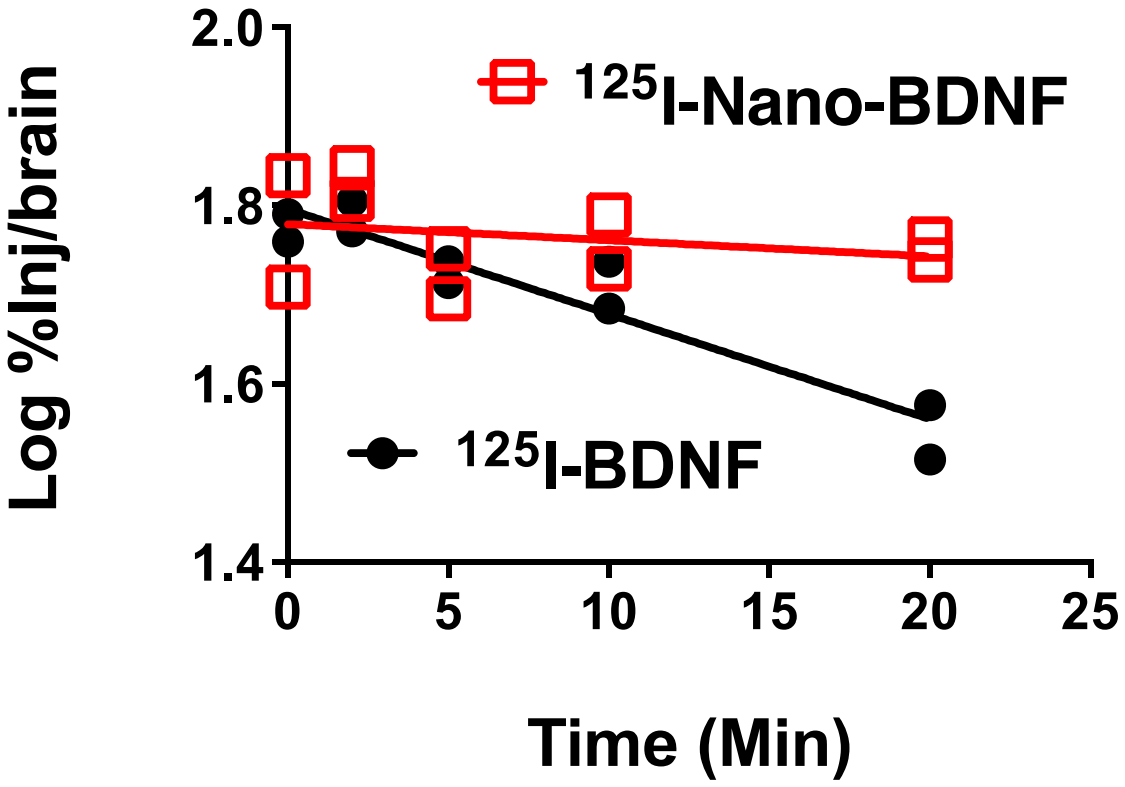

Figure 4.17 Inhibition of BDNF efflux from the brain to the blood.

Brain efflux curves of ^{125}I-BDNF or ^{125}I-Nano-BDNF after ICV injection showing the rate of efflux, as indicated by the slopes of the lines were −0.012 ± 0.0014 (r^2 = 0.89, n = 26) for BDNF and −0.0018 ± 0.0023 (r^2 = 0.07, n = 30) for Nano-BDNF, respectively. Both slopes were significantly non–zero and differences between the slopes are extremely significant.

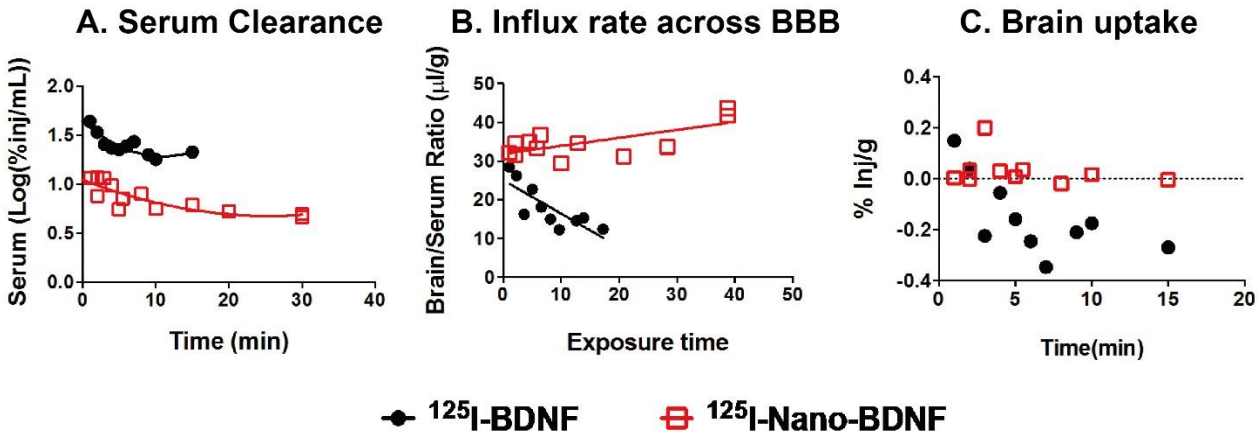

Figure 4.18 Brain PK of IV Nano-BDNF.

A. Nano-BDNF clears from the circulation similarly to native BDNF; **B.** Nano-BDNF displays net influx (Ki = 0.84 uL/g.min) into the brain, whereas native BDNF displays a net efflux from brain to the blood; **C.** Nano-BDNF displays higher brain uptake than native BDNF, as shown by AUC of 2.96 for Nano-BDNF vs 0.54 for native BDNF. The native BDNF or Nano-BDNF were injected IV at a single dose of 0.5 µg/mouse.

Table 4.1 Reference chart for the frequency levels shown in Figure 4.7 and Figure 4.8.

Frequency level	*Count_NC*	*Count_HB*
0	*0 - 100*	*0 - 100*
1	*100 - 1000*	*100 - 1000*
2	*1000 - 5000*	*1000 - 2000*
3	*5000 - 10000*	*2000 - 3000*
4	*10000 - 20000*	*3000 - 4000*
5	*> 20000*	*> 4000*

Count_NC denotes the total number of non-bonding contacts, and Count_HB denotes the total number of hydrogen bonds formed across the entire process of the four simulation experiments.

Table 4.2 Summary of BDNF AUC values (%inj·min/g) in different brain regions).

Region	BDNF	Nano-BDNF	Ratio
Olfactory	*5.094*	*34.32*	*6.7*
Striatum	*1.860*	*4.923*	*2.6*
Frontal Cortex	*0.8850*	*2.033*	*2.3*
Hypothalamus	*2.145*	*9.588*	*4.5*
Hippocampus	*0.7300*	*7.229*	*9.9*
Thalamus	*0.6150*	*4.419*	*7.2*
Parietal Cortex	*0.6200*	*2.261*	*3.6*
Occipital Cortex	*0.9400*	*2.593*	*2.8*
Cerebellum	*0.9200*	*1.704*	*1.9*
Midbrain	*0.9500*	*1.929*	*2.0*
Pons	*0.7917*	*3.220*	*4.1*
***Whole Brain**	*1.020*	*3.550*	*3.5*
****Brainstem**	*0.7289*	*2.905*	*4.0*
Serum	*4.835*	*3.088*	*0.6*

** Whole brain AUC was calculated as the weight-averaged AUC of all the brain regions listed above (except brainstem).*

*** Brainstem AUC was calculated as the weight-averaged AUC of midbrain and pons regions.*

CHAPTER 5 SUMMERY AND FUTURE DIRECTIONS

In this thesis, I reviewed the history of block ionomer complexes and introduced its applications in the field of protein delivery. Limitations with this formulation to be used as an *in vivo* protein delivery carrier are summarized, and different approaches to overcome these limitations are discussed.

Stability of protein block ionomer complexes *in vivo* is one of the biggest obstacles for their development and application. The formulation of SOD1 nanozyme addresses this problem by chemical crosslinking. This approach is useful for the delivery of SOD1 because this enzyme does not need to be released in order to function. Its substrate, superoxide anions, are small enough to penetrate into the core of the complex using a concentration gradient and get removed by the active enzyme encapsulated at the core. For stroke ischemic-reperfusion injury, this formulation was remarkably effective due to their passive accumulation at the injured sites on brain capillaries and arteries after stroke. By locally staying at the region where superoxide anions are generated for the entire length of blood vessel damage, this formulation is ideal for the treatment of similar pathologies involving vasculature damage. For example, ischemic-reperfusion injuries also occur in the case of myocardial infarction, and after organ transplantation; other similar conditions include the vascular damage after cancer radiotherapy. For the treatment of chronic diseases which involve frequent dosing regimens, the PLL polymer can be replaced by more biocompatible polymers, e.g. PAsp(DET), to avoid the toxicity associated with this highly cationic polymer. Furthermore, surface modifications by antibodies can be introduced to this formulation for more specific targeting towards different tissues of interest.

The BIC formulation formed with BDNF and PEG-PLE polymer represent another direction of our research by exploring the nature of molecular interactions driving the complex to form. It is widely accepted that hydrogen bonding and hydrophobic interactions can contribute to the formation and stability of BICs, and we can possibly design more stable BICs by taking advantage of these forces after fully understanding the natural laws governing them. Molecular modeling is a powerful tool for us to move this research forward, as well as the state of art biophysical research tools previously utilized to understand protein structures and interactions.

APPENDIX I

Brain PK study using therapeutic dose of BDNF shows that Nano-BDNF clears from circulations similar to native BDNF.

Brain PK study BDNF shows that Nano-BDNF clears from the circulation similarly to native BDNF. Nano-BDNF displays net influx (Ki = 0.84 uL/g.min) into the brain, whereas native BDNF displays a net efflux from brain to the blood. Consequently, Nano-BDNF displays higher brain uptake than native BDNF, as shown by AUC of 2.96 for Nano-BDNF vs 0.54 for native BDNF. The native BDNF or nano-BDNF were injected IV at a single dose of 0.5ug BDNF per mouse co-injected with ^{125}I-BDNF tracers.

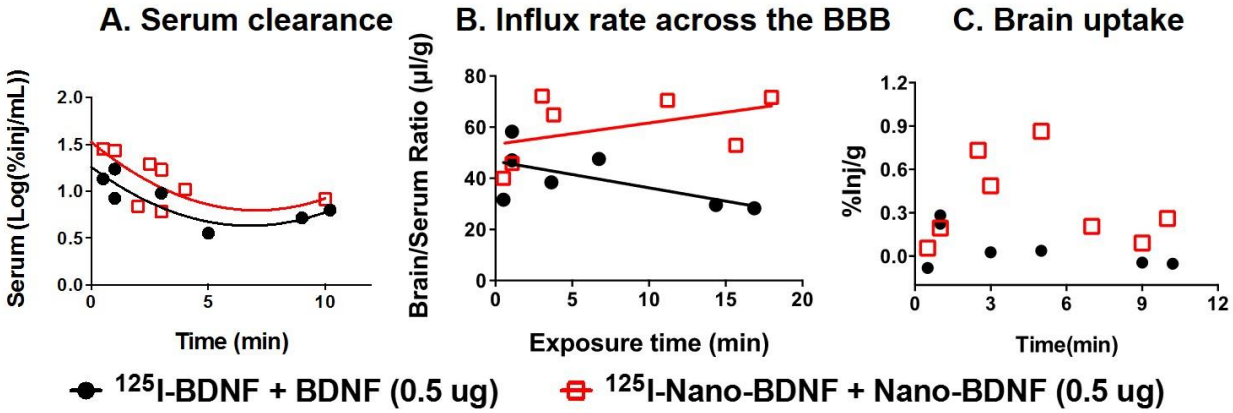

Figure 1. (**A**); Nano-BDNF rapidly enters the brain, whereas native BDNF displays an efflux from brain to the blood, as indicated by the influx rate (Ki) of Nano-BDNF across the BBB at 0.84 uL/g.min (**B)**; and consequently nano-BDNF displays higher brain uptake than native BDNF, as shown by AUC of 2.96 for Nano-BDNF vs 0.54 for native BDNF (**C**).

Nano-BDNF remains intact in brain but less stable in serum

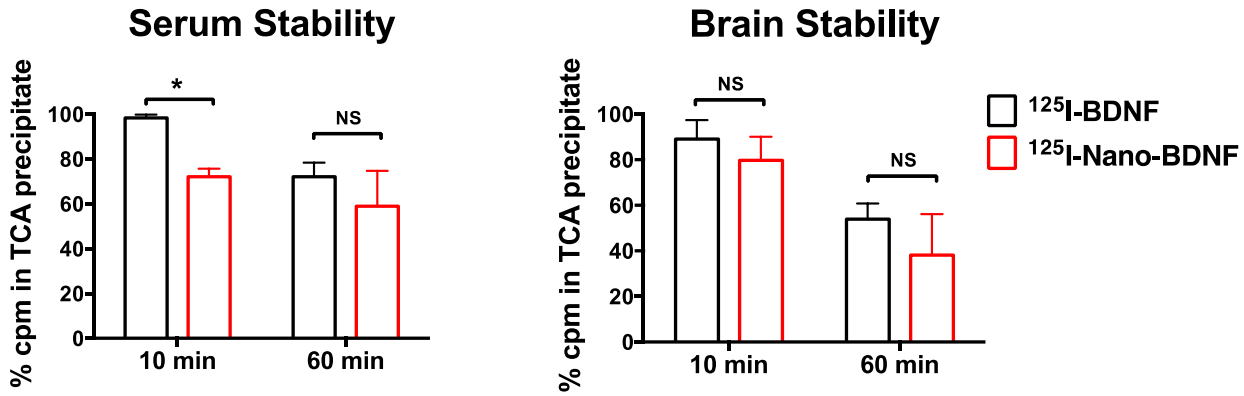

Figure 2. Nano-BDNF is less stable than native BDNF in serum at early time point (10 min) but remains similar intactness as native BDNF in the brain. The stability was accessed by the percent of radioactivity precipitated in the pellet and normalized by the values for processing controls (n=2/time point, * $p < 0.05$).

Capillary depletion study shows that at least half of Nano-BDNF is detected in brain parenchyma, indicating Nano-BDNF crosses the BBB and accumulates in the brain side.

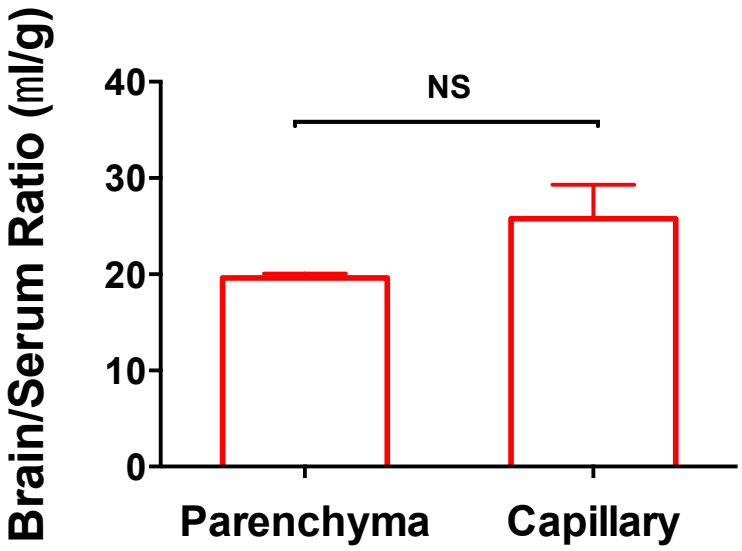

Figure 3. No difference was observed in amount between the capillary-associated BDNF and parenchyma-associated BDNF.

The amount of BDNF delivered by the same dose of PLE-PEG solution peaks at 5ug.

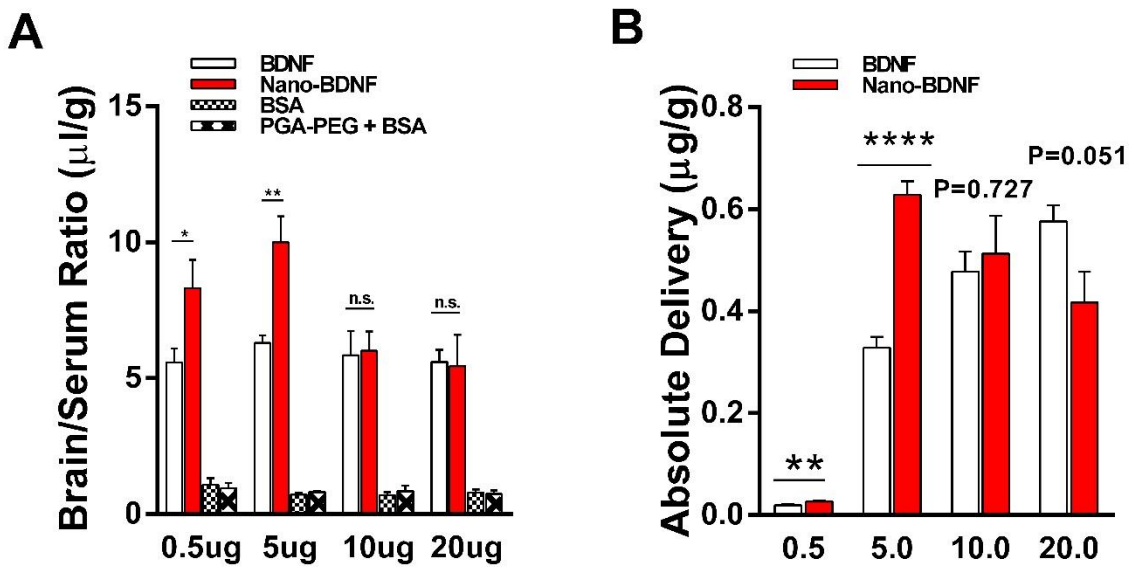

Figure 4. Different doses (0.5ug, 5ug, 10ug, and 20ug) of BDNF were mixed with 200ul of 1mg/ml PLE-PEG solution in LR, resulting in Nano-BDNF complex formed at different Z ratios (946, 94.6, 47.3, and 23.7, respectively). The solutions were then IV injected in experiment mice and their brain/serum ratios were measured **(A)** and absolute delivery values were calculated **(B)**. The result suggests 5ug as the most appropriate dose for in vivo delivery in this mouse model.

Brain uptake of Nano-BDNF is polymer-dose dependent

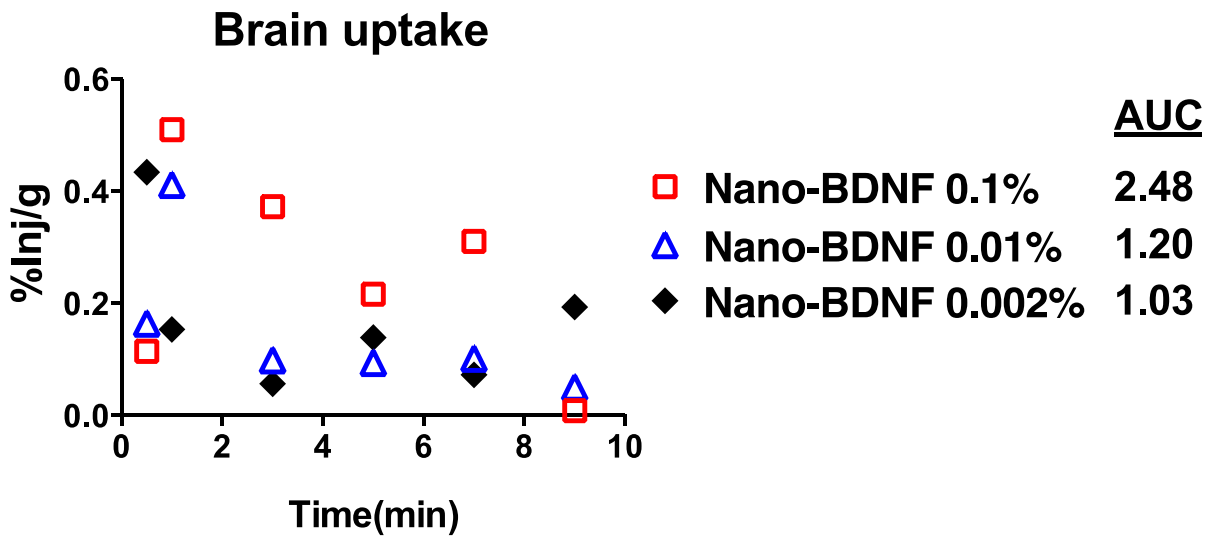

Figure 5. Nano-BDNF formed at various PEG-PLE concentrations (Nano-BDNF(0.1%) to (0.002%)) display significantly different brain PK profiles. Brain uptake of these 3 formulations, as shown by AUC of %inj/g of BDNF over 10 min following i.v. injection is 2.48, 1.20 and 1.03 respectively.

Nano-NGF Brain PK shows similar pattern to that of BDNF.

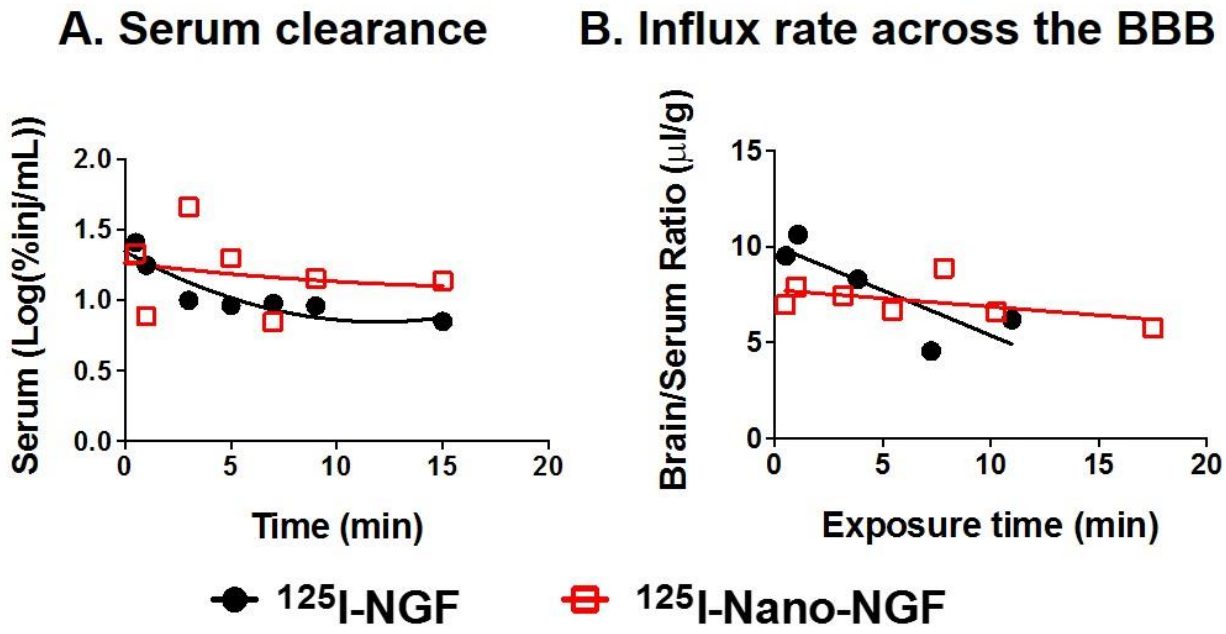

Figure 6. Brain PK study using trace amount of iodinated NGF substance shows that Nano-NGF greater of BBB penetration than native NGF.

PGA-PEG labeled with Cu-64 shows rapid brain influx

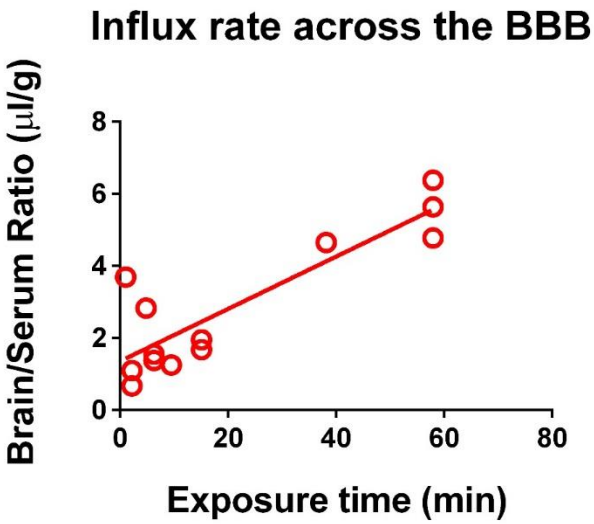

Figure 7. PEG-PLE polymer was labelled with Cu-64 and its brain influx rate was measured. The labelling was performed at the N-terminal of the PEG-PGA polymer, with help from Dr. Zibo Li, UNC Chapel Hill. PEG-PLE appears to be transported across BBB pretty fast. However, we don't know if it is transported as an intact polymer, or is it just the free glutamic acid being transported after degradation. To this end, TCA precipitation was done in the brain tissue, and assured the intactness of labelling.

APPENDIX II

Pharmacological validation of neuroprotection by BDNF nano-particles after focal cerebral ischemia in mice[5]

Reduced brain-derived neurotrophic factor (BDNF) levels have been associated with delayed neurological recovery, depression, and cognitive impairment following stroke, whereas supplementation reverses these impairments. Unfortunately, systemically administered BDNF in its native form has minimal therapeutic value due to its poor blood brain barrier permeability and short serum half-life. In this study, a novel nano-particle formulation of BDNF was used to evaluate potential neuroprotective efficacy after experimental stroke. Male C57BL/6J (8-10 weeks) mice were randomly assigned to one of three treatment groups after being subjected to 60 minutes of reversible middle cerebral artery occlusion (MCAo) followed by 14 days of reperfusion. Mice in Group A (early treatment) were treated twice with either BDNF nano-particles (nano-BDNF) or saline (250µg/kg i.v; n=6/group) 3 and 24 hours after the onset of MCAo. Mice in Groups B (intermediate treatment) and C (delayed treatment) were treated twice with saline, native-BDNF, or nano-BDNF (250µg/kg i.v.; n=8/group) 6 and 24 (B) or 12 and 24 (C) hours after MCAo, respectively. Early and intermediate nano-BDNF treatment led to a significant reduction in tissue loss compared to native-BDNF and saline treatment. Additionally, mice in Group A showed rapid recovery from stroke-induced neurological deficits. Delayed treatment (Group C) led to improved memory/cognition and reduced post-stroke depressive phenotypes, but had no effect on tissue atrophy. Collectively, our results indicate that nano-particle formulations of BDNF show neuroprotective effects even with delayed treatment. This study suggests that nano-BDNF treatment has therapeutic potential with a wide treatment window.

---

[5] Author information: Nia M Harris[#$], Nikolas Mancini[#], Rodney Ritzel[#], Yuhang Jiang*, Devika S Manickam*, Alexander V Kabanov*, Louise D McCullough[#$], & Rajkumar Verma[#@]

#Department of Neuroscience, University of Connecticut Health Center, Farmington, CT 06032, USA; $ Department of Neurology, University of Texas Health Science Center, Houston, TX 77030, USA; *Center for Nanomedicine and Drug Delivery, UNC Eshelman School of Pharmacy, University of North Carolina at Chapel Hill Chapel Hill, NC 27599-7362, USA; @Corresponding author: Rajkumar Verma, Department of Neuroscience, University of Connecticut Health Center, 263 Farmington Avenue, Farmington, CT 06030. E-mail: raverma@uchc.edu, rajsanto1979@gmail.com ; Phone: +1 860-679-8939.

REFERENCES

[1] H.K. Makadia, S.J. Siegel, Poly Lactic-co-Glycolic Acid (PLGA) as Biodegradable Controlled Drug Delivery Carrier, Polymers, 3 (2011) 1377-1397.

[2] F. Alexis, E. Pridgen, L.K. Molnar, O.C. Farokhzad, Factors Affecting the Clearance and Biodistribution of Polymeric Nanoparticles, Molecular pharmaceutics, 5 (2008) 505-515.

[3] M. Ye, S. Kim, K. Park, Issues in long-term protein delivery using biodegradable microparticles, Journal of controlled release : official journal of the Controlled Release Society, 146 (2010) 241-260.

[4] X. Huang, C.S. Brazel, On the importance and mechanisms of burst release in matrix-controlled drug delivery systems, Journal of controlled release : official journal of the Controlled Release Society, 73 (2001) 121-136.

[5] H.G.B.D. JONG, H.R. KRUYT, Coacewation (Partial miscibility in colloid systems). , Proceedings Royal Acad. Amsterdam, 32 (1929) 849-856.

[6] M.A. Cohen Stuart, N.A.M. Besseling, R.G. Fokkink, Formation of Micelles with Complex Coacervate Cores, Langmuir : the ACS journal of surfaces and colloids, 14 (1998) 6846-6849.

[7] A.I. Oparin, The origin of life on the earth, The origin of life on the Earth., (1957).

[8] A.V. Kabanov, S.V. Vinogradov, Y.G. Suzdaltseva, V. Alakhov, Water-soluble block polycations as carriers for oligonucleotide delivery, Bioconjug Chem, 6 (1995) 639-643.

[9] A. Harada, K. Kataoka, Formation of Polyion Complex Micelles in an Aqueous Milieu from a Pair of Oppositely-Charged Block Copolymers with Poly(ethylene glycol) Segments, Macromolecules, 28 (1995) 5294-5299.

[10] Y.H. Hsieh, Y.T. Hsiao, J.S. Jan, Shell and core cross-linked poly(L-lysine)/poly(acrylic acid) complex micelles, Soft matter, 10 (2014) 9568-9576.

[11] D. Fischer, H. Dautzenberg, K. Kunath, T. Kissel, Poly(diallyldimethylammonium chlorides) and their N-methyl-N-vinylacetamide copolymer-based DNA-polyplexes: role of molecular weight and charge density in complex formation, stability, and in vitro activity, International journal of pharmaceutics, 280 (2004) 253-269.

[12] Y. Jiang, A.M. Brynskikh, S.M. D, A.V. Kabanov, SOD1 nanozyme salvages ischemic brain by locally protecting cerebral vasculature, Journal of controlled release : official journal of the Controlled Release Society, 213 (2015) 36-44.

[13] Y. Jiang, P. Arounleut, S. Rheiner, Y. Bae, A.V. Kabanov, C. Milligan, D.S. Manickam, SOD1 nanozyme with reduced Toxicity and MPS accumulation, Journal of controlled release : official journal of the Controlled Release Society, (2016).

[14] C.P. Brangwynne, T.J. Mitchison, A.A. Hyman, Active liquid-like behavior of nucleoli determines their size and shape in Xenopus laevis oocytes, Proceedings of the National Academy of Sciences, 108 (2011) 4334-4339.

[15] C.P. Brangwynne, Soft active aggregates: mechanics, dynamics and self-assembly of liquid-like intracellular protein bodies, Soft matter, 7 (2011) 3052-3059.

[16] J.-F. Gohy, S.K. Varshney, S. Antoun, R. Jérôme, Water-Soluble Complexes Formed by Sodium Poly(4-styrenesulfonate) and a Poly(2-vinylpyridinium)-block-poly(ethyleneoxide) Copolymer, Macromolecules, 33 (2000) 9298-9305.

[17] C.L. Cooper, P.L. Dubin, A.B. Kayitmazer, S. Turksen, Polyelectrolyte-protein complexes, Curr. Opin. Colloid Interface Sci., 10 (2005) 52-78.

[18] S. Kim, J. Huang, Y. Lee, S. Dutta, H.Y. Yoo, Y.M. Jung, Y. Jho, H. Zeng, D.S. Hwang, Complexation and coacervation of like-charged polyelectrolytes inspired by mussels, Proceedings of the National Academy of Sciences of the United States of America, 113 (2016) E847-853.

[19] W. Kim, Y. Yamasaki, W.D. Jang, K. Kataoka, Thermodynamics of DNA condensation induced by poly(ethylene glycol)-block-polylysine through polyion complex micelle formation, Biomacromolecules, 11 (2010) 1180-1186.

[20] J. Zhang, S. Chen, Z. Zhu, S. Liu, Stopped-flow kinetic studies of the formation and disintegration of polyion complex micelles in aqueous solution, Physical chemistry chemical physics : PCCP, 16 (2014) 117-127.

[21] C.G. de Kruif, F. Weinbreck, R. de Vries, Complex coacervation of proteins and anionic polysaccharides, Curr. Opin. Colloid Interface Sci., 9 (2004) 340-349.

[22] T.V. Burova, N.V. Grinberg, V.Y. Grinberg, A.I. Usov, V.B. Tolstoguzov, C.G. Kruif, Conformational changes in iota- and kappa-carrageenans induced by complex formation with bovine beta-casein, Biomacromolecules, 8 (2007) 368-375.

[23] K. Laos, G.J. Brownsey, S.G. Ring, Interactions between furcellaran and the globular proteins bovine serum albumin and beta-lactoglobulin, Carbohydr. Polym., 67 (2007) 116-123.

[24] C. Wang, K.C. Tam, Interaction between polyelectrolyte and oppositely charged surfactant: Effect of charge density, J Phys Chem B, 108 (2004) 8976-8982.

[25] W. Kim, Y. Yamasaki, K. Kataoka, Development of a fitting model suitable for the isothermal titration calorimetric curve of DNA with cationic ligands, J Phys Chem B, 110 (2006) 10919-10925.

[26] I. Jelesarov, H.R. Bosshard, Isothermal titration calorimetry and differential scanning calorimetry as complementary tools to investigate the energetics of biomolecular recognition, Journal of molecular recognition : JMR, 12 (1999) 3-18.

[27] M. Jonsson, P. Linse, Polyelectrolyte-macroion complexation. II. Effect of chain flexibility, J. Chem. Phys., 115 (2001) 10975-10985.

[28] T. Wallin, P. Linse, Monte Carlo simulations of polyelectrolytes at charged micelles .1. Effects of chain flexibility, Langmuir : the ACS journal of surfaces and colloids, 12 (1996) 305-314.

[29] S. Stoll, P. Chodanowski, Polyelectrolyte Adsorption on an Oppositely Charged Spherical Particle. Chain Rigidity Effects, Macromolecules, 35 (2002) 9556-9562.

[30] T. Hattori, S. Bat-Aldar, R. Kato, H.B. Bohidar, P.L. Dubin, Characterization of polyanion-protein complexes by frontal analysis continuous capillary electrophoresis and small angle neutron scattering: effect of polyanion flexibility, Anal Biochem, 342 (2005) 229-236.

[31] A. Harada, K. Kataoka, Novel polyion complex micelles entrapping enzyme molecules in the core. 2. Characterization of the micelles prepared at nonstoichiometric mixing ratios, Langmuir : the ACS journal of surfaces and colloids, 15 (1999) 4208-4212.

[32] D.S. Manickam, A.M. Brynskikh, J.L. Kopanic, P.L. Sorgen, N.L. Klyachko, E.V. Batrakova, T.K. Bronich, A.V. Kabanov, Well-defined cross-linked antioxidant nanozymes for treatment of ischemic brain injury, Journal of controlled release : official journal of the Controlled Release Society, 162 (2012) 636-645.

[33] J.M. Park, B.B. Muhoberac, P.L. Dubin, J. Xia, Effects of protein charge heterogeneity in protein-polyelectrolyte complexation, Macromolecules, 25 (1992) 290-295.

[34] F.E. Regnier, The role of protein structure in chromatographic behavior, Science (New York, N.Y.), 238 (1987) 319-323.

[35] J.M. Park, B.B. Muhoberac, P.L. Dubin, J.L. Xia, EFFECTS OF PROTEIN CHARGE HETEROGENEITY IN PROTEIN-POLYELECTROLYTE COMPLEXATION, Macromolecules, 25 (1992) 290-295.

[36] C.L. Cooper, A. Goulding, A.B. Kayitmazer, S. Ulrich, S. Stoll, S. Turksen, S. Yusa, A. Kumar, P.L. Dubin, Effects of polyelectrolyte chain stiffness, charge mobility, and charge sequences on binding to proteins and micelles, Biomacromolecules, 7 (2006) 1025-1035.

[37] K.R. Grymonpre, B.A. Staggemeier, P.L. Dubin, K.W. Mattison, Identification by integrated computer modeling and light scattering studies of an electrostatic serum albumin-hyaluronic acid binding site, Biomacromolecules, 2 (2001) 422-429.

[38] E. Seyrek, P.L. Dubin, C. Tribet, E.A. Gamble, Ionic strength dependence of protein-polyelectrolyte interactions, Biomacromolecules, 4 (2003) 273-282.

[39] Y. Xu, M. Mazzawi, K. Chen, L. Sun, P.L. Dubin, Protein Purification by Polyelectrolyte Coacervation: Influence of Protein Charge Anisotropy on Selectivity, Biomacromolecules, 12 (2011) 1512-1522.

[40] J. Israelachvili, Intermolecular and Surface Forces, Elsevier Inc., 2011.

[41] J.M. Moss, M.P. Van Damme, W.H. Murphy, B.N. Preston, Dependence of salt concentration on glycosaminoglycan-lysozyme interactions in cartilage, Archives of biochemistry and biophysics, 348 (1997) 49-55.

[42] T. Hattori, R. Hallberg, P.L. Dubin, Roles of Electrostatic Interaction and Polymer Structure in the Binding of β-Lactoglobulin to Anionic Polyelectrolytes: Measurement of Binding Constants by Frontal Analysis Continuous Capillary Electrophoresis, Langmuir : the ACS journal of surfaces and colloids, 16 (2000) 9738-9743.

[43] N.L. Marky, G.S. Manning, An Interpretation of Small-Ion Effects on the Electrostatics of the λ Repressor DNA Complex, Journal of the American Chemical Society, 122 (2000) 6057-6066.

[44] F. Capito, R. Skudas, B. Stanislawski, H. Kolmar, Polyelectrolyte–protein interaction at low ionic strength: required chain flexibility depending on protein average charge, Colloid and Polymer Science, 291 (2013) 1759-1769.

[45] R. Schwartz, C.S. Ting, J. King, Whole proteome pI values correlate with subcellular localizations of proteins for organisms within the three domains of life, Genome research, 11 (2001) 703-709.

[46] S.S. Singh, A.K. Siddhanta, R. Meena, K. Prasad, S. Bandyopadhyay, H.B. Bohidar, Intermolecular complexation and phase separation in aqueous solutions of oppositely charged biopolymers, International journal of biological macromolecules, 41 (2007) 185-192.

[47] H. Espinosa-Andrews, J.G. Baez-Gonzalez, F. Cruz-Sosa, E.J. Vernon-Carter, Gum arabic-chitosan complex coacervation, Biomacromolecules, 8 (2007) 1313-1318.

[48] Y. Fang, L. Li, C. Inoue, L. Lundin, I. Appelqvist, Associative and segregative phase separations of gelatin/kappa-carrageenan aqueous mixtures, Langmuir : the ACS journal of surfaces and colloids, 22 (2006) 9532-9537.

[49] G. Mekhloufi, C. Sanchez, D. Renard, S. Guillemin, J. Hardy, pH-Induced structural transitions during complexation and coacervation of beta-lactoglobulin and acacia gum, Langmuir : the ACS journal of surfaces and colloids, 21 (2005) 386-394.

[50] J. Huotari, A. Helenius, Endosome maturation, The EMBO journal, 30 (2011) 3481-3500.

[51] V. Estrella, T. Chen, M. Lloyd, J. Wojtkowiak, H.H. Cornnell, A. Ibrahim-Hashim, K. Bailey, Y. Balagurunathan, J.M. Rothberg, B.F. Sloane, J. Johnson, R.A. Gatenby, R.J. Gillies, Acidity generated by the tumor microenvironment drives local invasion, Cancer research, 73 (2013) 1524-1535.

[52] E.M. Nemoto, S. Frinak, Brain tissue pH after global brain ischemia and barbiturate loading in rats, Stroke, 12 (1981) 77-82.

[53] S.L. Turgeon, C. Schmitt, C. Sanchez, Protein–polysaccharide complexes and coacervates, Curr. Opin. Colloid Interface Sci., 12 (2007) 166-178.

[54] M. Annaka, K. Morishita, S. Okabe, Electrostatic Self-Assembly of Neutral and Polyelectrolyte Block Copolymers and Oppositely Charged Surfactant, The Journal of Physical Chemistry B, 111 (2007) 11700-11707.

[55] J.-S. Park, Y. Akiyama, Y. Yamasaki, K. Kataoka, Preparation and Characterization of Polyion Complex Micelles with a Novel Thermosensitive Poly(2-isopropyl-2-oxazoline) Shell via the Complexation of Oppositely Charged Block Ionomers, Langmuir : the ACS journal of surfaces and colloids, 23 (2007) 138-146.

[56] A. Papagiannopoulos, A. Meristoudi, S. Pispas, U. Keiderling, Thermoresponsive behavior of micellar aggregates from end-functionalized PnBA-b-PNIPAM-COOH block copolymers and their complexes with lysozyme, Soft matter, (2016).

[57] M. Turk, S. Dincer, I.G. Yulug, E. Piskin, In vitro transfection of HeLa cells with temperature sensitive polycationic copolymers, Journal of controlled release : official journal of the Controlled Release Society, 96 (2004) 325-340.

[58] H.S. Bisht, D.S. Manickam, Y. You, D. Oupicky, Temperature-Controlled Properties of DNA Complexes with Poly(ethylenimine)-graft-poly(N-isopropylacrylamide), Biomacromolecules, 7 (2006) 1169-1178.

[59] S.R. Sershen, S.L. Westcott, N.J. Halas, J.L. West, Temperature-sensitive polymer-nanoshell composites for photothermally modulated drug delivery, Journal of biomedical materials research, 51 (2000) 293-298.

[60] I. Migneault, C. Dartiguenave, M.J. Bertrand, K.C. Waldron, Glutaraldehyde: behavior in aqueous solution, reaction with proteins, and application to enzyme crosslinking, BioTechniques, 37 (2004) 790-796, 798-802.

[61] A. Gaydess, E. Duysen, Y.A. Li, V. Gilman, A. Kabanov, O. Lockridge, T. Bronich, Visualization of exogenous delivery of nanoformulated butyrylcholinesterase to the central nervous system, Chem-Biol Interact, 187 (2010) 295-298.

[62] A. Kawamura, A. Harada, K. Kono, K. Kataoka, Self-assembled nano-bioreactor from block ionomers with elevated and stabilized enzymatic function, Bioconjug Chem, 18 (2007) 1555-1559.

[63] N.L. Klyachko, D.S. Manickam, A.M. Brynskikh, S.V. Uglanova, S. Li, S.M. Higginbotham, T.K. Bronich, E.V. Batrakova, A.V. Kabanov, Cross-linked antioxidant nanozymes for improved delivery to CNS, Nanomedicine : nanotechnology, biology, and medicine, 8 (2012) 119-129.

[64] X.F. Yuan, Y. Yamasaki, A. Harada, K. Kataoka, Characterization of stable lysozyme-entrapped polyion complex (PIC) micelles with crosslinked core by glutaraldehyde, Polymer, 46 (2005) 7749-7758.

[65] T. Takigawa, Y. Endo, Effects of glutaraldehyde exposure on human health, Journal of occupational health, 48 (2006) 75-87.

[66] D. Oupicky, R.C. Carlisle, L.W. Seymour, Triggered intracellular activation of disulfide crosslinked polyelectrolyte gene delivery complexes with extended systemic circulation in vivo, Gene therapy, 8 (2001) 713-724.

[67] M.J. Fischer, Amine coupling through EDC/NHS: a practical approach, Methods in molecular biology (Clifton, N.J.), 627 (2010) 55-73.

[68] M.J. Heffernan, N. Murthy, Disulfide-crosslinked polyion micelles for delivery of protein therapeutics, Annals of biomedical engineering, 37 (2009) 1993-2002.

[69] A. Harada, K. Kataoka, Novel polyion complex micelles entrapping enzyme molecules in the core: Preparation of narrowly-distributed micelles from lysozyme and poly(ethylene glycol)-poly(aspartic acid) block copolymer in aqueous medium, Macromolecules, 31 (1998) 288-294.

[70] A. Harada, K. Kataoka, Pronounced activity of enzymes through the incorporation into the core of polyion complex micelles made from charged block copolymers, Journal of controlled release : official journal of the Controlled Release Society, 72 (2001) 85-91.

[71] X. Yuan, Y. Yamasaki, A. Harada, K. Kataoka, Evaluation of enzymatic reactivity for lysozyme incorporated in the core-crosslinked polyion complex (PIC) micelles, 54 (2005) 2179.

[72] A.C. Obermeyer, C.E. Mills, X.H. Dong, R.J. Flores, B.D. Olsen, Complex coacervation of supercharged proteins with polyelectrolytes, Soft matter, 12 (2016) 3570-3581.

[73] Y. Lee, K. Kataoka, Biosignal-sensitive polyion complex micelles for the delivery of biopharmaceuticals, Soft matter, 5 (2009) 3810-3817.

[74] Y. Lee, T. Ishii, H.J. Kim, N. Nishiyama, Y. Hayakawa, K. Itaka, K. Kataoka, Efficient delivery of bioactive antibodies into the cytoplasm of living cells by charge-conversional polyion complex micelles, Angewandte Chemie (International ed. in English), 49 (2010) 2552-2555.

[75] A. Kim, Y. Miura, T. Ishii, O.F. Mutaf, N. Nishiyama, H. Cabral, K. Kataoka, Intracellular Delivery of Charge-Converted Monoclonal Antibodies by Combinatorial Design of Block/Homo Polyion Complex Micelles, Biomacromolecules, 17 (2016) 446-453.

[76] S. Lindhoud, R. de Vries, W. Norde, M.A.C. Stuart, Structure and stability of complex coacervate core micelles with lysozyme, Biomacromolecules, 8 (2007) 2219-2227.

[77] S. Lindhoud, R. de Vries, R. Schweins, M.A.C. Stuart, W. Norde, Salt-induced release of lipase from polyelectrolyte complex micelles, Soft matter, 5 (2009) 242-250.

[78] S. Lindhoud, L. Voorhaar, R. de Vries, R. Schweins, M.A.C. Stuart, W. Norde, Salt-Induced Disintegration of Lysozyme-Containing Polyelectrolyte Complex Micelles, Langmuir : the ACS journal of surfaces and colloids, 25 (2009) 11425-11430.

[79] S. Lindhoud, W. Norde, M.A. Cohen Stuart, Effects of polyelectrolyte complex micelles and their components on the enzymatic activity of lipase, Langmuir : the ACS journal of surfaces and colloids, 26 (2010) 9802-9808.

[80] S. Lindhoud, M.M.A.E. Claessens, Accumulation of small protein molecules in a macroscopic complex coacervate, Soft matter, 12 (2016) 408-413.

[81] A. Boudier, A. Aubert-Pouessel, P. Louis-Plence, C. Gerardin, C. Jorgensen, J.-M. Devoisselle, S. Begu, The control of dendritic cell maturation by pH-sensitive polyion complex micelles, Biomaterials, 30 (2009) 233-241.

[82] A. Boudier, A. Aubert-Pouessel, N. Mebarek, A. Chavanieu, J. Quentin, D. Martire, H. Boukhaddaoui, C. Gerardin, C. Jorgensen, J.M. Devoisselle, P. Louis-Plence, S. Begu, Development of tripartite polyion micelles for efficient peptide delivery into dendritic cells without altering their plasticity, Journal of controlled release : official journal of the Controlled Release Society, 154 (2011) 156-163.

[83] S. Pispas, Complexes of lysozyme with sodium (sulfamate-carboxylate)isoprene/ethylene oxide double hydrophilic block copolymers, Journal of Polymer Science Part a-Polymer Chemistry, 45 (2007) 509-520.

[84] K. Itaka, K. Yamauchi, A. Harada, K. Nakamura, H. Kawaguchi, K. Kataoka, Polyion complex micelles from plasmid DNA and poly(ethylene glycol)-poly(L-lysine) block copolymer as serum-tolerable polyplex system: physicochemical properties of micelles relevant to gene transfection efficiency, Biomaterials, 24 (2003) 4495-4506.

[85] M. Tangsangasaksri, H. Takemoto, M. Naito, Y. Maeda, D. Sueyoshi, H.J. Kim, Y. Miura, J. Ahn, R. Azuma, N. Nishiyama, K. Miyata, K. Kataoka, siRNA-Loaded Polyion Complex Micelle Decorated with Charge-Conversional Polymer Tuned to Undergo Stepwise Response to Intra-Tumoral and Intra-Endosomal pHs for Exerting Enhanced RNAi Efficacy, Biomacromolecules, 17 (2016) 246-255.

[86] D.P. Jones, J.L. Carlson, V.C. Mody, J. Cai, M.J. Lynn, P. Sternberg, Redox state of glutathione in human plasma, Free radical biology & medicine, 28 (2000) 625-635.

[87] Y. Lee, S. Fukushima, Y. Bae, S. Hiki, T. Ishii, K. Kataoka, A protein nanocarrier from charge-conversion polymer in response to endosomal pH, Journal of the American Chemical Society, 129 (2007) 5362-+.

[88] A.K. Varkouhi, M. Scholte, G. Storm, H.J. Haisma, Endosomal escape pathways for delivery of biologicals, Journal of controlled release : official journal of the Controlled Release Society, 151 (2011) 220-228.

[89] K. Miyata, M. Oba, M. Nakanishi, S. Fukushima, Y. Yamasaki, H. Koyama, N. Nishiyama, K. Kataoka, Polyplexes from Poly(aspartamide) Bearing 1,2-Diaminoethane Side Chains Induce pH-Selective, Endosomal Membrane Destabilization with Amplified Transfection and Negligible Cytotoxicity, Journal of the American Chemical Society, 130 (2008) 16287-16294.

[90] T. Kurinomaru, K. Shiraki, Noncovalent PEGylation of L-asparaginase using PEGylated polyelectrolyte, Journal of pharmaceutical sciences, 104 (2015) 587-592.

[91] A. Gaydess, E. Duysen, Y. Li, V. Gilman, A. Kabanov, O. Lockridge, T. Bronich, Visualization of exogenous delivery of nanoformulated butyrylcholinesterase to the central nervous system, Chem Biol Interact, 187 (2010) 295-298.

[92] L.W. Seymour, R. Duncan, J. Strohalm, J. Kopecek, Effect of molecular weight (Mw) of N-(2-hydroxypropyl)methacrylamide copolymers on body distribution and rate of excretion after subcutaneous, intraperitoneal, and intravenous administration to rats, Journal of biomedical materials research, 21 (1987) 1341-1358.

[93] S. Stolnik, L. Illum, S.S. Davis, Long circulating microparticulate drug carriers, Adv Drug Deliver Rev, 64 (2012) 290-301.

[94] A. Harada, K. Kataoka, On-off control of enzymatic activity synchronizing with reversible formation of supramolecular assembly from enzyme and charged block copolymers, Journal of the American Chemical Society, 121 (1999) 9241-9242.

[95] X. Yuan, A. Harada, Y. Yamasaki, K. Kataoka, Stabilization of lysozyme-incorporated polyion complex micelles by the omega-end derivatization of poly(ethylene glycol)-poly(alpha,beta-aspartic acid) block copolymers with hydrophobic groups, Langmuir : the ACS journal of surfaces and colloids, 21 (2005) 2668-2674.

[96] X. Yuan, Y. Yamasaki, A. Harada, K. Kataoka, Characterization of stable lysozyme-entrapped polyion complex (PIC) micelles with crosslinked core by glutaraldehyde, Polymer, 46 (2005) 7749-7758.

[97] T. Kurinomaru, S. Tomita, S. Kudo, S. Ganguli, Y. Nagasaki, K. Shiraki, Improved Complementary Polymer Pair System: Switching for Enzyme Activity by PEGylated Polymers, Langmuir : the ACS journal of surfaces and colloids, 28 (2012) 4334-4338.

[98] T. Kurinomaru, S. Tomita, Y. Hagihara, K. Shiraki, Enzyme hyperactivation system based on a complementary charged pair of polyelectrolytes and substrates, Langmuir : the ACS journal of surfaces and colloids, 30 (2014) 3826-3831.

[99] A. Kawamura, A. Harada, K. Kono, K. Kataoka, Functional evaluation of core-stabilized polyion complex micelles entrapping enzymes in the core, 54 (2005) 2977-2978.

[100] A. Kawamura, Y. Yoshioka, A. Harada, K. Kono, Acceleration of enzymatic reaction of trypsin through the formation of water-soluble complexes with poly(ethylene glycol)-block-poly(alpha,beta-aspartic acid), Biomacromolecules, 6 (2005) 627-631.

[101] Lloyd-Jones, Heart Disease and Stroke Statistics-2009 Update: A Report From the American Heart Association Statistics Committee and Stroke Statistics Subcommittee (vol 119, pg e21, 2009), Circulation, 122 (2010) E11-E11.

[102] J.L. Hinkle, M.M. Guanci, Acute ischemic stroke review, The Journal of neuroscience nursing : journal of the American Association of Neuroscience Nurses, 39 (2007) 285-293, 310.

[103] R. Rodrigo, R. Fernandez-Gajardo, R. Gutierrez, J.M. Matamala, R. Carrasco, A. Miranda-Merchak, W. Feuerhake, Oxidative Stress and Pathophysiology of Ischemic Stroke: Novel Therapeutic Opportunities, Cns Neurol Disord-Dr, 12 (2013) 698-714.

[104] M. Spranger, S. Krempien, S. Schwab, S. Donneberg, W. Hacke, Superoxide dismutase activity in serum of patients with acute cerebral ischemic injury - Correlation with clinical course and infarct size, Stroke, 28 (1997) 2425-2428.

[105] J.E. Jung, G.S. Kim, P. Narasimhan, Y.S. Song, P.H. Chan, Regulation of Mn-Superoxide Dismutase Activity and Neuroprotection by STAT3 in Mice after Cerebral Ischemia, Journal of Neuroscience, 29 (2009) 7003-7014.

[106] I. Margaill, M. Plotkine, D. Lerouet, Antioxidant strategies in the treatment of stroke, Free Radical Bio Med, 39 (2005) 429-443.

[107] J.L. Hughes, J.S. Beech, P.S. Jones, D. Wang, D.K. Menon, J.C. Baron, Mapping selective neuronal loss and microglial activation in the salvaged neocortical penumbra in the rat, Neuroimage, 49 (2010) 19-31.

[108] W.A. Banks, Delivery of peptides to the brain: Emphasis on therapeutic development, Biopolymers, 90 (2008) 589-594.

[109] R. Sood, Y. Yang, S. Taheri, E. Candelario-Jalil, E.Y. Estrada, E.J. Walker, J. Thompson, G.A. Rosenberg, Increased apparent diffusion coefficients on MRI linked with matrix metalloproteinases and edema in white matter after bilateral carotid artery occlusion in rats, J Cerebr Blood F Met, 29 (2009) 308-316.

[110] Y. Zhang, W.M. Pardridge, Conjugation of brain-derived neurotrophic factor to a blood-brain barrier drug targeting system enables neuroprotection in regional brain ischemia following intravenous injection of tbe neurotrophin, Brain research, 889 (2001) 49-56.

[111] W.S. Eum, D.W. Kim, I.K. Hwang, K.Y. Yoo, T.C. Kang, S.H. Jang, H.S. Choi, S.H. Choi, Y.H. Kim, S.Y. Kim, H.Y. Kwon, J.H. Kang, O.S. Kwon, S.W. Cho, K.S. Le, J. Park, M.H. Won, S.Y. Choi, In vivo protein transduction: biologically active intact pep-1-superoxide dismutase fusion protein efficiently protects against ischemic insult (vol 37, pg 1656, 2004), Free Radical Bio Med, 38 (2005) 406-406.

[112] D.W. Kim, H.J. Jeong, H.W. Kang, M.J. Shin, E.J. Sohn, M.J. Kim, E.H. Ahn, J.J. An, S.H. Jang, K.Y. Yoo, M.H. Won, T.C. Kang, I.K. Hwang, O.S. Kwon, S.W. Cho, J. Park, W.S. Eum, S.Y. Choi, Transduced human PEP-1-catalase fusion protein attenuates ischemic neuronal damage, Free Radical Bio Med, 47 (2009) 941-952.

[113] F.M. Veronese, P. Caliceti, O. Schiavon, M. Sergi, Polyethylene glycol-superoxide dismutase, a conjugate in search of exploitation, Adv Drug Deliver Rev, 54 (2002) 587-606.

[114] J.W. Francis, J.M. Ren, L. Warren, R.H. Brown, S.P. Finklestein, Postischemic infusion of Cu/Zn superoxide dismutase or SOD:Tet451 reduces cerebral infarction following focal ischemia/reperfusion in rats, Exp Neurol, 146 (1997) 435-443.

[115] M.K. Reddy, V. Labhasetwar, Nanoparticle-mediated delivery of superoxide dismutase to the brain: an effective strategy to reduce ischemia-reperfusion injury, FASEB journal : official publication of the Federation of American Societies for Experimental Biology, 23 (2009) 1384-1395.

[116] P.H. Chan, S. Longar, R.A. Fishman, Protective Effects of Liposome-Entrapped Superoxide-Dismutase on Posttraumatic Brain Edema, Ann Neurol, 21 (1987) 540-547.

[117] S. Imaizumi, V. Woolworth, R.A. Fishman, P.H. Chan, Liposome-Entrapped Superoxide-Dismutase Reduces Cerebral Infarction in Cerebral-Ischemia in Rats, Stroke, 21 (1990) 1312-1317.

[118] X. Yun, V.D. Maximov, J. Yu, H. Zhu, A.A. Vertegel, M.S. Kindy, Nanoparticles for targeted delivery of antioxidant enzymes to the brain after cerebral ischemia and reperfusion injury, Journal of cerebral blood flow and metabolism : official journal of the International Society of Cerebral Blood Flow and Metabolism, 33 (2013) 583-592.

[119] T. Yusa, J.D. Crapo, B.A. Freeman, Liposome-mediated augmentation of brain SOD and catalase inhibits CNS O2 toxicity, Journal of applied physiology: respiratory, environmental and exercise physiology, 57 (1984) 1674-1681.

[120] E.V. Batrakova, S. Li, A.D. Reynolds, R.L. Mosley, T.K. Bronich, A.V. Kabanov, H.E. Gendelman, A macrophage-nanozyme delivery system for Parkinson's disease, Bioconjugate Chem, 18 (2007) 1498-1506.

[121] E.G. Rosenbaugh, J.W. Roat, L. Gao, R.F. Yang, D.S. Manickam, J.X. Yin, H.D. Schultz, T.K. Bronich, E.V. Batrakova, A.V. Kabanov, I.H. Zucker, M.C. Zimmerman, The attenuation of central angiotensin II-dependent pressor response and intra-neuronal signaling by intracarotid injection of nanoformulated copper/zinc superoxide dismutase, Biomaterials, 31 (2010) 5218-5226.

[122] K. Savalia, D.S. Manickam, E.G. Rosenbaugh, J. Tian, I.M. Ahmad, A.V. Kabanov, M.C. Zimmerman, Neuronal uptake of nanoformulated superoxide dismutase and attenuation of angiotensin II-dependent hypertension after central administration, Free radical biology & medicine, 73 (2014) 299-307.

[123] A.M. Brynskikh, Y.L. Zhao, R.L. Mosley, S. Li, M.D. Boska, N.L. Klyachko, A.V. Kabanov, H.E. Gendelman, E.V. Batrakova, Macrophage delivery of therapeutic nanozymes in a murine model of Parkinson's disease, Nanomedicine : nanotechnology, biology, and medicine, 5 (2010) 379-396.

[124] N.L. Klyachko, M.J. Haney, Y. Zhao, D.S. Manickam, V. Mahajan, P. Suresh, S.D. Hingtgen, R.L. Mosley, H.E. Gendelman, A.V. Kabanov, E.V. Batrakova, Macrophages offer a paradigm switch for CNS delivery of therapeutic proteins, Nanomedicine (London, England), 9 (2014) 1403-1422.

[125] E.Z. Longa, P.R. Weinstein, S. Carlson, R. Cummins, Reversible Middle Cerebral-Artery Occlusion without Craniectomy in Rats, Stroke, 20 (1989) 84-91.

[126] K. Tieu, C. Perier, C. Caspersen, P. Teismann, D.C. Wu, S.D. Yan, A. Naini, M. Vila, V. Jackson-Lewis, R. Ramasamy, S. Przedborski, D-beta-hydroxybutyrate rescues mitochondrial respiration and mitigates features of Parkinson disease, The Journal of clinical investigation, 112 (2003) 892-901.

[127] T.O. Price, S.A. Farr, X. Yi, S. Vinogradov, E. Batrakova, W.A. Banks, A.V. Kabanov, Transport across the blood-brain barrier of pluronic leptin, The Journal of pharmacology and experimental therapeutics, 333 (2010) 253-263.

[128] L.D. McCullough, K. Blizzard, E.R. Simpson, O.K. Oz, P.D. Hurn, Aromatase cytochrome P450 and extragonadal estrogen play a role in ischemic neuroprotection, The Journal of neuroscience : the official journal of the Society for Neuroscience, 23 (2003) 8701-8705.

[129] R.A. Swanson, M.T. Morton, G. Tsao-Wu, R.A. Savalos, C. Davidson, F.R. Sharp, A semiautomated method for measuring brain infarct volume, Journal of cerebral blood flow and metabolism : official journal of the International Society of Cerebral Blood Flow and Metabolism, 10 (1990) 290-293.

[130] E.G. Rosenbaugh, K.K. Savalia, D.S. Manickam, M.C. Zimmerman, Antioxidant-based therapies for angiotensin II-associated cardiovascular diseases, Am J Physiol-Reg I, 304 (2013) R917-R928.

[131] R.C. Brown, T.P. Davis, Calcium modulation of adherens and tight junction function: a potential mechanism for blood-brain barrier disruption after stroke, Stroke, 33 (2002) 1706-1711.

[132] T.N. Nagaraja, K.A. Keenan, S.L. Brown, J.D. Fenstermacher, R.A. Knight, Relative distribution of plasma flow markers and red blood cells across BBB openings in acute cerebral ischemia, Neurol Res, 29 (2007) 78-80.

[133] T.N. Nagaraja, K.A. Keenan, J.D. Fenstermacher, R.A. Knight, Acute leakage patterns of fluorescent plasma flow markers after transient focal cerebral ischemia suggest large openings in blood-brain barrier, Microcirculation, 15 (2008) 1-14.

[134] V.R. Richardson, P. Cordell, K.F. Standeven, A.M. Carter, Substrates of Factor XIII-A: roles in thrombosis and wound healing, Clinical science, 124 (2013) 123-137.

[135] A. Sala, M. Ehrbar, D. Trentin, R.G. Schoenmakers, J. Voros, F.E. Weber, Enzyme mediated site-specific surface modification, Langmuir : the ACS journal of surfaces and colloids, 26 (2010) 11127-11134.

[136] E.F. Mammen, Coagulation abnormalities in liver disease, Hematology/oncology clinics of North America, 6 (1992) 1247-1257.

[137] N. Heye, C. Paetzold, R. Steinberg, J. Cervos-Navarro, The topography of microthrombi in ischemic brain infarct, Acta neurologica Scandinavica, 86 (1992) 450-454.

[138] F. Liu, D.P. Schafer, L.D. McCullough, TTC, fluoro-Jade B and NeuN staining confirm evolving phases of infarction induced by middle cerebral artery occlusion, Journal of neuroscience methods, 179 (2009) 1-8.

[139] T.F. Choudhri, B.L. Hoh, H.G. Zerwes, C.J. Prestigiacomo, S.C. Kim, E.S. Connolly, Jr., G. Kottirsch, D.J. Pinsky, Reduced microvascular thrombosis and improved outcome in acute murine stroke by inhibiting GP IIb/IIIa receptor-mediated platelet aggregation, The Journal of clinical investigation, 102 (1998) 1301-1310.

[140] G. Stoll, C. Kleinschnitz, B. Nieswandt, Molecular mechanisms of thrombus formation in ischemic stroke: novel insights and targets for treatment, Blood, 112 (2008) 3555-3562.

[141] Z.G. Zhang, M. Chopp, A. Goussev, D.Y. Lu, D. Morris, W. Tsang, C. Powers, K.L. Ho, Cerebral microvascular obstruction by fibrin is associated with upregulation of PAI-1 acutely after onset of focal embolic ischemia in rats, Journal of Neuroscience, 19 (1999) 10898-10907.

[142] H.K. Eltzschig, C.D. Collard, Vascular ischaemia and reperfusion injury, British medical bulletin, 70 (2004) 71-86.

[143] G.J. del Zoppo, Virchow's triad: the vascular basis of cerebral injury, Reviews in neurological diseases, 5 Suppl 1 (2008) S12-21.

[144] J. Kelly, A. Rudd, R.R. Lewis, C. Coshall, A. Moody, B.J. Hunt, Venous thromboembolism after acute ischemic stroke: a prospective study using magnetic resonance direct thrombus imaging, Stroke, 35 (2004) 2320-2325.

[145] S. Guo, W.J. Kim, J. Lok, S.R. Lee, E. Besancon, B.H. Luo, M.F. Stins, X. Wang, S. Dedhar, E.H. Lo, Neuroprotection via matrix-trophic coupling between cerebral endothelial cells and neurons, Proceedings of the National Academy of Sciences of the United States of America, 105 (2008) 7582-7587.

[146] M.S. Siket, Treatment of Acute Ischemic Stroke, Emergency medicine clinics of North America, 34 (2016) 861-882.

[147] F. Fluri, M.K. Schuhmann, C. Kleinschnitz, Animal models of ischemic stroke and their application in clinical research, Drug Design, Development and Therapy, 9 (2015) 3445-3454.

[148] E. Hodgson, I. Fridovich, Reversal of the superoxide dismutase reaction, Biochemical and biophysical research communications, 54 (1973) 270-274.

[149] E. Hodgson, I. Fridovich, The interaction of bovine erythrocyte superoxide dismutase with hydrogen peroxide: chemiluminescence and peroxidation, Biochemistry, 14 (1975) 5299-5303.

[150] E. Hodgson, I. Fridovich, The interaction of bovine erythrocyte superoxide dismutase with hydrogen peroxide: inactivation of the enzyme, Biochemistry, 14 (1975) 5294-5299.

[151] J. Koningsberger, B. van Asbeck, E. van Faassen, L. Wiegman, J. van Hattum, G. van Berge Henegouwen, J. Marx, Copper, zinc-superoxide dismutase and hydrogen peroxide: a hydroxyl radical generating system, Clinica chimica acta; international journal of clinical chemistry, 230 (1994) 51-61.

[152] G. Mao, P. Thomas, G. Lopaschuk, M. Poznansky, Superoxide dismutase (SOD)-catalase conjugates. Role of hydrogen peroxide and the Fenton reaction in SOD toxicity, The Journal of biological chemistry, 268 (1993) 416-420.

[153] S. Jewett, A. Rocklin, M. Ghanevati, J. Abel, J. Marach, A new look at a time-worn system: oxidation of CuZn-SOD by H2O2, Free radical biology & medicine, 26 (1999) 905-918.

[154] H. Zhang, J. Joseph, C. Felix, B. Kalyanaraman, Bicarbonate enhances the hydroxylation, nitration, and peroxidation reactions catalyzed by copper, zinc superoxide dismutase. Intermediacy of carbonate anion radical, The Journal of biological chemistry, 275 (2000) 14038-14045.

[155] D. Ramirez, S. Gomez Mejiba, R. Mason, Mechanism of hydrogen peroxide-induced Cu,Zn-superoxide dismutase-centered radical formation as explored by immuno-spin trapping: the role of copper- and carbonate radical anion-mediated oxidations, Free radical biology & medicine, 38 (2005) 201-214.

[156] I.L. Stefan, F. Irwin, Reversal of the superoxide dismutase reaction revisited, Free Radical Bio Med, 34 (2003).

[157] B. Omar, N. Gad, M. Jordan, S. Striplin, W. Russell, J. Downey, J. McCord, Cardioprotection by Cu,Zn-superoxide dismutase is lost at high doses in the reoxygenated heart, Free radical biology & medicine, 9 (1990) 465-471.

[158] M. Paller, J. Eaton, Hazards of antioxidant combinations containing superoxide dismutase, Free radical biology & medicine, 18 (1995) 883-890.

[159] D. Truelove, A. Shuaib, S. Ijaz, R. Ishaqzay, J. Kalra, Neuronal protection with superoxide dismutase in repetitive forebrain ischemia in gerbils, Free radical biology & medicine, 17 (1994) 445-450.

[160] B. Omar, J. McCord, The cardioprotective effect of Mn-superoxide dismutase is lost at high doses in the postischemic isolated rabbit heart, Free radical biology & medicine, 9 (1990) 473-478.

[161] J.M. McCord, Superoxide Dismutase, Lipid Peroxidation, and Bell-Shaped Dose Response Curves, Dose-Response, 6 (2008) 223-238.

[162] B. Uttara, A.V. Singh, P. Zamboni, R.T. Mahajan, Oxidative Stress and Neurodegenerative Diseases: A Review of Upstream and Downstream Antioxidant Therapeutic Options, Current Neuropharmacology, 7 (2009) 65-74.

[163] M. Schieber, N.S. Chandel, ROS function in redox signaling and oxidative stress, Current biology : CB, 24 (2014) R453-462.

[164] I. Fridovich, Superoxide anion radical (O2-.), superoxide dismutases, and related matters, J Biol Chem, 272 (1997) 18515-18517.

[165] G. Jadot, A. Vaille, J. Maldonado, P. Vanelle, Clinical pharmacokinetics and delivery of bovine superoxide dismutase, Clinical pharmacokinetics, 28 (1995) 17-25.

[166] Y. Takeda, H. Hashimoto, F. Kosaka, M. Hirakawa, M. Inoue, Albumin-binding superoxide dismutase with a prolonged half-life reduces reperfusion brain injury, The American journal of physiology, 264 (1993) H1708-1715.

[167] W.S. Eum, D.W. Kim, I.K. Hwang, K.Y. Yoo, T.C. Kang, S.H. Jang, H.S. Choi, S.H. Choi, Y.H. Kim, S.Y. Kim, H.Y. Kwon, J.H. Kang, O.S. Kwon, S.W. Cho, K.S. Lee, J. Park, M.H. Won, S.Y. Choi, In vivo protein transduction: biologically active intact pep-1-superoxide dismutase fusion protein efficiently protects against ischemic insult, Free radical biology & medicine, 37 (2004) 1656-1669.

[168] J.W. Francis, J. Ren, L. Warren, R.H. Brown, Jr., S.P. Finklestein, Postischemic infusion of Cu/Zn superoxide dismutase or SOD:Tet451 reduces cerebral infarction following focal ischemia/reperfusion in rats, Exp Neurol, 146 (1997) 435-443.

[169] O. Onaca, D.W. Hughes, V. Balasubramanian, M. Grzelakowski, W. Meier, C.G. Palivan, SOD antioxidant nanoreactors: influence of block copolymer composition on the nanoreactor efficiency, Macromol Biosci, 10 (2010) 531-538.

[170] T.D. Dziubla, V.V. Shuvaev, N.K. Hong, B.J. Hawkins, M. Madesh, H. Takano, E. Simone, M.T. Nakada, A. Fisher, S.M. Albelda, V.R. Muzykantov, Endothelial targeting of semi-permeable polymer nanocarriers for enzyme therapies, Biomaterials, 29 (2008) 215-227.

[171] F. Axthelm, O. Casse, W.H. Koppenol, T. Nauser, W. Meier, C.G. Palivan, Antioxidant nanoreactor based on superoxide dismutase encapsulated in superoxide-permeable vesicles, J Phys Chem B, 112 (2008) 8211-8217.

[172] S.C. Barber, R.J. Mead, P.J. Shaw, Oxidative stress in ALS: a mechanism of neurodegeneration and a therapeutic target, Biochimica et biophysica acta, 1762 (2006) 1051-1067.

[173] W.H. De Jong, P.J.A. Borm, Drug delivery and nanoparticles: Applications and hazards, International Journal of Nanomedicine, 3 (2008) 133-149.

[174] K. Xiao, Y. Li, J. Luo, J.S. Lee, W. Xiao, A.M. Gonik, R.G. Agarwal, K.S. Lam, The effect of surface charge on in vivo biodistribution of PEG-oligocholic acid based micellar nanoparticles, Biomaterials, 32 (2011) 3435-3446.

[175] D. Akagi, M. Oba, H. Koyama, N. Nishiyama, S. Fukushima, T. Miyata, H. Nagawa, K. Kataoka, Biocompatible micellar nanovectors achieve efficient gene transfer to vascular lesions without cytotoxicity and thrombus formation, Gene therapy, 14 (2007) 1029-1038.

[176] M. Baba, K. Itaka, K. Kondo, T. Yamasoba, K. Kataoka, Treatment of neurological disorders by introducing mRNA in vivo using polyplex nanomicelles, Journal of controlled release : official journal of the Controlled Release Society, 201 (2015) 41-48.

[177] A. Iriyama, T. Usui, Y. Yanagi, S. Amano, M. Oba, K. Miyata, N. Nishiyama, K. Kataoka, Gene transfer using micellar nanovectors inhibits corneal neovascularization in vivo, Cornea, 30 (2011) 1423-1427.

[178] K. Hayakawa, S. Uchida, T. Ogata, S. Tanaka, K. Kataoka, K. Itaka, Intrathecal injection of a therapeutic gene-containing polyplex to treat spinal cord injury, J. Control. Release, 197 (2015) 1-9.

[179] M. Harada-Shiba, I. Takamisawa, K. Miyata, T. Ishii, N. Nishiyama, K. Itaka, K. Kangawa, F. Yoshihara, Y. Asada, K. Hatakeyama, N. Nagaya, K. Kataoka, Intratracheal gene transfer of adrenomedullin using polyplex nanomicelles attenuates monocrotaline-induced pulmonary hypertension in rats, Molecular therapy : the journal of the American Society of Gene Therapy, 17 (2009) 1180-1186.

[180] M. Han, Y. Bae, N. Nishiyama, K. Miyata, M. Oba, K. Kataoka, Transfection study using multicellular tumor spheroids for screening non-viral polymeric gene vectors with low cytotoxicity and high transfection efficiencies, Journal of controlled release : official journal of the Controlled Release Society, 121 (2007) 38-48.

[181] K. Itaka, S. Ohba, K. Miyata, H. Kawaguchi, K. Nakamura, T. Takato, U.I. Chung, K. Kataoka, Bone regeneration by regulated in vivo gene transfer using biocompatible polyplex nanomicelles, Molecular therapy : the journal of the American Society of Gene Therapy, 15 (2007) 1655-1662.

[182] M.P. Xiong, Y. Bae, S. Fukushima, M.L. Forrest, N. Nishiyama, K. Kataoka, G.S. Kwon, pH-responsive Multi-PEGylated dual cationic nanoparticles enable charge modulations for safe gene delivery, ChemMedChem, 2 (2007) 1321-1327.

[183] T.C. Lai, Y. Bae, T. Yoshida, K. Kataoka, G.S. Kwon, pH-sensitive multi-PEGylated block copolymer as a bioresponsive pDNA delivery vector, Pharm Res, 27 (2010) 2260-2273.

[184] D.R. Rosen, T. Siddique, D. Patterson, D.A. Figlewicz, P. Sapp, A. Hentati, D. Donaldson, J. Goto, J.P. O'Regan, H.X. Deng, et al., Mutations in Cu/Zn superoxide dismutase gene are associated with familial amyotrophic lateral sclerosis, Nature, 362 (1993) 59-62.

[185] M.E. Gurney, H. Pu, A.Y. Chiu, M.C. Dal Canto, C.Y. Polchow, D.D. Alexander, J. Caliendo, A. Hentati, Y.W. Kwon, H.X. Deng, et al., Motor neuron degeneration in mice that express a human Cu,Zn superoxide dismutase mutation, Science (New York, N.Y.), 264 (1994) 1772-1775.

[186] F.L. Muller, W. Song, Y.C. Jang, Y. Liu, M. Sabia, A. Richardson, H. Van Remmen, Denervation-induced skeletal muscle atrophy is associated with increased mitochondrial ROS production, American journal of physiology. Regulatory, integrative and comparative physiology, 293 (2007) R1159-1168.

[187] M.C. Rocha, P.A. Pousinha, A.M. Correia, A.M. Sebastiao, J.A. Ribeiro, Early changes of neuromuscular transmission in the SOD1(G93A) mice model of ALS start long before motor symptoms onset, PloS one, 8 (2013) e73846.

[188] M.B. Robinson, J.L. Tidwell, T. Gould, A.R. Taylor, J.M. Newbern, J. Graves, M. Tytell, C.E. Milligan, Extracellular heat shock protein 70: a critical component for motoneuron survival, The Journal of neuroscience : the official journal of the Society for Neuroscience, 25 (2005) 9735-9745.

[189] D.J. Gifondorwa, M.B. Robinson, C.D. Hayes, A.R. Taylor, D.M. Prevette, R.W. Oppenheim, J. Caress, C.E. Milligan, Exogenous delivery of heat shock protein 70 increases lifespan in a mouse model of amyotrophic lateral sclerosis, The Journal of neuroscience : the official journal of the Society for Neuroscience, 27 (2007) 13173-13180.

[190] D.J. Gifondorwa, R. Jimenz-Moreno, C.D. Hayes, H. Rouhani, M.B. Robinson, J.L. Strupe, J. Caress, C. Milligan, Administration of Recombinant Heat Shock Protein 70 Delays Peripheral Muscle Denervation in the SOD1(G93A) Mouse Model of Amyotrophic Lateral Sclerosis, Neurology research international, 2012 (2012) 170426.

[191] C.S. Patlak, R.G. Blasberg, J.D. Fenstermacher, Graphical evaluation of blood-to-brain transfer constants from multiple-time uptake data, Journal of cerebral blood flow and metabolism : official journal of the International Society of Cerebral Blood Flow and Metabolism, 3 (1983) 1-7.

[192] C.S. Patlak, R.G. Blasberg, Graphical evaluation of blood-to-brain transfer constants from multiple-time uptake data. Generalizations, Journal of cerebral blood flow and metabolism : official journal of the International Society of Cerebral Blood Flow and Metabolism, 5 (1985) 584-590.

[193] C. Zheng, G. Ma, Z. Su, Native PAGE eliminates the problem of PEG-SDS interaction in SDS-PAGE and provides an alternative to HPLC in characterization of protein PEGylation, Electrophoresis, 28 (2007) 2801-2807.

[194] N.L. Ogihara, H.E. Parge, P.J. Hart, M.S. Weiss, J.J. Goto, B.R. Crane, J. Tsang, K. Slater, J.A. Roe, J.S. Valentine, D. Eisenberg, J.A. Tainer, Unusual trigonal-planar copper configuration revealed in the atomic structure of yeast copper-zinc superoxide dismutase, Biochemistry, 35 (1996) 2316-2321.

[195] H. Dautzenberg, Y.B. Gao, M. Hahn, Formation, structure, and temperature behavior of polyelectrolyte complexes between ionically modified thermosensitive polymers, Langmuir : the ACS journal of surfaces and colloids, 16 (2000) 9070-9081.

[196] S. Vinsant, C. Mansfield, R. Jimenez-Moreno, V. Del Gaizo Moore, M. Yoshikawa, T.G. Hampton, D. Prevette, J. Caress, R.W. Oppenheim, C. Milligan, Characterization of early pathogenesis in the SOD1(G93A) mouse model of ALS: part I, background and methods, Brain and behavior, 3 (2013) 335-350.

[197] S. Vinsant, C. Mansfield, R. Jimenez-Moreno, V. Del Gaizo Moore, M. Yoshikawa, T.G. Hampton, D. Prevette, J. Caress, R.W. Oppenheim, C. Milligan, Characterization of early pathogenesis in the SOD1(G93A) mouse model of ALS: part II, results and discussion, Brain and behavior, 3 (2013) 431-457.

[198] M.A. Hough, J.G. Grossmann, S.V. Antonyuk, R.W. Strange, P.A. Doucette, J.A. Rodriguez, L.J. Whitson, P.J. Hart, L.J. Hayward, J.S. Valentine, S.S. Hasnain, Dimer destabilization in superoxide dismutase may result in disease-causing properties: structures of motor neuron disease mutants, Proceedings of the National Academy of Sciences of the United States of America, 101 (2004) 5976-5981.

[199] C.T. Lin, M.T. Lin, Y.T. Chen, J.F. Shaw, Subunit interaction enhances enzyme activity and stability of sweet potato cytosolic Cu/Zn-superoxide dismutase purified by a His-tagged recombinant protein method, Plant molecular biology, 28 (1995) 303-311.

[200] J.L. Abernethy, H.M. Steinman, R.L. Hill, Bovine erythrocyte superoxide dismutase. Subunit structure and sequence location of the intrasubunit disulfide bond, J Biol Chem, 249 (1974) 7339-7347.

[201] J.R. Auclair, J.L. Johnson, Q. Liu, J.P. Salisbury, M. Rotunno, G.A. Petsko, D. Ringe, R.H. Brown, D.A. Bosco, J.N. Agar, Post-Translational Modification by Cysteine Protects Cu/Zn-Superoxide Dismutase From Oxidative Damage, Biochemistry, 52 (2013) 10.1021/bi4006122.

[202] Y. Furukawa, R. Fu, H.X. Deng, T. Siddique, T.V. O'Halloran, Disulfide cross-linked protein represents a significant fraction of ALS-associated Cu, Zn-superoxide dismutase aggregates in spinal cords of model mice, Proceedings of the National Academy of Sciences of the United States of America, 103 (2006) 7148-7153.

[203] K. Toichi, K. Yamanaka, Y. Furukawa, Disulfide scrambling describes the oligomer formation of superoxide dismutase (SOD1) proteins in the familial form of amyotrophic lateral sclerosis, J Biol Chem, 288 (2013) 4970-4980.

[204] M.L. Quillin, B.W. Matthews, Accurate calculation of the density of proteins, Acta crystallographica. Section D, Biological crystallography, 56 (2000) 791-794.

[205] J.C. Grotta, G.W. Albers, J.P. Broderick, E.H. Lo, S.E. Kasner, A.D. Mendelow, R.L. Sacco, L.K.S. Wong, Stroke: Pathophysiology, Diagnosis, and Management, Elsevier - Health Sciences Division, 2015.

[206] S.K. Nelson, S.K. Bose, J.M. McCord, The toxicity of high-dose superoxide dismutase suggests that superoxide can both initiate and terminate lipid peroxidation in the reperfused heart, Free radical biology & medicine, 16 (1994) 195-200.

[207] M.J. Ernsting, M. Murakami, A. Roy, S.D. Li, Factors controlling the pharmacokinetics, biodistribution and intratumoral penetration of nanoparticles, Journal of controlled release : official journal of the Controlled Release Society, 172 (2013) 782-794.

[208] S.M. Moghimi, A.C. Hunter, Capture of stealth nanoparticles by the body's defences, Critical reviews in therapeutic drug carrier systems, 18 (2001) 527-550.

[209] N.B. Shah, G.M. Vercellotti, J.G. White, A. Fegan, C.R. Wagner, J.C. Bischof, Blood-nanoparticle interactions and in vivo biodistribution: impact of surface PEG and ligand properties, Molecular pharmaceutics, 9 (2012) 2146-2155.

[210] A.H. Nagahara, D.A. Merrill, G. Coppola, S. Tsukada, B.E. Schroeder, G.M. Shaked, L. Wang, A. Blesch, A. Kim, J.M. Conner, E. Rockenstein, M.V. Chao, E.H. Koo, D. Geschwind, E. Masliah, A.A. Chiba, M.H. Tuszynski, Neuroprotective effects of brain-derived neurotrophic factor in rodent and primate models of Alzheimer's disease, Nature medicine, 15 (2009) 331-337.

[211] M. Ploughman, V. Windle, C.L. MacLellan, N. White, J.J. Dore, D. Corbett, Brain-derived neurotrophic factor contributes to recovery of skilled reaching after focal ischemia in rats, Stroke, 40 (2009) 1490-1495.

[212] J.L. Larimore, C.A. Chapleau, S. Kudo, A. Theibert, A.K. Percy, L. Pozzo-Miller, Bdnf overexpression in hippocampal neurons prevents dendritic atrophy caused by Rett-associated MECP2 mutations, Neurobiol Dis, 34 (2009) 199-211.

[213] T. Tsukahara, M. Takeda, S. Shimohama, O. Ohara, N. Hashimoto, Effects of brain-derived neurotrophic factor on 1-methyl-4-phenyl-1,2,3,6-tetrahydropyridine-induced parkinsonism in monkeys, Neurosurgery, 37 (1995) 733-739; discussion 739-741.

[214] S.U. Yanpallewar, C.A. Barrick, H. Buckley, J. Becker, L. Tessarollo, Deletion of the BDNF truncated receptor TrkB.T1 delays disease onset in a mouse model of amyotrophic lateral sclerosis, PloS one, 7 (2012) e39946.

[215] X.C. Ma, P. Liu, X.L. Zhang, W.H. Jiang, M. Jia, C.X. Wang, Y.Y. Dong, Y.H. Dang, C.G. Gao, Intranasal Delivery of Recombinant AAV Containing BDNF Fused with HA2TAT: a Potential Promising Therapy Strategy for Major Depressive Disorder, Scientific reports, 6 (2016) 22404.

[216] F. Molina-Holgado, P. Doherty, G. Williams, Tandem repeat peptide strategy for the design of neurotrophic factor mimetics, CNS & neurological disorders drug targets, 7 (2008) 110-119.

[217] W. Pan, W.A. Banks, M.B. Fasold, J. Bluth, A.J. Kastin, Transport of brain-derived neurotrophic factor across the blood-brain barrier, Neuropharmacology, 37 (1998) 1553-1561.

[218] J.F. Poduslo, G.L. Curran, Permeability at the blood-brain and blood-nerve barriers of the neurotrophic factors: NGF, CNTF, NT-3, BDNF, Brain research. Molecular brain research, 36 (1996) 280-286.

[219] M.H. Tuszynski, L. Thal, M. Pay, D.P. Salmon, H.S. U, R. Bakay, P. Patel, A. Blesch, H.L. Vahlsing, G. Ho, G. Tong, S.G. Potkin, J. Fallon, L. Hansen, E.J. Mufson, J.H. Kordower,

C. Gall, J. Conner, A phase 1 clinical trial of nerve growth factor gene therapy for Alzheimer disease, Nature medicine, 11 (2005) 551-555.

[220] A controlled trial of recombinant methionyl human BDNF in ALS: The BDNF Study Group (Phase III), Neurology, 52 (1999) 1427-1433.

[221] S.C. Apfel, J.A. Kessler, B.T. Adornato, W.J. Litchy, C. Sanders, C.A. Rask, Recombinant human nerve growth factor in the treatment of diabetic polyneuropathy. NGF Study Group, Neurology, 51 (1998) 695-702.

[222] A.H. Nagahara, M.H. Tuszynski, Potential therapeutic uses of BDNF in neurological and psychiatric disorders, Nature reviews. Drug discovery, 10 (2011) 209-219.

[223] X.Q. Chen, J.R. Fawcett, Y.E. Rahman, T.A. Ala, I.W. Frey, Delivery of Nerve Growth Factor to the Brain via the Olfactory Pathway, Journal of Alzheimer's disease : JAD, 1 (1998) 35-44.

[224] R.G. Thorne, G.J. Pronk, V. Padmanabhan, W.H. Frey, 2nd, Delivery of insulin-like growth factor-I to the rat brain and spinal cord along olfactory and trigeminal pathways following intranasal administration, Neuroscience, 127 (2004) 481-496.

[225] R.G. Thorne, L.R. Hanson, T.M. Ross, D. Tung, W.H. Frey, 2nd, Delivery of interferon-beta to the monkey nervous system following intranasal administration, Neuroscience, 152 (2008) 785-797.

[226] D.B. Renner, W.H. Frey, 2nd, L.R. Hanson, Intranasal delivery of siRNA to the olfactory bulbs of mice via the olfactory nerve pathway, Neuroscience letters, 513 (2012) 193-197.

[227] D.B. Renner, A.L. Svitak, N.J. Gallus, M.E. Ericson, W.H. Frey, 2nd, L.R. Hanson, Intranasal delivery of insulin via the olfactory nerve pathway, The Journal of pharmacy and pharmacology, 64 (2012) 1709-1714.

[228] J.J. Lochhead, R.G. Thorne, Intranasal delivery of biologics to the central nervous system, Adv Drug Deliv Rev, 64 (2012) 614-628.

[229] J.J. Lochhead, D.J. Wolak, M.E. Pizzo, R.G. Thorne, Rapid transport within cerebral perivascular spaces underlies widespread tracer distribution in the brain after intranasal administration, Journal of cerebral blood flow and metabolism : official journal of the International Society of Cerebral Blood Flow and Metabolism, 35 (2015) 371-381.

[230] S. Craft, L.D. Baker, T.J. Montine, S. Minoshima, G.S. Watson, A. Claxton, M. Arbuckle, M. Callaghan, E. Tsai, S.R. Plymate, P.S. Green, J. Leverenz, D. Cross, B. Gerton, Intranasal insulin therapy for Alzheimer disease and amnestic mild cognitive impairment: a pilot clinical trial, Archives of neurology, 69 (2012) 29-38.

[231] S.R. Alcala-Barraza, M.S. Lee, L.R. Hanson, A.A. McDonald, W.H. Frey, 2nd, L.K. McLoon, Intranasal delivery of neurotrophic factors BDNF, CNTF, EPO, and NT-4 to the CNS, Journal of drug targeting, 18 (2010) 179-190.

[232] S.R. Vaka, S.N. Murthy, A. Balaji, M.A. Repka, Delivery of brain-derived neurotrophic factor via nose-to-brain pathway, Pharm Res, 29 (2012) 441-447.

[233] Y. Kanato, K. Kitajima, C. Sato, Direct binding of polysialic acid to a brain-derived neurotrophic factor depends on the degree of polymerization, Glycobiology, 18 (2008) 1044-1053.

[234] Y. Kanato, S. Ono, K. Kitajima, C. Sato, Complex formation of a brain-derived neurotrophic factor and glycosaminoglycans, Bioscience, biotechnology, and biochemistry, 73 (2009) 2735-2741.

[235] J.G. Widdicombe, The physiology of the nose, Clinics in chest medicine, 7 (1986) 159-170.

[236] K.C. Lee, M.O. Park, D.H. Na, Y.S. Youn, S.D. Lee, S.D. Yoo, H.S. Lee, P.P. DeLuca, Intranasal delivery of PEGylated salmon calcitonins: hypocalcemic effects in rats, Calcified tissue international, 73 (2003) 545-549.

[237] M. Tobio, R. Gref, A. Sanchez, R. Langer, M.J. Alonso, Stealth PLA-PEG nanoparticles as protein carriers for nasal administration, Pharm Res, 15 (1998) 270-275.

[238] W.M. Pardridge, D. Wu, T. Sakane, Combined use of carboxyl-directed protein pegylation and vector-mediated blood-brain barrier drug delivery system optimizes brain uptake of brain-derived neurotrophic factor following intravenous administration, Pharm Res, 15 (1998) 576-582.

[239] K. Yoshida, G.F. Burton, J.S. McKinney, H. Young, E.F. Ellis, Brain and tissue distribution of polyethylene glycol-conjugated superoxide dismutase in rats, Stroke, 23 (1992) 865-869.

[240] C.C. Visser, S. Stevanovic, L.H. Voorwinden, L. van Bloois, P.J. Gaillard, M. Danhof, D.J. Crommelin, A.G. de Boer, Targeting liposomes with protein drugs to the blood-brain barrier in vitro, European journal of pharmaceutical sciences : official journal of the European Federation for Pharmaceutical Sciences, 25 (2005) 299-305.

[241] Y. Xie, L. Ye, X. Zhang, W. Cui, J. Lou, T. Nagai, X. Hou, Transport of nerve growth factor encapsulated into liposomes across the blood-brain barrier: in vitro and in vivo studies, Journal of controlled release : official journal of the Controlled Release Society, 105 (2005) 106-119.

[242] Q. Mu, T. Hu, J. Yu, Molecular insight into the steric shielding effect of PEG on the conjugated staphylokinase: biochemical characterization and molecular dynamics simulation, PloS one, 8 (2013) e68559.

[243] I.K. McDonald, J.M. Thornton, Satisfying hydrogen bonding potential in proteins, Journal of molecular biology, 238 (1994) 777-793.

[244] E.N. Baker, R.E. Hubbard, Hydrogen bonding in globular proteins, Progress in biophysics and molecular biology, 44 (1984) 97-179.

[245] A.V. Kabanov, V.A. Kabanov, DNA Complexes with Polycations for the Delivery of Genetic Material into Cells, Bioconjugate Chem, 6 (1995) 7-20.

[246] S. Holappa, L. Kantonen, T. Andersson, F. Winnik, H. Tenhu, Overcharging of polyelectrolyte complexes by the guest polyelectrolyte studied by fluorescence spectroscopy, Langmuir : the ACS journal of surfaces and colloids, 21 (2005) 11431-11438.

[247] K.N. Bakeev, V.A. Izumrudov, S.I. Kuchanov, A.B. Zezin, V.A. Kabanov, Kinetics and mechanism of interpolyelectrolyte exchange and addition reactions, Macromolecules, 25 (1992) 4249-4254.

[248] A. Zintchenko, G. Rother, H. Dautzenberg, Transition highly aggregated complexes-soluble complexes via polyelectrolyte exchange reactions: Kinetics, structural changes, and mechanism, Langmuir : the ACS journal of surfaces and colloids, 19 (2003) 2507-2513.

[249] H. Dautzenberg, Polyelectrolyte Complex Formation in Highly Aggregating Systems. 1. Effect of Salt: Polyelectrolyte Complex Formation in the Presence of NaCl, Macromolecules, 30 (1997) 7810-7815.

[250] N. Ali, K. Mattsson, J. Rissler, H.M. Karlsson, C.R. Svensson, A. Gudmundsson, C.H. Lindh, B.A.G. Jönsson, T. Cedervall, M. Kåredal, Analysis of nanoparticle–protein coronas formed in vitro between nanosized welding particles and nasal lavage proteins, Nanotoxicology, 10 (2016) 226-234.

[251] B. Casado, L.K. Pannell, P. Iadarola, J.N. Baraniuk, Identification of human nasal mucous proteins using proteomics, Proteomics, 5 (2005) 2949-2959.

[252] Y.Y. Wang, S.K. Lai, J.S. Suk, A. Pace, R. Cone, J. Hanes, Addressing the PEG mucoadhesivity paradox to engineer nanoparticles that "slip" through the human mucus barrier, Angewandte Chemie (International ed. in English), 47 (2008) 9726-9729.

[253] W.J. Callahan, L.O. Narhi, A.A. Kosky, M.J. Treuheit, Sodium chloride enhances the storage and conformational stability of BDNF and PEG-BDNF, Pharm Res, 18 (2001) 261-266.

[254] T. Nakamura, R. Sanokawa, Y. Sasaki, D. Ayusawa, M. Oishi, N. Mori, N-Shc: a neural-specific adapter molecule that mediates signaling from neurotrophin/Trk to Ras/MAPK pathway, Oncogene, 13 (1996) 1111-1121.

[255] E.A. Nance, G.F. Woodworth, K.A. Sailor, T.-Y. Shih, Q. Xu, G. Swaminathan, D. Xiang, C. Eberhart, J. Hanes, A Dense Poly(Ethylene Glycol) Coating Improves Penetration of Large Polymeric Nanoparticles Within Brain Tissue, Science Translational Medicine, 4 (2012) 149ra119.

[256] J.J. Iliff, M. Wang, Y. Liao, B.A. Plogg, W. Peng, G.A. Gundersen, H. Benveniste, G.E. Vates, R. Deane, S.A. Goldman, E.A. Nagelhus, M. Nedergaard, A paravascular pathway facilitates CSF flow through the brain parenchyma and the clearance of interstitial solutes, including amyloid beta, Sci Transl Med, 4 (2012) 147ra111.

[257] J.P. Bertram, M.F. Rauch, K. Chang, E.B. Lavik, Using polymer chemistry to modulate the delivery of neurotrophic factors from degradable microspheres: delivery of BDNF, Pharm Res, 27 (2010) 82-91.

[258] J. Tan, Y. Wang, X. Yip, F. Glynn, R.K. Shepherd, F. Caruso, Nanoporous Peptide Particles for Encapsulating and Releasing Neurotrophic Factors in an Animal Model of Neurodegeneration, Advanced materials (Deerfield Beach, Fla.), 24 (2012) 3362-3366.

[259] S. Mehrotra, D. Lynam, R. Maloney, K.M. Pawelec, M.H. Tuszynski, I. Lee, C. Chan, J. Sakamoto, Time Controlled Protein Release from Layer-by-Layer Assembled Multilayer Functionalized Agarose Hydrogels, Advanced functional materials, 20 (2010) 247-258.

[260] J. Narayanan, J.Y. Xiong, X.Y. Liu, Determination of agarose gel pore size: Absorbance measurements vis a vis other techniques, in: K.L. Teo, Z.X. Shen, L. Liu (Eds.) International Conference on Materials for Advanced Technologies, 2006, pp. 83-86.